DIGITAL SIGNAL PROCESSING FOR FRONT-END NON-IDEALITIES IN COHERENT OPTICAL OFDM SYSTEM

CAO SHENGJIAO

(B.Eng.), Tsinghua University, China

A THESIS SUBMITTED FOR THE DEGREE OF

DOCTOR OF PHILOSOPHY

DEPARTMENT OF

ELECTRICAL AND COMPUTER ENGINEERING

NATIONAL UNIVERSITY OF SINGAPORE

2014

DECLARATION

I hereby declare that this thesis is my original work and it has been written by me in its entirety.

I have duly acknowledged all the sources of information which have been used in the thesis.

This thesis has also not been submitted for any degree in any university previously.

CAO SHENGJIAO

April 24, 2014

Acknowledgement

First and foremost, I would like to express my sincere gratitude to my supervisors, Dr. Changyuan Yu and Prof. Pooi-Yuen Kam for their continuous support for my Ph.D. study. This thesis would not have been possible without their guidance and encouragement.

Besides my advisors, I would like to thank my thesis committee for their time devoted to review my thesis.

I would like to thank the friendly and cheerful fellow lab-mates in NUS optical fiber communication group.

Last but not least, I would also like to thank my parents. They were always supporting me and encouraging me with their best wishes.

ACKNOWLEDGEMENT

Contents

Summary

Coherent optical orthogonal frequency division multiplexing (CO-OFDM) has recently attracted much interest in the fiber-optic research community for its dispersion tolerance, ease of frequency domain equalization and high spectral efficiency. Unfortunately, CO-OFDM is sensitive to non-idealities in the transmitter and receiver front-ends, including carrier frequency offset, linear phase noise and IQ mismatch. All the three impairments will cause inter-carrier interference (ICI) and thus degrade the system performance. In this thesis, we will propose compensation methods for these front-end impairments.

First of all, we propose a novel frequency offset compensation (FOC) method for CO-OFDM system, which is demonstrated through experiment. The method is composed of a correlation-based method for the fraction part estimation and a pilot-tone-assisted method for the integer part estimation. Our algorithm can achieve the widest estimation range which is determined by the signal spectrum allocation and receiver bandwidth, by inserting only one pilot tone at the center of the spectrum, without the need of exhaustive search or tuning of any parameters. Furthermore, we carry out a comprehensive analysis to examine the performance of our FOC method in the presence of chromatic dispersion and linear phase noise. We analytically derive the fraction part estimation accuracy

of various correlation-based methods in the presence of linear phase noise.

Secondly, we propose a novel decision-aided phase estimation method to compensate for common phase error (CPE) induced by linear phase noise. Subsequently, we propose to combine decision-aided (DA) algorithm with pilot-aided (PA) as well as decision-feedback (DF) methods. DA+PA is able to reduce the overhead of PA while improving the phase noise tolerance of DA. DA+DF is demonstrated to be performing the best with zero overhead in a simulated 40-Gb/s CO-OFDM system. We also analytically evaluate the BER performance when only CPE is compensated for. A modified time-domain blind ICI mitigation algorithm is proposed for CO-OFDM system with non-constant amplitude modulation formats. The modified algorithm is demonstrated to be effective in mitigating ICI for a simulated 56-Gb/s CO-OFDM system over various non-constant amplitude modulation formats: 8-QAM, 16-QAM, 32-QAM and 64-QAM. Furthermore, it shows superior performance with the same complexity compared to the decision-aided ICI compensation algorithm at larger laser linewidths, especially for higher-order modulation format.

Thirdly, we propose a decision-aided joint compensation method for Tx IQ mismatch and channel distortion. We further propose a second phase compensation stage to deal with the linear phase noise. Simulation results show that our proposed algorithm can effectively mitigate Tx IQ mismatch, channel distortion and linear phase noise at the same time. Additionally, we propose to use pre-distortion scheme for compensating IQ mismatch and compare it with the post-equalization scheme through simulation.

Finally, we study the performance of LDPC coded OFDM system in the presence of linear phase noise. The performance of decoding algorithms de-

pends on the calculation of the decoding metric, i.e., the log-likelihood ratio. We will analytically derive new log-likelihood ratios with linear phase noise term for LDPC coded OFDM system with different modulation formats: differential M-ary phase shift keying system, pilot-aided M-ary phase shift keying system and pilot-aided M-QAM.

List of Tables

LIST OF TABLES

List of Figures

List of Abbreviations

A-LLR Approximate Log-likelihood Ratio

ADC Analog to Digital Converter

ASE Amplified Spontaneous Emission

AWGN Additive White Gaussian Noise

b2b back-to-back

BCH Bose-Chaudhuri-Hocquenghem

BER Bit Error Rate

BL-ICI Blind ICI

BL-ICI Blind ICI

CCDF Complementary Cumulative Density Function

CD Chromatic Dispersion

CDF Cumulative Distribution Function

CFO Carrier Frequency Offset

CP Cyclic Prefix

CPE Common Phase Error

DA Decision-aided

DAC Digital-to-Analog Converter

DAJC Decision-aided Joint Compensation

DD-OFDM Direct Detection OFDM

DDPE Decision-directed Phase Estimation

Demod Demodulator

DF Decision Feedback

DFT Discrete Fourier Transform

DGD Differential Group Delay

DMPSK Differential M-ary Phase Shift Keying

EDFA Erbium-doped Fiber Amplifier

FEC Forward Error Correction

FOC Frequency Offset Compensation

FOC Frequency Offset Compensation

FWM Four-wave Mixing

GI Guard Interval

GM Gaussian Metric

GSOP Gram-Schmidt Orthogonalization Procedure

GSOP Gram-Schmidt Orthogonalization Procedure

GVD Group Velocity Dispersion

ICI Inter-carrier Interference

IDFT Inverse Discrete Fourier Transform

ISI Inter-symbol Interference

LLR Log-likelihood Ratio

LO Local Oscillator

LPN Linear Phase Noise

MCM Multicarrier Modulation

Mod Modulator

MPSK M-ary Phase Shift Keying

OFDM Orthogonal Frequency-division Multiplexing

OSNR Optical Signal-to-noise Ratio

P/S Parallel-to-Serial

PA Pilot-aided

PA-LLR Pilot-aided LLR

PA-MPSK Pilot-aided M-ary Phase Shift Keying

PA-SA-LLR Pilot-aided Simplified-approximate LLR

PAPR Peak-to-Average Power Ratio

PD Pre-distortion

PDL Polarization-dependent Loss

PE Post-equalization

PLL Phase-locked Loops

PLL Phase-locked Loops

PMD Polarization Mode Dispersion

PSCs Pilot Subcarriers

PSD Power Spectral Density

RS Reed-Solomon

Rx Receiver

Rx Receiver

S/P Serial-to-Parallel

SMF Single-Mode Fiber

SNR Singal-to-noise Ratio

SPA Sum-product Algorithm

SPM Self-phase Modulation

SSMF Standard Single-Mode Fiber

Tx Transmitter

Tx Transmitter

WDM Wavelength-division Multiplexing

XPM Cross-phase Modulation

Chapter 1

Introduction

This thesis aims at DSP algorithms for compensating front-end non-idealities in CO-OFDM system, including carrier frequency offset, linear phase noise, as well as IQ mismatch. Additionally, another goal is on developing a new LLR metric with linear phase noise term for CO-OFDM system. Section 1.1 briefly introduces the motivation behind the development of DSP algorithms as well as decoding metrics. The scope and contributions of the thesis are highlighted in Section 1.2. Section 1.3 gives an overview of the organization of this thesis.

1.1 Motivation

Due to the enormous bandwidth of several hundred terahertz (THz) in the infrared lightwave region (from 400 THz down to 300 GHz in frequency), the lightwave systems can provide a staggering capacity of 100 Tb/s and beyond. In fact, the optical communication systems have become indispensable as the backbone of the modern-day information infrastructure.

Digital modulation techniques can be generally classified into two categories: single-carrier modulation in which the data are carried on a single main carrier and multicarrier modulation (MCM) in which the data are carried through many closely spaced subcarriers. Orthogonal frequency division multiplexing (OFDM) is a special class of MCM systems, which has become a standard for many wireless [4] and wired [5] communications. OFDM is proposed as an attractive long-haul transmission format in both coherent detection [6, 7] and direct detection [8–10]. Direct detection OFDM (DD-OFDM) allows for a simpler receiver structure, but has a worse energy and spectral efficiency, making it more suitable for cost-effective short reach applications [11]. CO-OFDM features superior performance in long-haul high-data-rate transmissions.

The next generation optical links are going to carry 100 Gbps per wavelength [12, 13]. Several experiments on CO-OFDM transmission [14–16] have proved it as a suitable candidate for the next generation of 100 Gb/s Ethernet transport. Moreover, several 1 Tb/s and beyond (per channel) CO-OFDM experiments have been carried out in [17–20].

CO-OFDM offers advantages such as its dispersion tolerance, ease of frequency domain equalization and high spectral efficiency. Additionally, it has the two unique features of multicarrier modulation [21]: (1) Its scalable spectrum partitioning provides flexibility in device-, subsystem- or system- level design; (2) its adaptation of pilot subcarriers simultaneously with the data carriers enables rapid and convenient ways for channel and phase estimation.

Unfortunately, CO-OFDM is sensitive to non-idealities in the transmitter and receiver front-ends, including carrier frequency offset (CFO), linear phase noise (LPN) and IQ mismatch. Fig. 1.1 shows the front-end (transmitter-receiver)

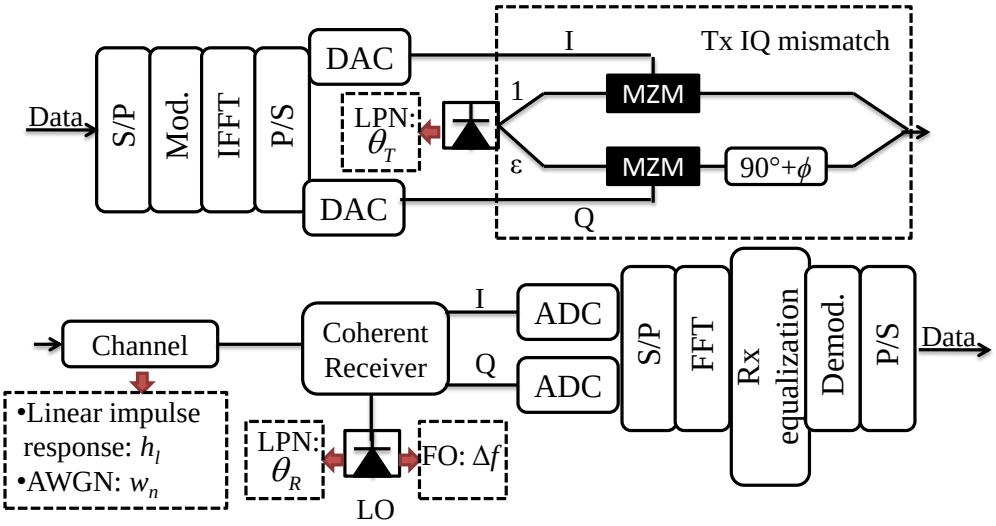

Figure 1.1: Diagram of DFT-based CO-OFDM systems with front-end non-idealities (S/P: serial to parallel, Mod./Demod: modulator/demodulator, P/S: parallel to serial, DAC/ADC: digital/analog to analog/digital converter, MZM: mach-zehnder modulator)

non-idealities of a DFT-based CO-OFDM system. Carrier frequency offset is caused by the frequency difference between the Tx laser and Rx local oscillator whereas linear phase noise is introduced by both Tx and Rx lasers. OFDM system is hundreds or thousands times more sensitive to CFO and LPN than the single carrier system with the same bit rate, due to its longer symbol duration. IQ mismatch is caused by the mismatch in amplitude and phase between I and Q branches due to non-ideal modulator or receiver hybrid. All the three impairments will cause inter-carrier interference and thus degrade the system performance.

Furthermore, the large peak-to-average power ratio (PAPR) of OFDM signals results in large system nonlinearity, especially in dispersion-managed systems [22, 23]. In addition to high nonlinearity, the resolution requirements of analog-to-digital and digital-to-analog converters are higher for OFDM com-

pared to single carrier systems [24]. On the other hand, single carrier systems require a fractionally-spaced two-dimensional linear equalizer to compensate for linear impairments (GVD and PMD) [25]. The equalizer part is the most computationally demanding and technologically challenging block for a single carrier system.

Low-density parity-check (LDPC) codes have become standards in many communication applications, including digital video broadcasting (DVB-S2) [26, 27], 10 Gigabit Ethernet (10GBASE-T) [28], broadband wireless access (WiMax) [29], wireless local area network (WiFi) [30], deep-space communications [31], and magnetic storage in hard disk drives [32]. LDPC coded OFDM is a suitable coded modulation technique for long-haul optical communication [33]. Recently, there have been quite a few experimental demonstrations using LDPC coded CO-OFDM for high speed long-haul transmission [34, 35]. The performance of decoding algorithms depends on the calculation of the decoding metric, i.e., the log-likelihood ratio. Thus, the study of the LLR metric in the presence of linear phase noise deserves great attention.

In this thesis, we will focus on combatting the front-end non-idealiteis in CO-OFDM system. Digital signal processing algorithms are proposed for compensating carrier frequency offset, linear phase noise and IQ mismatch. We will also propose new LLR metrics with the consideration of one specific front-end non-ideality: linear phase noise.

1.2 Scope and Contributions

This dissertation is aimed at the development of digital signal processing algorithms for front-end non-idealities in CO-OFDM system. The goal is to design efficient and effective algorithms for combatting carrier frequency offset, linear phase noise and IQ mismatch. An additional goal is to derive a new LLR metric with one specific front-end non-ideality term, i.e., the linear phase noise, for CO-OFDM system.

To summarise, this thesis makes the following contributions towards DSP algorithm for front-end non-idealities and LLR metrics with linear phase noise term:

1. The key challenge in carrier frequency offset compensation for CO-OFDM system is to estimate the carrier frequency offset (CFO) both accurately and efficiently with a full acquisition range. In this thesis, we propose a novel frequency offset compensation method for CO-OFDM system. Our algorithm can achieve the widest estimation range which is determined by the signal spectrum allocation and receiver bandwidth, by inserting only one pilot tone at the center of the spectrum. Only one training symbol is needed for CFO acquisition, without the need of exhaustive search or tuning of any parameters. We have demonstrated our algorithm through both experiment and analysis. Specifically, analytical expressions of estimation accuracy (with the consideration of LPN) are derived for various correlation-based CFO estimators, which are confirmed through simulation. To our best knowledge, there is no other work of analytical CFO accuracy derivation (with the consideration of LPN) in the literature.

2. Uncompensated linear phase noise will cause common phase error (CPE) and intercarrier interference (ICI). In this thesis, we will propose compensation methods to combat both CPE and ICI. We first introduce a novel decision-aided (DA) carrier phase estimation algorithm. Based on that, we further propose new schemes which combine pilot-aided (PA) , decision-aided (DA) and decision-feedback (DF) methods. The combination of DA and PA is shown to improve phase noise tolerance compared to DA while reducing overhead compared to PA. The combination of DA and DF offers better tolerance to linear phase noise compared to DA and other purely decision-directed methods. In addition, we analytically evaluate the BER performance when only CPE is compensated for. BER expression under Gaussian approximation is derived, which is quite close to the simulation result, especially for smaller laser linewidth. Lastly, we propose a modified time-domain blind ICI mitigation method for non-constant amplitude modulation format, e.g., M-QAM. The modified algorithm is demonstrated to be effective in mitigating ICI for a simulated 56-Gb/s CO-OFDM system over various non-constant amplitude modulation formats: 8-QAM, 16-QAM, 32-QAM and 64-QAM. Furthermore, it shows superior performance with the same complexity compared to the decision-aided ICI compensation algorithm at larger laser linewidths, especially for higher-order modulation format.

3. We successfully introduce a decision-aided joint compensation method for Tx IQ mismatch and channel distortion. Our method is superior to the previous methods in several aspects. Firstly, DAJC makes use of standard

pilot symbols, which simplifies the design compared to the special pilot structure proposed in [36]. Secondly, the adaptive characteristic of DAJC makes it more robust to time-variant channel and mismatch parameters, and also reduces the requirement on overhead. Last but not least, DAJC performs better than both GSOP and PA, with tolerable and adjustable increase in complexity. In addition to DAJC, we further propose a second phase compensation stage to deal with the linear phase noise. Simulation results show that our proposed algorithm can effectively mitigate Tx IQ mismatch, channel distortion and linear phase noise at the same time. Lastly, we propose a pre-distortion (PD) scheme for compensating Tx IQ mismatch in the presence of channel distortion for CO-OFDM system, which is compared with post-equalization (PE) through simulation. PE is performing better than PD for smaller phase or amplitude mismatch values while PD has larger tolerance towards the mismatch.

4. In this thesis, we will study the performance of LDPC coded OFDM system in the presence of linear phase noise. The performance of decoding algorithm depends on the calculation of the decoding metric, i.e., the log-likelihood ratio. We will analytically derive new log-likelihood ratios with linear phase noise term for LDPC coded OFDM system with different modulation formats: differential M-ary phase shift keying system, pilot-aided M-ary phase shift keying system and pilot-aided M-QAM. As far as we know, this is the first work which gives analytical LLR expressions for LDPC coded OFDM system with the consideration of linear phase noise. First of all, we propose a new LLR metric and its approx-

imate version (A-LLR) based on two-symbol-interval observations with consideration of linear phase noise for LDPC coded OFDM system with differential BPSK format. Our LLR metric is performing slightly better than the GM metric with larger tolerance to SNR under-estimation error while A-LLR metric has almost identical performance compared to the LLR metric but with much lower computational complexity. Moreover, we extend this work to OFDM system with differential MPSK formats. Secondly, we derive a pilot-aided LLR (PA-LLR) metric for LDPC coded MPSK CO-OFDM with consideration of linear phase noise. The bit LLR metric is evaluated from the likelihood function given the received signal that carries that bit and a set of pilot subcarriers as well as unknown linear phase noise. Lastly, we propose to incorporate the knowledge of phase noise into the calculation of bit LLR and derive it for M-QAM CO-OFDM system. With the help of the PA-LLR, the phase noise term is included into the decoding metric and thus the need for prior phase compensation is eliminated. Moreover, our PA-LLR performs better than the conventional LLR in 16QAM and 64QAM simulation. The PA-SA-LLR is proposed as a simplification of PA-LLR, which achieves similar performance with much lower complexity.

1.3 Thesis Outline

The remainder of this thesis is organized as follows:

In Chapter 2, we introduce the OFDM fundamentals, including its mathematical formulation, DFT implementation, overheads and spectral efficiency

as well as the cyclic prefix. The linear distortions(CD/PMD, frequency offset, linear phase noise, IQ mismatch) are modeled and studied in details. The basics of LDPC encoding and decoding are briefly presented.

In Chapter 3, a novel correlation-based and pilot-tone-assisted FOC method is introduced for CO-OFDM system, which can achieve the widest estimation range by inserting only one training symbol. The performance of our FOC method is experimentally demonstrated in a 22.24-Gb/s CO-OFDM system. In addition, a comprehensive analysis is carried out to examine the performance of our FOC method. Analytical expressions of fraction part estimation accuracy are obtained for various correlation-based methods in the presence of linear phase noise.

In Chapter 4, a novel decision-aided algorithm is introduced to compensate for the common phase error caused by linear phase noise, and we further propose to combine decision-aided algorithm with pilot-aided as well as decision-feedback methods. A modified time-domain blind ICI mitigation algorithm is proposed for CO-OFDM system with non-constant amplitude modulation formats.

In Chapter 5, a decision-aided joint compensation method for Tx IQ mismatch and channel distortion is introduced, and we propose to employ a second stage to compensate the linear phase noise. We propose to use pre-distortion scheme for compensating IQ mismatch and compare it with the post-equalization scheme through simulation.

In Chapter 6, a new log-likelihood ratio with the linear phase noise term is analytically derived for CO-OFDM system with different modulation formats: differential MPSK, pilot-aided MPSK and pilot-aided M-QAM.

Finally, conclusion and future work are presented in Chapter 7.

Chapter 2

Fundamental Theory and Literature Review of Coherent Optical OFDM System

2.1 Introduction

In this chapter, an overview of the coherent optical orthogonal frequency-division multiplexing (OFDM) system is presented, including the OFDM fundamentals, the linear distortions of optical channel and the basics of LDPC encoding and decoding. We will also discuss the motivation and review the literature in each of the sub-topics.

OFDM belongs to the class of multicarrier modulation (MCM), in which the data information is carried over many lower rate subcarriers. Compared to single carrier, OFDM is more resistant to inter-symbol interference (ISI) and inter-carrier interference (ICI) caused by chromatic dispersion (CD) and polarization

mode dispersion (PMD). Another advantage of OFDM is known as ease of signal processing with the efficient algorithm of FFT/IFFT. Typical CO-OFDM channel equalizer requires N (number of subcarriers) complex multiplications per symbol and FFT/IFFT takes $(N/2) \times log_2(N)$ multiplications. If we transmit R OFDM symbols (consisting of N subcarriers) per second, the number of multiplications required is $(1 + log_2(N)) \times N \times R$ per second. For single carrier systems using FIR filter with M taps, it requires $M \times N \times R$ multiplications per second to achieve the same bit rate. For example, the required taps using time-domain equalization is around 100 per symbol for 112-Gb/s PolMux-QPSK with only 500-ps/nm chromatic dispersion [37]. Note that the complexity of single carrier channel equalization could be reduced by employing frequency domain equalization similar to OFDM systems. Thus, OFDM offers easier digital signal processing compared to single carrier for most cases in high speed coherent optical long-haul transmission. OFDM and single carrier share a comparable spectral efficiency although the advantage of OFDM is that inherently the linear crosstalk of the neighboring channels is negligible [38]. Despite all the advantages, OFDM is prone to front-end non-idealities including carrier frequency offset, linear phase noise and IQ mismatch. Lastly, OFDM signal has a high peak-to-average power ratio (PAPR), and thus it is more vulnerable to fiber nonlinear effects such as self-phase modulation (SPM), cross-phase modulation (XPM) and four-wave mixing (FWM). In this thesis, we study the digital signal processing algorithms for combatting the front-end non-idealities in CO-OFDM system. Therefore, a proper understanding of OFDM basics is of great importance for further studies.

2.2 OFDM Fundamentals

2.2.1 Mathematical Formulation of an OFDM Signal

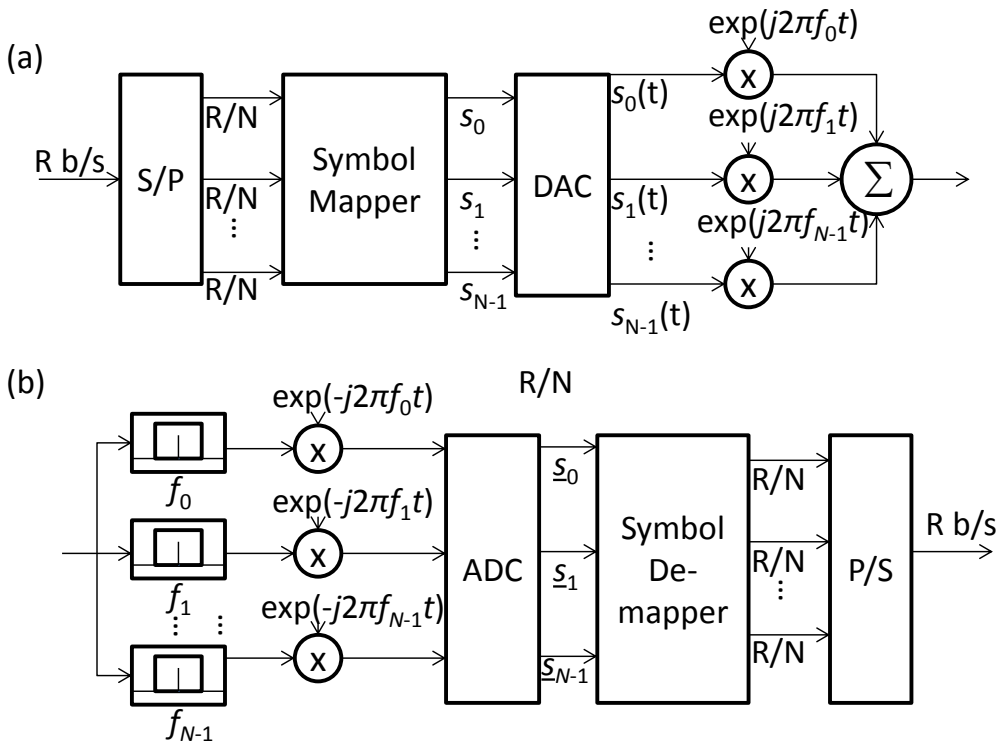

Figure 2.1: The transmitter (a) and receiver (b) of a multicarrier modulation system.

The generic presentation of an MCM system is shown in Fig. 2.1. At the transmitter side, a transmitted bitstream (R b/s) is divided into N different substreams, which are sent in parallel over orthogonal subchannels. The MCM

transmitted signal $s(t)$ is represented as [21]:

$$s(t) = \sum_{i=-\infty}^{+\infty} \sum_{k=0}^{N-1} c_{ki} s_k(t - iT_s) \tag{2.1}$$

$$s_k(t) = \Pi(t) e^{j2\pi f_k t} \tag{2.2}$$

$$\Pi(t) = \begin{cases} 1, (0 < t \leq T_s) \\ 0, (t \leq 0, t > T_s) \end{cases} \tag{2.3}$$

where c_{ki} is the ith information symbol at the kth subcarrier, $s_k(t)$ is the waveform for the kth subcarrier, N is the number of subcarriers, f_k is the frequency of the subcarrier, T_s is the symbol period, and $\Pi(t)$ is the pulse shaping function. At the receiver side, a correlator matched to the subcarrier is used:

$$c'_{ki} = \frac{1}{T_s} \int_0^{T_s} r(t - iT_s) s_k^* dt = \frac{1}{T_s} \int_0^{T_s} r(t - iT_s) e^{-j2\pi f_k t} dt \tag{2.4}$$

where $r(t)$ is the received time domain signal. The classical MCM uses non-overlapped bandlimited signals which reduces the spectral efficiency. And a bank of large numbers of oscillators and filters is used for implementation at both transmitter and receiver sides. OFDM was proposed by employing overlapped yet orthogonal signal sets. The correlation between different subcarriers are formulated as:

$$\begin{aligned} \delta_{kl} &= \frac{1}{T_s} \int_0^{T_s} s_k s_l^* dt \\ &= \frac{1}{T_s} \int_0^{T_s} \exp(j2\pi(f_k - f_l)t) dt \\ &= \exp(j\pi(f_k - f_l)T_s) \frac{\sin(\pi(f_k - f_l)T_s)}{\pi(f_k - f_l)T_s} \end{aligned} \tag{2.5}$$

So the orthogonal condition is:

$$f_k - f_l = \frac{m}{T_s}(m \text{ is an integer}) \tag{2.6}$$

The orthogonal subcarriers are spaced at multiples of inverse of the symbol periods, which can be recovered with matched filters without ICI.

2.2.2 Discrete Fourier Transform Implementation of OFDM

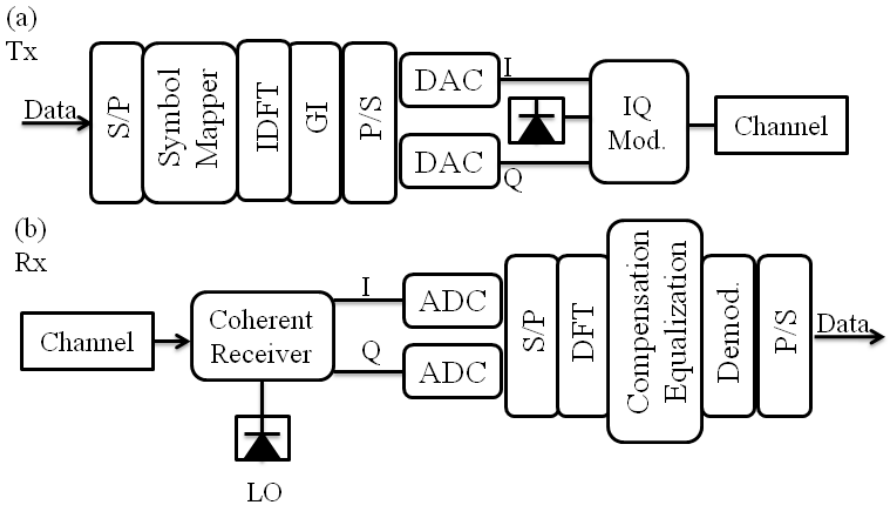

Figure 2.2: The transmitter (a) and receiver (b) of a DFT based OFDM system.

In [39], the idea of using inverse discrete Fourier transform (IDFT)/discrete Fourier transform (DFT) was first proposed for OFDM modulation/demodulation. Two critical devices have been assumed for the DFT/IDFT implementation: digital-to-analog converter (DAC) and analog-to-digital converter (ADC).

The OFDM transmitter and receiver diagram based on DFT/IDFT are shown

in Fig 2.2 (a) and (b), respectively. At the Tx side, the serial input data bits are converted into many parallel data streams through serial-to-parallel (S/P) conversion. The data streams are mapped to corresponding information symbols $X_{k,i}$ for different subcarriers within one OFDM symbol. Data subcarriers are padded with virtual subcarriers, which allows the system to easily accommodate for transmit filters with a smooth transition band [5]. Over-sampling is easily achieved with the use of virtual subcarriers, which is a main advantage in OFDM compared to SC schemes. With commonly used filters, 20% of virtual subcarriers is typically sufficient [40]. The discrete time-domain samples are obtained via IDFT:

$$x_{N*i+n} = \mathfrak{F}^{-1}\{X_{k,i}\} = \frac{1}{\sqrt{N}} \sum_{k=0}^{N-1} X_{k,i} e^{j2\pi kn/N} \tag{2.7}$$

where i and k denote the i-th OFDM symbol and k-th subcarrier. $\mathfrak{F}$ is the discrete Fourier transform while $\mathfrak{F}^{-1}$ is the inverse discrete Fourier transform. The fast Fourier transform algorithm reduces the complexity from $O(N^2)$ using definition to $O(Nlog_2(N))$. Each OFDM symbol is subsequently inserted with a guard interval (GI). The parallel streams are converted back to serial samples through parallel-to-serial (P/S) conversion and into real-time waveform through DAC. The base band electrical signal are modulated onto light with an IQ modulator (Mod.). At the receiver end, the OFDM signal is down-converted to baseband with a coherent receiver, sampled by an ADC, transformed to parallel pipes by S/P conversion and demodulated with DFT:

$$\hat{X}_{k,i} = \mathfrak{F}\{y_{N*i+n}\} = \frac{1}{\sqrt{N}} \sum_{k=0}^{N-1} y_{N*i+n} e^{-j2\pi kn/N} \tag{2.8}$$

where y_{N*i+n} are the received signals sampled at $(i + n/N)T_s$. After passing through equalizer and demodulator (Demod), the parallel subcarriers are demodulated and transformed back into serial data bits through P/S conversion. The advantages of DFT/IDFT implementation of OFDM are: (1) the existence of a fast fourier transform algorithm reduces the computational complexity to only $O(N \log N)$, and (2) a large number of orthogonal subcarriers can be generated and demodulated without the need of much more complex RF oscillators and filters.

2.2.3 OFDM Overheads and Spectral Efficiency

In an OFDM system, the overhead may come from various OFDM specific sources: training symbol (ϵ_{TS}), cyclic prefix (ϵ_{CP}), pilot subcarriers for phase noise compensation (ϵ_{PNC}) [41]. Other general factors including feedforward error correction (FEC) (ϵ_{FEC}) and Ethernet framing (ϵ_{EN}) may also introduce overhead. The resulting gross or nominal data rate R_{gross} is larger than the net data rate R_{net} by a factor of the total overhead:

$$R_{gross} = R_{net}(1 + \epsilon_{TS})(1 + \epsilon_{CP})(1 + \epsilon_{PNC})(1 + \epsilon_{FEC})(1 + \epsilon_{EN}) \tag{2.9}$$

The signal bandwidth of an OFDM system is:

$$B_d = \frac{R_{gross}}{\log_2(M)} \tag{2.10}$$

where M is the number of constellation points. Fig. 2.3(a) shows the optical spectrum of wavelength-division multiplexed (WDM) channels, each with CO-

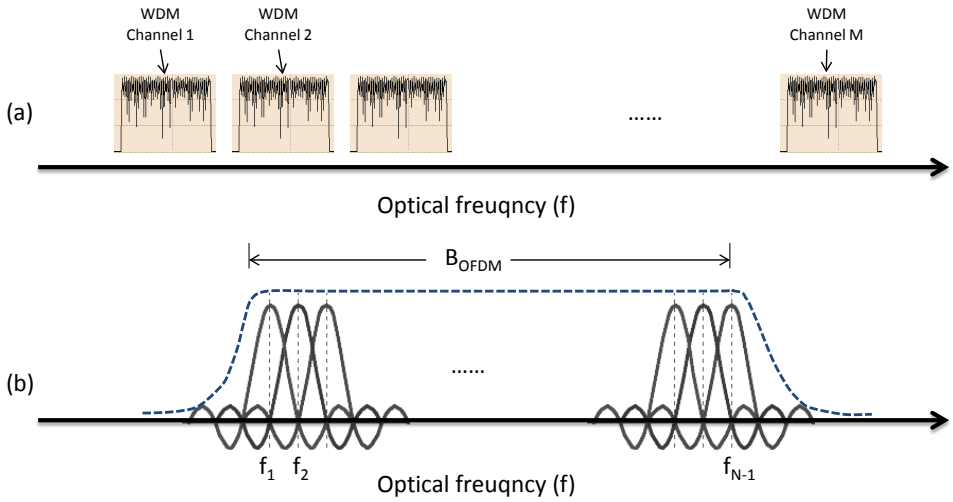

Figure 2.3: Optical Spectrum for (a) WDM CO-OFDM channels, (b) OFDM signal for one wavelength.

OFDM modulation and Fig. 2.3(b) shows the optical spectrum for each wavelength channel. According to [21], assuming the bandwidth of the first null is the boundary of each wavelength channel, the single channel OFDM bandwidth is given by:

$$B_{OFDM} = \frac{2}{T_s} + \frac{N-1}{t_s} \tag{2.11}$$

where T_s is the OFDM symbol period and t_s is the symbol period minus the guard interval as illustrated in Fig. 2.4. The spectral efficiency of OFDM is found to be:

$$\eta = 2\frac{R}{B_{OFDM}} \tag{2.12}$$

where $R = R_{net}/\log_2(M)$ is the OFDM net symbol rate and the factor of 2 accounts for two polarizations in the fiber. Assuming that a large number of

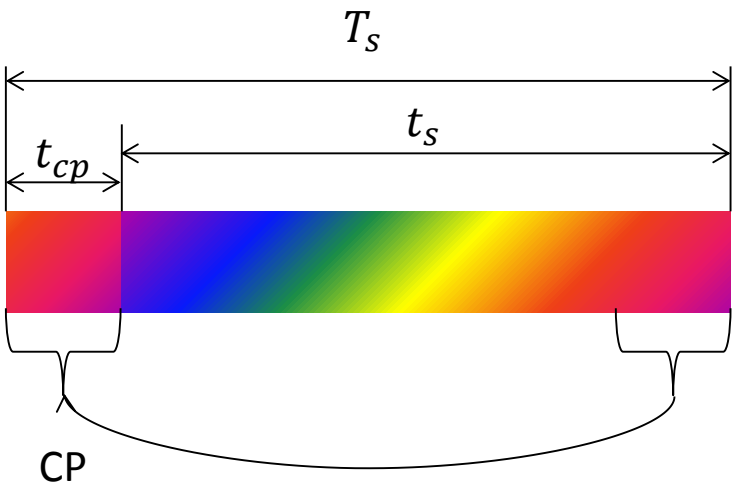

Figure 2.4: Illustration of T_s, t_s and t_{cp}.

subcarriers are used ($N >> 1$), we can approximate Eq. 2.12 with:

$$\eta \approx 2\alpha, \alpha = \frac{t_s}{T_s} \tag{2.13}$$

2.2.4 Cyclic Prefix for OFDM

Cyclic Prefix (CP), as one of the major overheads in OFDM systems, is proposed to resolve the ISI and ICI induced by channel dispersion [42,43]. A cyclic prefix was generated by either padding a copy of the tail samples to the front or a copy of the head samples to the back, as illustrated in Fig. 2.5. CD and PMD will cause the subcarriers to drift relatively to each other. CP could prevent power leakage from neighbouring OFDM symbols.

Fig. 2.6 shows the OFDM signal with the guard interval at transmitter and receiver side. It can be seen from the figure that the slow subcarriers (e.g., purple) is still maintained within the DFT window as a portion of the CP has

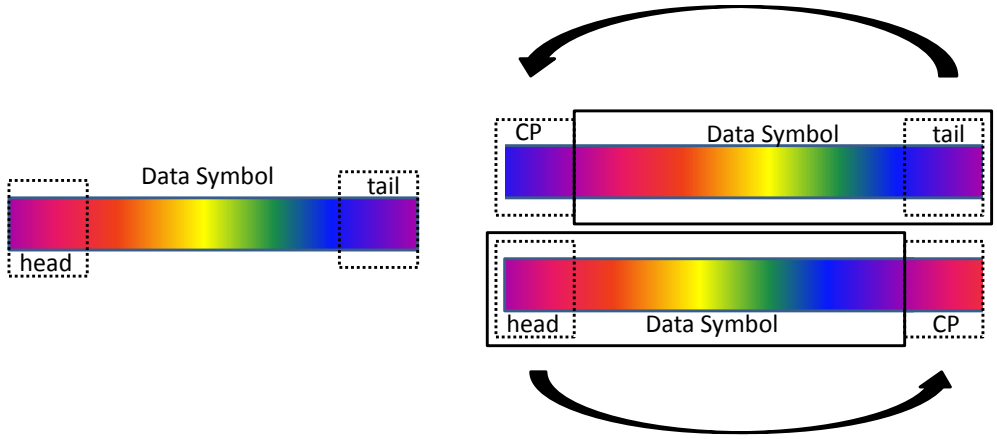

Figure 2.5: Cyclic prefix generation of an OFDM symbol

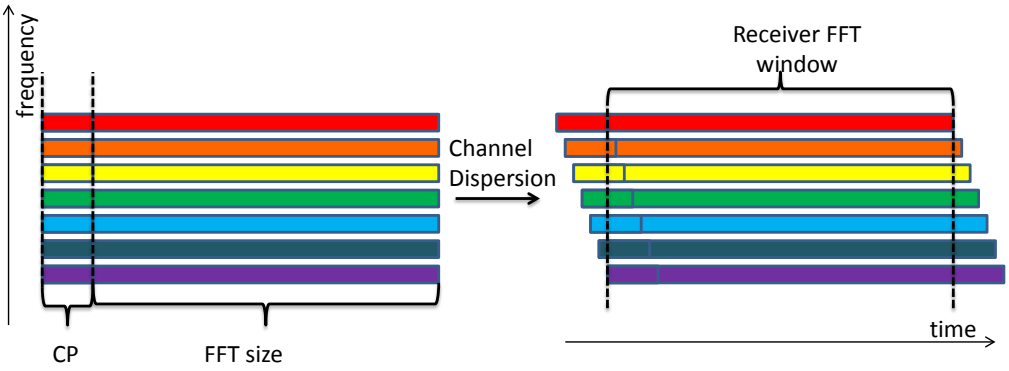

Figure 2.6: OFDM symbol with cyclic prefix undergoes channel dispersion

moved into the DFT window to replace the portion of identical part that has shifted out. The slow subcarriers at the receiver side will appear almost the same as the transmitted signal except with an additional phase shift. The phase shift can be removed via channel estimation and compensation. To ensure zero ISI, the cyclic prefix allocated must be larger than the walk-off of the transmission

link:

$$\Delta_G > t_d \tag{2.14}$$

$$t_d = DB_d c/f^2 + DGD_{max} \tag{2.15}$$

where D is the accumulated chromatic dispersion, B_d is the total bandwidth of the signal, c is the speed of light, f is the central frequency of the OFDM signal and DGD_{max} represents the maximum differential group delay (DGD) of the link.

2.3 Linear Distortions of Optical Channel

The optical channel consists of multiple spans of single-mode fiber (SMF), with amplification (and dispersion compensation) after each span. Assuming linear distortions only and no polarization-dependent loss (PDL), the signal is corrupted by PMD, group velocity dispersion (GVD) and amplified spontaneous emission (ASE) noise. The received samples through such a linear optical channel can be expressed as [24]:

$$\mathbf{y}_n = \sum_{l=0}^{L-1} \mathbf{h}_l \mathbf{x}_{n-l} + \mathbf{w}_n \tag{2.16}$$

where $\mathbf{h}_l$ is the 2×2 channel impulse response matrix accounting for PMD, GVD, DACs and ADCs, as well as transmit and receive filters assuming that no ISI arises in back-to-back (b2b) case. The two components of $\mathbf{w}_n$ are independent and identically distributed complex Gaussian random variables each with

zero mean and two-sided power spectral density (PSD) equal to N_0. n and l are time index. As in [25], we assume a finite impulse response of length L samples. Although the impulse response of a fiber has an infinite duration, it decays to zero for increasing values of l due to its finite energy. Hence, L is chosen such that the energy of the impulse response leaking outside the range of $0 \leq l < L$ is negligible.

We denote by $\mathbf{X}_{k,i}$ the frequency-domain complex modulation symbol of k-th subcarrier and i-th symbol, with $k = 0, 1, \cdots, N-1$, where N is the employed DFT size. A few side subcarriers are set to zero for oversampling purpose, i.e., $\mathbf{X}_k = [0,0]^T, k = N'/2, \cdots, N - N'/2 - 1$, where N' is the number of data (nonzero) subcarriers. The time-domain samples of the transmitted signal are obtained from taking IDFT transform of the frequency domain complex symbols:

$$\mathbf{x}_{(N+N_{cp})i+n} = \frac{1}{\sqrt{N}} \sum_{k=0}^{N-1} \mathbf{X}_{k,i} e^{j2\pi kn/N}, (n = N_{cp}, \cdots, N + N_{cp} - 1) \quad (2.17)$$

where N_{cp} is the length of the cyclic prefix. The continuous-time transmitted signal is obtained from the corresponding discrete-time sequence through a continuous-time pulse, which includes explicit filtering, implicit filtering carried out by DAC and the amplifier, etc [24]. The transmitted signal undergoes linear distortions as modeled in Eq. 2.16:

$$\mathbf{y}_{(N+N_{cp})i+n} = \sum_{l=0}^{L-1} \mathbf{h}_l \mathbf{x}_{(N+N_{cp})i+n-l} + \mathbf{w}_{(N+N_{cp})i+n} \quad (2.18)$$

At the receiver side, the discrete-time sequence after CP removal is fed to

an OFDM demodulator, whose frequency-domain complex output symbols are obtained by DFT transform:

$$\mathbf{Y}_{k,i} = \frac{1}{\sqrt{N}} \sum_{n=N_{cp}}^{N+N_{cp}-1} \mathbf{y}_{(N+N_{cp})i+n} e^{-j2\pi kn/N} \tag{2.19}$$

An OFDM frame usually consists of several training symbols (1-3) and data symbols (30-50). The impulse response is usually assumed to vary slowly so that it is constant over the duration of an OFDM frame. Assuming CP is longer than the impulse response (i.e., $N_{cp} \geq L-1$), we have:

$$\mathbf{Y}_{k,i} = \mathbf{H}_k \mathbf{X}_{k,i} + \mathbf{W}_{k,i} \tag{2.20}$$

where $\mathbf{W}_{k,i}$ are the frequency-domain additive noise samples and the frequency-domain channel response corresponding to the k-th subcarrier is:

$$\mathbf{H}_k = \sum_{l=0}^{L-1} \mathbf{h}_l e^{-j2\pi lk/N} \tag{2.21}$$

We remark that, if either one of the assumptions above does not hold, Eq. 2.20 is no longer true and ICI appears among the subcarriers. Besides ICI, inter-OFDM-symbol interference also arises when CP is shorter than the impulse response. CP represents a source of overhead, and the loss in terms of energy and spectral efficiency is $N_{cp}/(N' + N_{cp})$.

Channel coefficients $\mathbf{H}_k$ are unknown at the receiver. In practice, pilot symbols are periodically inserted into the transmitted OFDM frame, and used by the receiver for channel estimation and compensation. Besides CP, pilot symbols

represent a further source of overhead.

2.3.1 Carrier Frequency Offset Effect

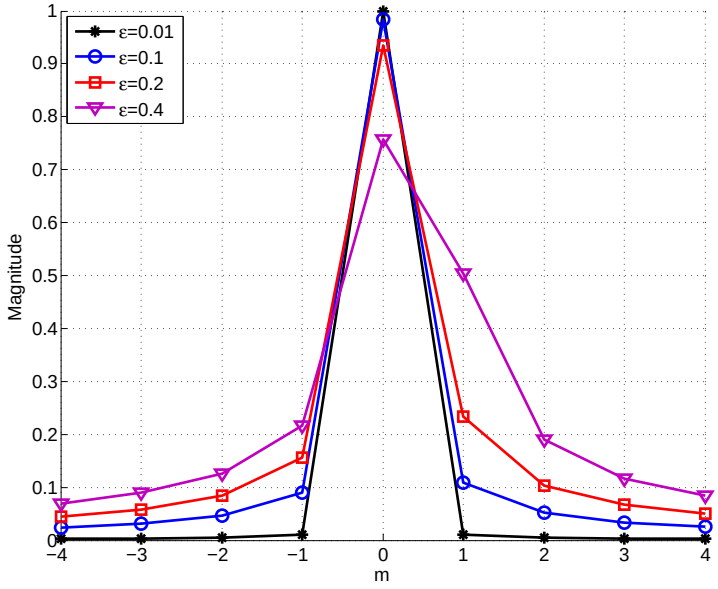

Figure 2.7: Magnitude of the coefficients Ψ_m for 256 DFT size and different values of ϵ (CFO)

Carrier frequency offset (CFO) is caused by the frequency difference between the transmitter and receiver lasers. In the presence of CFO, the n-th received samples are:

$$\mathbf{y}_n = e^{j2\pi n\epsilon/N} \sum_{l=0}^{L-1} \mathbf{h}_l \mathbf{x}_{n-l} + \mathbf{w}_n \tag{2.22}$$

where ϵ is the CFO normalized by the subcarrier spacing f_0: $\Delta f = \epsilon f_0$. The received frequency-domain sample corresponding to the k-th subcarrier can be written as:

$$\mathbf{Y}_k = \sum_{l=0}^{N-1} \Psi_{k-l}^{CFO} \mathbf{H}_l \mathbf{X}_l + \mathbf{W}_k \tag{2.23}$$

where the OFDM symbol index i is omitted for simplicity and Ψ_m^{CFO} is defined by [44]:

$$\Psi_m^{CFO} = \frac{1}{N}\frac{\sin(\pi(\epsilon - m))}{\sin(\pi(\epsilon - m)/N)} e^{j\pi(\epsilon - m)(1-\frac{1}{N})} \tag{2.24}$$

The magnitude of the ICI coefficients due to CFO is calculated as:

$$|\Psi_m^{CFO}| = \frac{1}{N}\frac{\sin(\pi\epsilon)}{\sin(\pi(\epsilon - m)/N)} \tag{2.25}$$

We plot the magnitude of Ψ_m for $m = 0, \pm1, \pm2, \pm3$ and for different values of ϵ in Fig. 2.7. From the figure, we can observe that ICI is almost fully suppressed when ϵ is as small as 0.01. To suppress ICI, the residual CFO must be order of magnitudes smaller than the subcarrier spacing, i.e., $\Delta f \approx 1\% \times f$.

2.3.2 Linear Phase Noise Effect

Linear phase noise (LPN) is induced by transmitter and receiver lasers, whose linewidth ranges from a few hundred kHz for external cavity lasers to a few MHz for distributed-feedback lasers. In the presence of LPN, the n-th received samples are:

$$\mathbf{y}_n = e^{j\phi_n} \sum_{l=0}^{L-1} \mathbf{h}_l \mathbf{x}_{n-l} + \mathbf{w}_n \tag{2.26}$$

where ϕ_n is a Wiener process, modeled by:

$$\phi_n = \phi_{n-1} + v_n \tag{2.27}$$

where $\{v_n\}$ is a set of independent and identically distributed, zero-mean Gaussian random variables, each with variance equal to $2\pi v T_s$. v is the combined

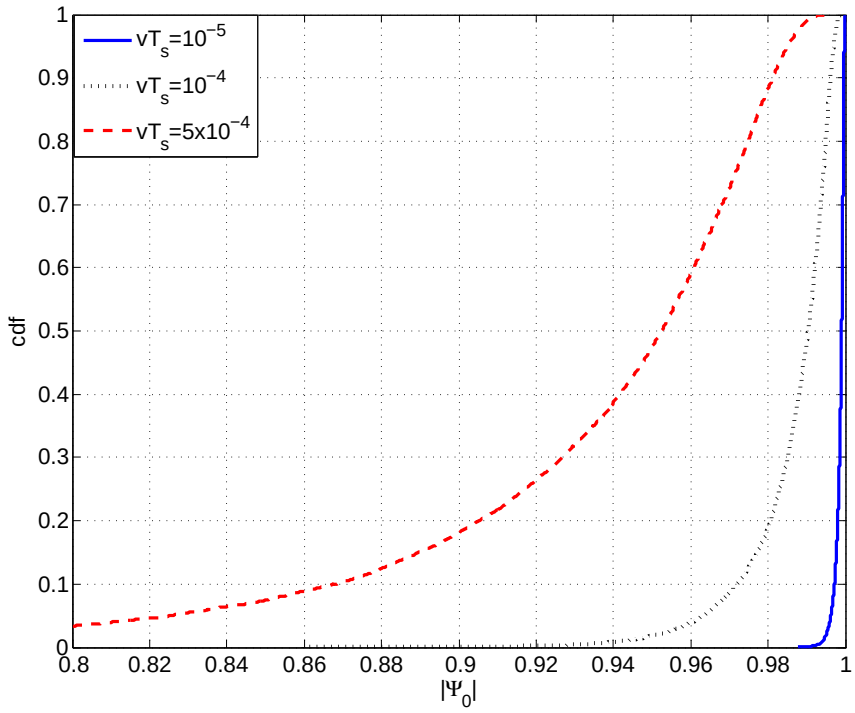

Figure 2.8: Magnitude of the coefficient Ψ_0 for 256 DFT size and different values of vT_s (LPN)

laser linewidth and T_s is the sample time interval. The received frequency-domain samples in the presence of LPN are:

$$\mathbf{Y}_k = \sum_{l=0}^{N-1} \Psi_{k-l}^{LPN} \mathbf{H}_l \mathbf{X}_l + \mathbf{W}_k \tag{2.28}$$

with Ψ_m^{LPN} being:

$$\Psi_m^{LPN} = \frac{1}{N} \sum_{n=N_{cp}}^{N+N_{cp}-1} e^{j\phi_n} e^{-j2\pi mn/N} \tag{2.29}$$

Eq. 2.28 can be rewritten as:

$$\mathbf{Y}_k = \Psi_0 \mathbf{H}_k \mathbf{X}_k + \mathbf{I}_k + \mathbf{W}_k \tag{2.30}$$

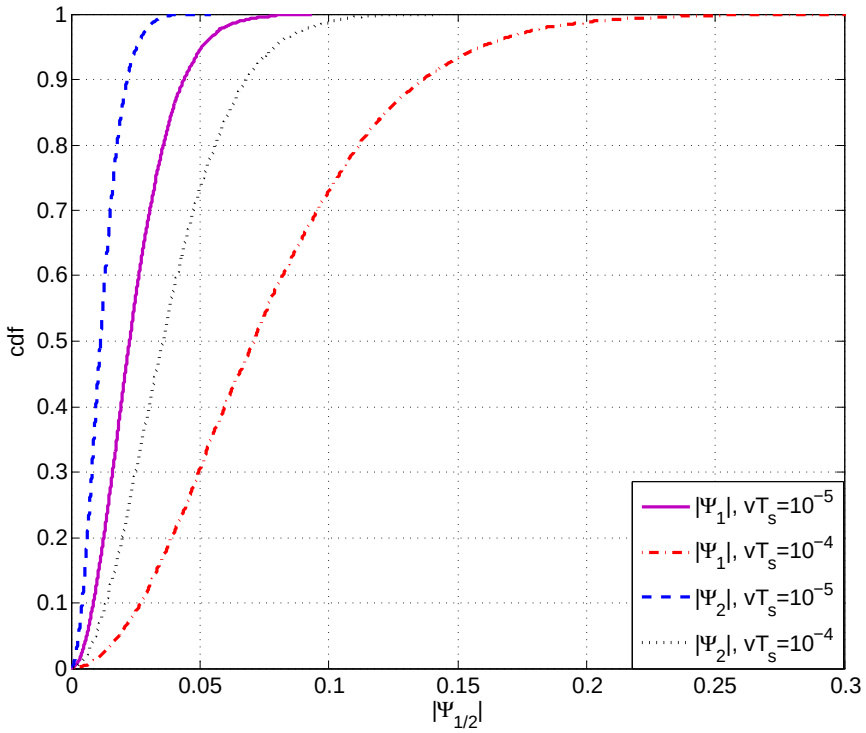

Figure 2.9: Magnitude of the coefficients Ψ_1 and Ψ_2 for 256 DFT size and different values of vT_s (LPN)

where $\Psi_0 = |\Psi_0|e^{j\phi_{cpe}}$ and ϕ_{cpe} is defined as the common phase error (CPE) while $\mathbf{I}_k = \sum_{l=0,l\neq k}^{N-1} \Psi_{k-l}\mathbf{H}_l\mathbf{X}_l$ represent the intercarrier interference (ICI) induced by LPN.

In Fig. 2.8, we plot the cumulative distribution function (cdf) of $|\Psi_0|$ through Monte-Carlo simulation for different values of vT_s. As can be seen from the figure, the value of $|\Psi_0|$ deviates more from 1 as the laser linewidth gets larger. We show the cdf of $|\Psi_1|$ and $|\Psi_2|$ in Fig. 2.9. The amplitude of Ψ_1 and Ψ_2 gets closer to zero with smaller laser linewidth. If the phase noise is sufficiently slow so that $|\Psi_0| \approx 1$ and $|\Psi_1| \approx 0$, the ICI term is negligible and there remains only a common phase rotation on the received symbol.

In high-speed coherent optical communications, PMD usually varies slowly

enough so that the resulting ICI is negligible. Its coherence time is orders of magnitude larger than any reasonable OFDM symbol duration. However, CFO and LPN vary relatively fast and might result in remarkable ICI. Thus, it is of high importance that CFO and LPN are compensated for in CO-OFDM system.

2.3.3 IQ Mismatch Effect

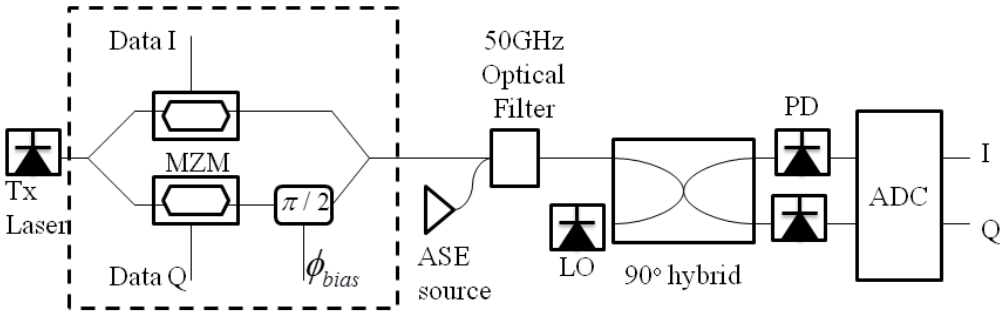

Figure 2.10: Coherent optical QPSK system with detailed modulator and hybrid structure

IQ mismatch would destroy the orthogonality between the two received channels and degrade performance of the system. Phase and amplitude imbalance may be caused by various factors [2]: incorrect bias points settings for the I-, Q- and phase ports, imperfect splitting ratio of couplers, photodiodes responsivity mismatch and mis-adjustment of the polarization controllers.

Fig. 2.10 shows an example of coherent optical QPSK system with detailed modulator and hybrid structure. The optical field equation at the output of the optical QPSK modulator is given by [2]:

$$E_{mod} = \frac{E_{in}}{2}\left\{ \cos\left(\frac{\pi}{2}\frac{V_I + V_{bI}}{V_\pi}\right) + \exp(j\phi_{bias}) \cos\left(\frac{\pi}{2}\frac{V_Q + V_{bQ}}{V_\pi}\right)\right\} \quad (2.31)$$

where V_I and V_Q are the drive voltages, V_{bI} and V_{bQ} are the bias voltages, and ϕ_{bias} is the phase bias between the I and Q branches in the modulator. Incorrect bias points settings for the I-, Q- and phase ports would cause transmitter IQ mismatch.

An optical 90° hybrid mixes the incoming signal with the local oscillator (LO) laser output. However, the phase difference of two output signals may deviate from 90° when the optical hybrid is imperfect [45]. The quadrature imbalance may cause amplitude and phase errors in the output photocurrents. The coherently detected in-phase and quadrature components can be represented as:

$$r_I \propto \Re_e\{E_s E_{LO}^*\} \tag{2.32}$$

$$r_Q \propto \Im_m\{Es E_{LO}^* \exp(j\theta)\} \tag{2.33}$$

where E_{LO}, E_s are the amplitude of the LO and signal, respectively. $\Re_e$ and $\Im_m$ denote the real and imaginary operator. Nonzero θ represents the non-orthogonality between I and Q. Both phase and amplitude imbalance may be caused by non-ideal optical hybrid, which is defined as receiver IQ mismatch. More detailed formulation of OFDM signals under Tx or Rx IQ mismatch could be found in chapter 5.

Gram-Schmidt orthogonalization procedure (GSOP) was first proposed to correct for non-orthogonality in CO-OFDM system [2]. GSOP transforms two non-orthogonal components ($r_I(t)$ and $r_Q(t)$) into a new pair of orthonormal

signals ($I_o(t)$ and $Q_o(t)$):

$$I_o(t) = \frac{r_I(t)}{\sqrt{P_I}} \tag{2.34}$$

$$Q'(t) = r_Q(t) - \frac{\rho r_I(t)}{P_I} \tag{2.35}$$

$$Q^o(t) = \frac{Q'(t)}{\sqrt{P_Q}} \tag{2.36}$$

where $\rho = E\{r_I(t) \cdot r_Q(t)\}$ is the correlation coefficient, $P_I = E\{r_I^2(t)\}$, $P_Q = E\{Q_I'^2(t)\}$ and $E\{\cdot\}$ denotes the ensemble average operator.

In this section, we have described and modeled linear distortions in CO-OFDM system, including linear channel distortion (CD/PMD) and linear front-end non-idealities (carrier frequency offset, linear phase noise and IQ mismatch effects). In this thesis, we will focus on designing DSP algorithms for combatting front-end non-idealities in CO-OFDM system.

2.4 LDPC Encoding and Decoding

OFDM offers an efficient way to deal with CD and PMD. Accoring to [21], the FWM between different subcarriers and its interplay with CD and PMD will result in different subcarriers being affected differently. In order to avoid the overall BER being dominated by the BER of the worst subcarriers, the use of FEC is important.

Reed-Solomon (RS) (255,239) code is commonly considered as the first-generation of FEC [46]. Bose-Chaudhuri-Hocquenghem (BCH), RS or convolutional codes may be combined into more powerful FEC schemes, such as the concatenation of two RS codes or cancatenation of RS and convolutional codes.

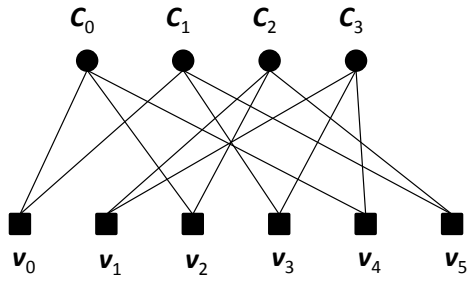

Figure 2.11: The Tanner graph associated with the parity-check matrix $\mathbf{A}$

Different concatenation schemes are commonly considered as the second generation of FEC [46]. Iteratively decodable codes including turbo codes [46–48] and low-density parity-check (LDPC) codes [49–51] have gained much attention in recent years. LDPC codes were originally proposed in 1962 by Robert Gallager [52]. LDPC codes have been shown to outperform turbo product codes in BER performance while have comparable (or lower) complexity than that of turbo product codes [50, 51]. LDPC codes also have many other advantages: (a) it is parallelizable in hardware; (b) LDPC codes of almost any rate and block-length can be created simply by specifying the shape of the parity check matrix whereas the rate of turbo codes is governed largely by a puncturing schedule; and etc. [52]. The soft iteratively decodable codes (turbo and LDPC codes) are commonly referred to as the third generation of FEC [46].

2.4.1 LDPC Codes Construction and Encoding

LDPC codes are linear block codes for which the parity-check matrix has a low density of ones. We denote the parity check matrix by $\mathbf{A}$ ($\mathbf{A} = [\mathbf{a}_1^T, \cdots, \mathbf{a}_M^T]^T$), where $\mathbf{a}_i = [a_{i,0}, \cdots, a_{i,N-1}](i = 0, \cdots, M-1)$ and $\mathbf{A}$ is an $M \times N$ matrix. N is the length of the code and K ($= N - M$) is its dimension. The corresponding

code rate is $R = K/N$. The graphical representation of LDPC codes is a graph called Tanner (bipartite) graph containing two sets of nodes: N bit nodes which represent the N bits of a codeword and M check nodes representing the parity constraints. Therefore, there are $M = N - K$ check nodes and N bit nodes. The nth bit node is connected to the mth check if $\mathbf{A}_{mn} = 1$. Figure 2.11 shows the Tanner graph representation of the following parity-check matrix:

$$\mathbf{A} = \begin{bmatrix} 1 & 0 & 1 & 0 & 1 & 0 \\ 1 & 0 & 0 & 1 & 0 & 1 \\ 0 & 1 & 1 & 0 & 0 & 1 \\ 0 & 1 & 0 & 1 & 1 & 0 \end{bmatrix} \tag{2.37}$$

For any valid codeword $\mathbf{v} = [v_0, v_1, \cdots, v_{N-1}]$ the checks used to decode the codeword are as follows:

$$c_0 : v_0 + v_2 + v_4 = 0 (\mathrm{mod}\, 2) \tag{2.38}$$

$$c_1 : v_0 + v_3 + v_5 = 0 (\mathrm{mod}\, 2) \tag{2.39}$$

$$c_2 : v_1 + v_2 + v_5 = 0 (\mathrm{mod}\, 2) \tag{2.40}$$

$$c_3 : v_1 + v_3 + v_4 = 0 (\mathrm{mod}\, 2) \tag{2.41}$$

Using Gaussian elimination, we can convert the parity-check matrix $\mathbf{A}$ into its systematic (reduced row echelon) form $\mathbf{H}$:

$$\mathbf{H} = \mathbf{A}_p^{-1}\mathbf{A} = [\mathbf{I}, \mathbf{A}_2] \tag{2.42}$$

where $\mathbf{A}_p$ is the matrix representing elementary row operations. The generator

matrix satisfies $\mathbf{HG} = \mathbf{0}$:

$$\mathbf{G} = \begin{bmatrix} \mathbf{A}_2 \\ \mathbf{I} \end{bmatrix} \tag{2.43}$$

with dimensions of $\mathbf{H}$ and $\mathbf{G}$ being $M \times N$ and $N \times M$, respectively. The codeword $\mathbf{c} = [c_0, c_1, \cdots, c_{N-1}]^T$ is generated from the input signal $\mathbf{u} = [u_0, u_1, \cdots, u_{M-1}]^T$ as follows:

$$\mathbf{c} = \mathbf{G} \cdot \mathbf{u} = \begin{bmatrix} \mathbf{c}' \\ \mathbf{u} \end{bmatrix} \tag{2.44}$$

where the codeword $\mathbf{c}$ is partitioned into two parts: an $(N - M) \times 1$ vector $\mathbf{c}'$ and the original data $\mathbf{u}$. However, the operation of Gaussian elimination is computationally costly when dealing with matrices of large size, with the number of elementary operations of $\mathrm{O}(n^3)$, where n is the matrix dimension. Radford [53] proposed an LU decomposition approach which can greatly reduce the number of elementary operations for LDPC encoding. In this method, $\mathbf{A}$ is partitioned into an $M \times (N-M)$ left part, $\mathbf{J}$, and an $M \times M$ right part, $\mathbf{K}$, after rearranging columns if necessary to make $\mathbf{J}$ non-singular.

$$[\mathbf{J}, \mathbf{K}] \begin{bmatrix} \mathbf{c}' \\ \mathbf{u} \end{bmatrix} = 0 \tag{2.45}$$

Thus, we have:

$$\mathbf{c}' = \mathbf{J}^{-1}\mathbf{K}\mathbf{u} \tag{2.46}$$

In [53], the author propose to compute Eq. 2.46 in two steps: (1) compute $\mathbf{z} = \mathbf{K}\mathbf{u}$ in time proportional to M exploiting the sparseness of $\mathbf{B}$ and (2) compute $\mathbf{c}' = \mathbf{J}^{-1}\mathbf{z}$ in time proportional to M^2. Suppose $\mathbf{L}$ and $\mathbf{U}$ is the lower

and upper triangular decomposition of matrix $\mathbf{A}$. The sparse LU decomposition method is detailed in [53], which only needs to be calculated once for each parity-check matrix. In the second step, the vector $\mathbf{c}'$ is found by solving $\mathbf{Ly} = \mathbf{z}$ (by forward substitution) and $\mathbf{Uc}' = \mathbf{y}$ (by backward substitution), which has the computational complexity of O(M^2). We will implement this sparse LU decomposition-based method for our LDPC encoder in chapter 6.

2.4.2 LDPC Codes Decoding

LDPC decoding is realized using the sum-product algorithm (SPA) [49, 54, 55]. Using log likelihood ratios (LLR) in the implementation of SPA can substantially reduce the required quantization levels [56]. The LLR of a binary valued random variable U is defined as:

$$L(U) = \log \frac{P(U=0)}{P(U=1)} \tag{2.47}$$

where $P(*)$ is the probability of an event. Here, we present the LLR-SPA [57] in table 2.1. Each bit node is assigned a posteriori LLR $L(u_n) = \log\{P(u_n = 0|y_n)/P(u_n = 1|y_n\}$. In the case of equiprobable inputs in AWGN channel, $L(u_n) = 2y_n/\sigma^2$, where σ^2 is the noise variance. Simplified (or efficient) implementations of SPA could be found in the literature [58–60].

2.5 Literature Review

In this section, we review the literature and discuss the motivations for each of the topics. In this section, we will intuitively show the performance degradation

Table 2.1: LLR-SPA

Algorithm Iterative Log Likelihood Decoding Algorithm for Binary LDPC Codes
Parameters: $\mathcal{M}(n)$ denotes the set of check nodes connected to a bit node n $\mathcal{M}(n)\backslash m$ denotes the set $\mathcal{M}(n)$ excluding the m-th check node $\mathcal{N}(m)$ denotes the set of bit nodes connected to a check node m $\mathcal{N}(m)\backslash n$ denotes the set $\mathcal{N}(m)$ excluding the n-th bit node $q_{n\to m}(x), x \in \{0,1\}$ denotes the message that bit node n sends to check node m, based on all the checks involving n except m $r_{m\to n}(x), x \in \{0,1\}$ denotes the message that check node m sends to bit node n, based on all the bits checked by m except n $\lambda_{n\to m} = \log(q_{n\to m}(0)/q_{n\to m}(1))$ $\eta_{m\to n} = \log(r_{m\to n}(0)/r_{m\to n}(1))$ **Input**: $\mathbf{A}$, the received vector $\mathbf{r}$, the maximum number of iterations L, and the channel reliability $L(u_n)$. **Initialization**: Set $\eta_{m\to n}^{[0]} = 0$ for all (m,n) with $\mathbf{A}(m,n) = 1$. Set $\lambda_{n\to m}^{[0]} = L(u_n)$ Set the loop counter $l = 1$. **Check node update**: For each (m,n) with $\mathbf{A}_{m,n} = 1$, compute $\eta_{m\to n}^{[l]} = 2\tanh^{-1}\left\{\prod_{n'\in\mathcal{N}(m)\backslash n}\tanh[\lambda_{n'\to m}^{[l-1]}/2]\right\}$ **Bit node update**:For each (m,n) with $\mathbf{A}_{m,n} = 1$, compute $\lambda_{n\to m}^{[l]} = L(u_n) + \sum_{m'\in\mathcal{M}(n)\backslash m}\eta_{m'\to n}^{[l]}$ For each n, compute $\lambda_n^{[l]} = L(u_n) + \sum_{m\in\mathcal{M}(n)}\eta_{m\to n}^{[l]}$ $l = l + 1$ Make a tentative decision: Set $\hat{c}_n = 0$ if $\lambda_n^{[l]} \geq 0$ and $\hat{c}_n = 1$ otherwise If $\mathbf{A}\hat{\mathbf{c}} = 0$, **Stop**. Otherwise, if number of iterations $< L$, loop to **Check node update** Otherwise, declare a decoding failure and **Stop**

due to each front-end non-ideality in a simulated 112-Gb/s PDM CO-OFDM system with QPSK modulation. The detailed setup of the system is described in [61].

2.5.1 Carrier Frequency Offset

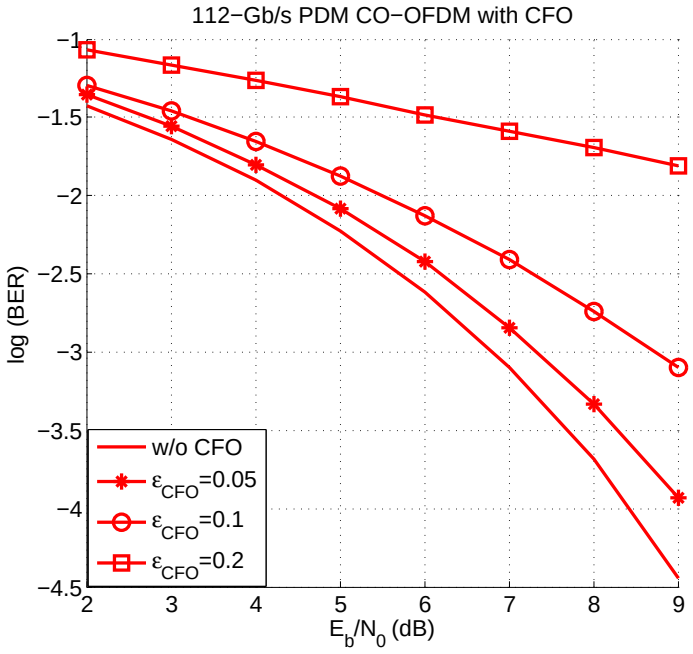

Figure 2.12: Simulated BER of the 112-Gb/s PDM CO-OFDM system with carrier frequency offset without any compensation in the back-to-back case.

In conventional wireless OFDM systems, the carrier frequency offset (CFO) mainly comes from the Doppler effect. In CO-OFDM systems, the CFO is due to the frequency difference between the transmitter (Tx) laser and receiver (Rx) LO. Optical phase-locked loops (PLL) are much more difficult to employ than radio-frequency PLLs, and the frequency stability of photons from semiconductor lasers is much more sensitive to environmental variations [62]. Thus, the major challenges of frequency offset compensation (FOC) include [62]: (1) the

limited budget of computational complexity due to multi-gigabit data operation; (2) the frequency offset value can be more than tens to hundreds of subcarrier spacings; (3) frequency offset varies swiftly in time.

OFDM is more sensitive to carrier frequency offset due to its longer symbol duration, which is N (number of subcarriers) times that of a single carrier system. This calls for accuracy in frequency and phase recovery hundreds or thousands of times better than that in a single carrier system with the same bit rate [63]. Frequency offset compensation, therefore, is one of the most critical functions to implement in OFDM systems. The key challenge in FOC for CO-OFDM system is to estimate the CFO both accurately and efficiently with a full acquisition range.

In Fig. 2.12, we plot the BER versus E_b/N_0 for the simulated system in back-to-back case with different values of carrier frequency offset. PA phase compensation is also employed at the receiver side to remove the CPE caused by the continuous phase drift due to CFO. The CFO Δf is normalized by the OFDM carrier spacing f_0 : $\epsilon_{CFO} = \Delta f/f_0$. We have $f_0 = R_s/N \approx 27$ MHz where R_s is the symbol rate (R_s =56 Gsymbol/s) and N is the DFT size ($N = 2048$). From Fig. 2.12, it is observed that as small as 2.7 MHz carrier frequency offset, if left uncompensated, could result in 2-dB SNR degradation at BER=10^{-3}. In practice, the laser could drift up to a few GHz because of ageing and heating.

The CFO is usually estimated by computing correlation between repeated training symbols [44, 62, 64–66]. However, parameters like the length of repeated symbols (L) [44, 64–66] or sample shift (p) [62] need to be tuned to cover the estimation range (smaller L or p) as well as maintain accuracy (larger

L or p). The CFO can be divided into a fraction and an integer part of the sub-carrier spacing and estimated separately [67–69]. In this kind of approaches, a merit function is usually introduced and the integer part of CFO is estimated by exhaustive search to optimize the merit function over a large number of integer candidates. The searching space would be as large as the FFT size to obtain the full estimation range, resulting in a computationally expensive algorithm. These schemes need to utilize two or more training symbols for FOC, resulting in larger overhead of OFDM systems. Recently, an RF-assisted FOC has been proposed by filtering the optical carrier using narrow pass-band filter whilst achieving better carrier phase recovery [70]. In this approach, the pass-band filter frequency needs to be carefully adjusted according to the systems. The narrow bandwidth of 2 MHz allows less than about 1-MHz tolerance to the shifting of center frequency. In practice, the laser could drift up to a few GHz because of ageing and heating, which would prevent the RF-assisted FOC from being performed automatically.

To overcome the problems of manual parameter tuning, exhaustive search, requirement of multiple training symbols and etc., we propose a novel frequency offset compensation method for CO-OFDM system. Our algorithm can achieve the widest estimation range which is determined by the signal spectrum allocation and receiver bandwidth, by inserting only one pilot-tone at the center of the spectrum. Only one training symbol is needed for CFO acquisition, without the need of exhaustive search or tuning of any parameters.

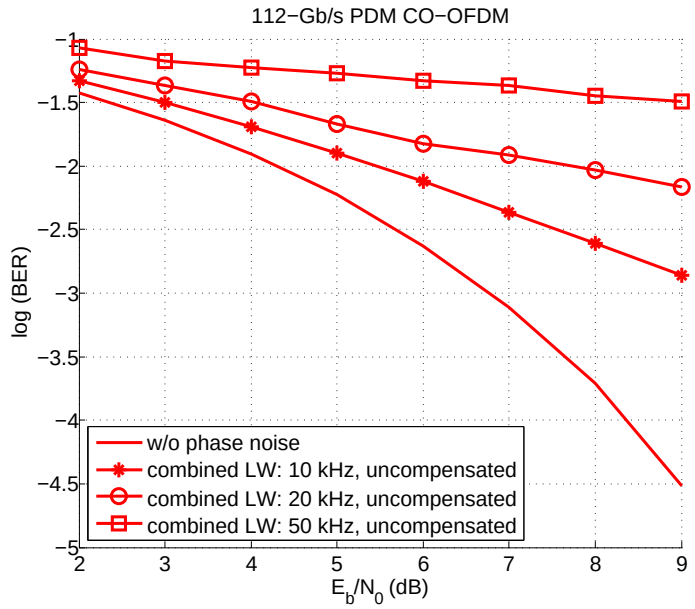

Figure 2.13: Simulated BER of the 112-Gb/s PDM CO-OFDM system with laser phase noise without any compensation in the back-to-back case.

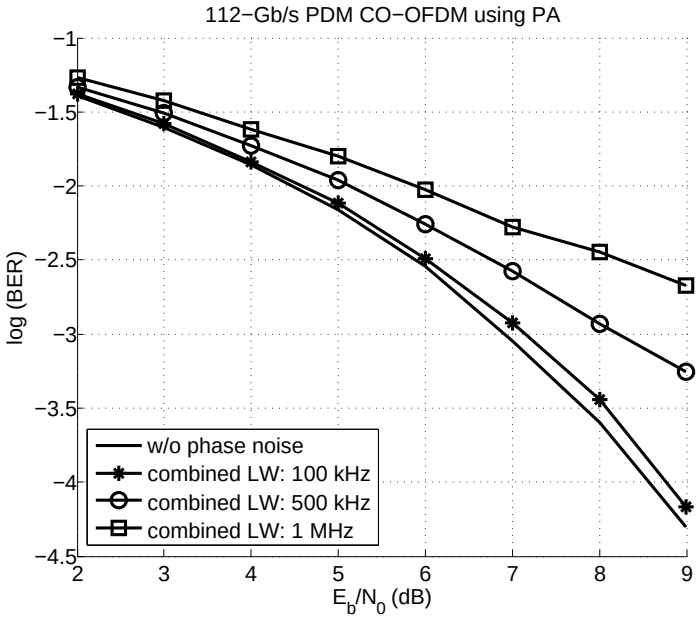

Figure 2.14: Simulated BER of the 112-Gb/s PDM CO-OFDM system with laser phase noise with pilot-subcarrier aided phase compensation [1] in the back-to-back case.

2.5.2 Linear Phase Noise

One of the major challenges in coherent detection is to overcome the carrier phase noise when using a local oscillator (LO) to beat with the received signals to retrieve modulated information. Carrier phase noise is generated by both transmitter laser and receiver local oscillators. An optical phase-locked loop (PLL) is one solution to track the carrier phase with respect to the LO carrier in early days of coherent optical communication. However, an optical PLL operating at optical wavelengths in combination with distributed feedback lasers is quite difficult to implement [71]. With the availability of high-speed analog-to-digital converters (ADCs), the carrier phase estimation can be done in high-speed DSP units rather than using an optical PLL for carrier phase tracking, allowing for free-running LO laser [72]. Uncompensated phase noise will cause common phase error (CPE) and intercarrier interference (ICI) to the received signal after FFT.

Fig. 2.13 shows the BER performance in the presence of uncompensated linear phase noise in the back-to-back case. As observed from the figure, linear phase noise, if left uncompensated, can cause more than 2-dB SNR degradation (at BER=10^{-3}) for a small combined laser linewidth, 10 kHz. A pilot-subcarrier aided (PA) phase compensation method is first introduced in [1, 73], which estimates the CPE based on a few pilot-subcarriers inserted into the OFDM spectrum. Later, a pilot-tone (PT) assisted method [74, 75] monitors the phase noise by the insertion of RF-pilot tone and guard band around it. In this case, the power allocated to the pilot-tone must be carefully selected with a tradeoff between phase estimation accuracy and energy wasted for pi-

lot tone. Decision feedback (DF) methods have also been proposed in the literature [73, 76, 77]. The proposed decision-directed phase estimation (DDPE) in [76,77] use the initial decisions of the current symbol to re-estimate the phase noise, re-compensate and demodulate again, which involves two steps of estimation, compensation and demodulation. Thus, the DDPE method is more computationally intensive than the PA or PT method, yet it suffers from decision errors as it is purely decision directed. A decision-aided (DA) phase estimation method has been proposed for the single carrier system [78, 79]. This method estimated the carrier phase of the current symbol from the decisions of the previous symbols. The CPE estimation methods in the literature are either based on pilots (pilot-subcarriers or pilot-tone) or decision of current symbol. In 4.1, We propose to use the decisions of the previous symbols to aid the phase estimation process for CO-OFDM systems for the first time. We also propose to combine the DA method with PA and DF in a unified framework, to reduce overhead and improve BER performance.

Fig. 2.14 shows the BER curves with PA phase compensation in the back-to-back case of the simulated system. The CPE compensation method greatly improves the BER performance and increases the laser linewidth tolerance compared to Fig. 2.13. However, the compensated curve still exhibits quite high degradation compared to the ideal case, especially when the laser linewidth gets larger (e.g., 500 kHz, 1 MHz). This is because ICI becomes very large and thus non-negligible at high laser linewidth.

In order to better understand and measure the ICI effect, we analytically derive the approximate BER as well as SNR degradation expressions with ideal CPE compensation in 4.1.3. With the help with our analytical equations, one

can easily calculate the BER and tell whether ICI compensation is necessary under certain BER requirement of the system, without running simulations.

All the previous phase compensation works [1, 73–77] assume the ICI to be additive white Gaussian noise and take care of CPE only. However, the correction of the CPE does not always suffice, especially for larger laser linewidth and higher-order modulation format (Fig. 2.14). Methods have been proposed to estimate the higher spectral components of phase noise thus reducing ICI in either wireless [80–82] or optical [83–86] domain. Works including [81–83] compensate for CPE using pilots and make hard decisions first. ICI is then estimated based on the initial decisions, which will suffer from falsely detected symbols. Paper [85] discards pilots and estimates both CPE and ICI in a decision-aided manner by running multiple iterations. Those decision-aided ICI (DA-ICI) compensation methods will suffer from decision errors, resulting in performance degradation. The matched filtering approach in [86] uses adaptive equalization based on an FIR filter which cancels the phase noise. However, it requires as many as $2N$ (N is the DFT size) iterations to converge and the calculation also involves decision statistics. A blind ICI (BL-ICI) compensation scheme over constant amplitude modulation was proposed in [80] for wireless communication. The author partitioned one received OFDM symbol into sub blocks and used the approximate average phase noise over each sub block to cancel ICI. As the wireless time-domain BL-ICI method solves the problem of initial decision errors [81–83] and high computational complexity [86], we propose a new algorithm derived from it for CO-OFDM systems, which could be applied to non-constant amplitude formats, M-QAM in 4.2.

2.5.3 IQ Mismatch

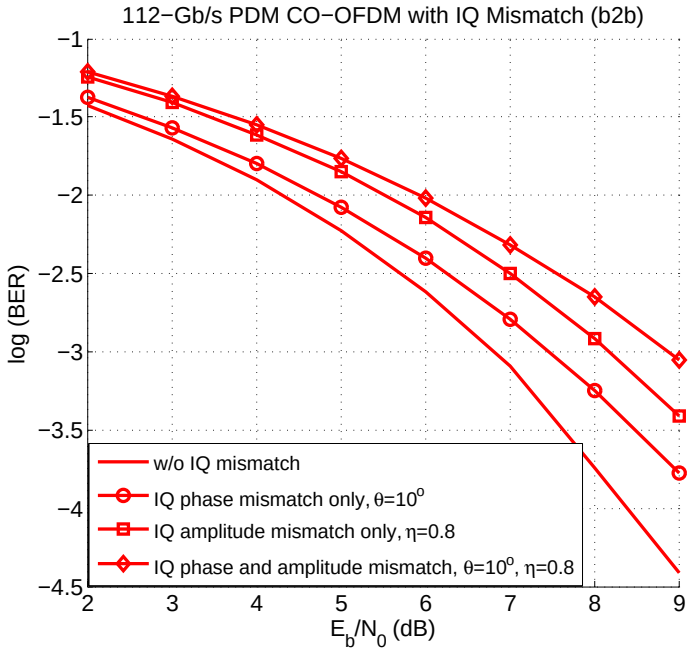

Figure 2.15: Simulated BER of the 112-Gb/s PDM CO-OFDM system with Tx/Rx IQ phase and amplitude mismatch in the back-to-back case.

IQ mismatch is one of the key front-end effects caused by the mismatch in amplitude and phase between I and Q branches. IQ mismatch will cause inter-carrier interference and thus degrade the performance of CO-OFDM system. Fig. 2.15 and Fig. 2.16 show the BER performance of the simulated CO-OFDM system with Tx and Rx IQ mismatch in back-to-back case or after 2 spans of SSMF transmission, respectively. The fiber length L_{SMF}, attenuation α_{SMF}, dispersion D_{SMF}, nonlinear coefficient γ and amplifier noise figure NF are 80 km, 0.2 dB/km, 16 ps/nm/km, 1.3 $\mathrm{W^{-1}km^{-1}}$ and 6 dB respectively. PMD effect is excluded here. For the second case, intra-symbol frequency-domain averaging (ISFA) based channel estimation [61] is employed at the receiver side. For the back-to-back case, Tx and Rx IQ mismatch have identical influence on

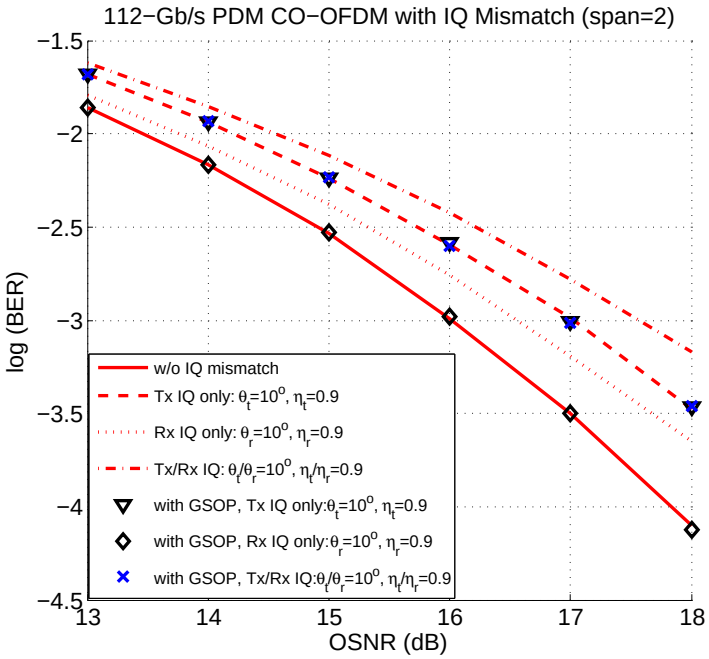

Figure 2.16: Simulated BER of the 112-Gb/s PDM CO-OFDM system with Tx/Rx IQ mismatch with/without GSOP [2, 3] after 2-span transmission.

the system.

As IQ mismatch destroys the orthogonality between the two received branches, Gram-Schmidt orthogonalization procedure (GSOP) was first proposed to compensate for the IQ mismatch in CO-OFDM system [2, 3]. GSOP is a time-domain method which transforms a set of nonorthogonal samples into a set of orthogonal samples. GSOP operating before FFT could effectively remove the Rx IQ mismatch at the Rx side.

Fig 2.16 demonstrates the performance of GSOP in dealing with Tx/Rx IQ mismatch after 2-span of fiber transmission. As shown in the figure, GSOP can effectively remove Rx IQ mismatch while it is not effective in compensating for Tx IQ mismatch in the presence of channel distortion [3]. This is because the correlation between I and Q of the received signal is not only induced by

Tx IQ mismatch, but also caused by channel distortion (CD/PMD). Thus a joint compensation of channel distortion and Tx IQ mismatch is necessary for this case. Recently, a pilot-assisted (PA) compensation method was proposed with a specially-structured pilot [36], which effectively compensates for Tx IQ mismatch in the presence of channel distortion. It inserts a specially structured training symbol at the beginning of the OFDM frame and estimate the IQ mismatch and channel distortion parameters once every OFDM frame. Here, we propose a new compensation method based on both pilot symbols and decision statistics. The channel transfer function and IQ mismatch factor are estimated jointly based on two pilot symbols, and updated after each decision-making stage. Our method is superior to the previous methods in several aspects. Firstly, DAJC makes use of standard pilot symbols, which simplifies the design compared to the special pilot structure proposed in [36]. Secondly, the adaptive characteristic of DAJC makes it more robust to time-variant channel and mismatch parameters, and also reduces the requirement on overhead. Last but not least, DAJC performs better than both GSOP and PA, with tolerable and adjustable increase in complexity. As shown in the simulation later, we can adjust the complexity of DAJC by applying the decision-aided stage every D symbols.

2.5.4 LDPC coded OFDM with linear phase noise

LDPC codes, invented by Gallager [52] in 1960s, have been proved to achieve close to Shannon limit performance [49]. LDPC codes are linear block codes for which the parity check matrix has low density of ones. LDPC coded orthogonal frequency division multiplexing (OFDM) is a suitable coded modula-

tion technique for long-haul optical communication [33]. Recently, there have been quite a few experimental demonstrations using LDPC coded coherent optical OFDM (CO-OFDM) for high speed long-haul transmission [34, 35]. The performance of decoding algorithms depends on the calculation of the decoding metric, i.e., the log-likelihood ratio (LLR). In the presence of linear phase noise, phase compensation is usually performed first, followed by LDPC decoding using the conventional LLR [34, 35, 87]. In Pol-Mux LDPC coded coherent OFDM transmission [87], the authors also describe how to determine the symbol's log-likelihood ratios in the presence of laser phase noise numerically. The average likelihood function was obtained over all possible values of phase noise but no analytical expression was given for the final metric.

Linear phase noise, as one of the key front-end non-idealities, is shown to have great impact on the CO-OFDM system performance (2.5.2). It is an interesting problem to study the LDPC coded CO-OFDM system in the presence of linear phase noise. Thus, we propose to investigate its influence on the LDPC coded OFDM system. In order to study the LDPC decoding performance in the presence of linear phase noise, we leave the linear phase noise uncompensated and incorporate it into the calculation of the decoding metric. In the conventional way, the decoding metric of each bit is calculated from the likelihood function conditioned on the received signal which carries that bit. In our proposed derivation, we calculate the decoding metric of each bit from the likelihood function conditioned on both the received signal which carries that bit, and the linear phase noise information. In this way, we have successfully derived new LLR metrics with linear phase noise term for both differential MPSK, coherent MPSK and M-QAM OFDM systems.

This work is also an important part of our thesis topic: digital signal processing for front-end non-idealities in CO-OFDM system. We combine the linear phase noise compensation and LDPC decoding into a one-step algorithm, by deriving a new analytical decoding metric. Although the study is based on a coded OFDM system, the core of our research still belongs to the broader version of DSP algorithms for combatting front-end non-ideality, i.e., the linear phase noise. Moreover, we have successfully demonstrated that our one-step decoding achieves better performance than the conventional two-step way of phase noise compensation plus LDPC decoding for 16-QAM and 64-QAM CO-OFDM signals.

2.6 Conclusion

In this chapter, we have studied the fundamentals of CO-OFDM system, including the mathematical formulation and discrete Fourier transform implementation of OFDM signals, overheads and spectral efficiency of OFDM systems as well as the cyclic prefix (section 2.2). Moreover, the linear distortions of optical channel are discussed in section 2.3. Besides fiber linear impairments such as CD and PMD, front-end non-idealities are the key performance-limiting linear impairments of CO-OFDM system. Carrier frequency offset, linear phase noise and IQ mismatch are the three major front-end non-idealities that deteriorate the OFDM signal. The encoding and decoding methods of LDPC codes are introduced in section 2.4. Finally, we give a brief discussion about the motivations as well as literature review for each sub-topics in the thesis.

In the following chapters 3, 4 and 5, we will propose novel compensa-

tion algorithms for carrier frequency offset, linear phase noise and IQ mismatch, respectively. In chapter 6, new log-likelihood ratios with linear phase noise term are derived for various LDPC coded OFDM formats: differential BPSK(MPSK), pilot-aided BPSK(MPSK) and pilot-aided M-QAM.

Chapter 3

Carrier Frequency Offset Compensation

In conventional wireless OFDM systems, the carrier frequency offset (CFO) mainly comes from the Doppler effect. In CO-OFDM systems, the CFO is due to the frequency difference between the transmitter (Tx) laser and receiver (Rx) LO. Optical phase-locked loops (PLL) are much more difficult to employ than radio-frequency PLLs, and the frequency stability of photons from semiconductor lasers is much more sensitive to environmental variations [62]. Thus, the major challenges of frequency offset compensation (FOC) include [62]: (1) the limited budget of computational complexity due to multi-gigabit data operation; (2) the frequency offset value can be more than tens to hundreds of subcarrier spacings; (3) frequency offset varies swiftly in time.

OFDM is more sensitive to carrier frequency offset due to its longer symbol duration, which is N (number of subcarriers) times that of a single carrier system. This calls for accuracy in frequency and phase recovery hundreds or thou-

sands of times better than that in a single carrier system with the same bit rate. Frequency offset compensation, therefore, is one of the most critical functions to implement in OFDM systems. The key challenge in FOC for CO-OFDM system is to estimate the CFO both accurately and efficiently with a full acquisition range.

The CFO is usually estimated by computing correlation between repeated training symbols [44, 62, 64–66]. However, parameters like the length of repeated symbols (L) [44, 64–66] or sample shift (p) [62] need to be tuned to cover the estimation range (smaller L or p) as well as maintain accuracy (larger L or p). The CFO can be divided into a fraction and an integer part of the subcarrier spacing and estimated separately [67–69]. In this kind of approaches, a merit function is usually introduced and the integer part of CFO is estimated by exhaustive search to optimize the merit function over a large number of integer candidates. The searching space would be as large as the FFT size to obtain the full estimation range, resulting in a computationally expensive algorithm. These schemes need to utilize two or more training symbols for FOC, resulting in larger overhead of OFDM systems. Recently, an RF-assisted FOC has been proposed by filtering the optical carrier using narrow pass-band filter whilst achieving better carrier phase recovery [70]. In this approach, the pass-band filter frequency needs to be carefully adjusted according to the systems. The narrow bandwidth of 2 MHz allows less than about 1-MHz tolerance to the shifting of center frequency. In practice, the laser could drift up to a few GHz because of ageing and heating, which would prevent the RF-assisted FOC from being performed automatically.

In this chapter, we propose a novel frequency offset compensation method

for CO-OFDM system. The method is composed of a correlation-based method for the fraction part estimation and a pilot-tone-assisted method for the integer part estimation. Our algorithm can achieve the widest estimation range which is determined by the signal spectrum allocation and receiver bandwidth, by inserting only one pilot tone at the center of the spectrum. The fraction part of the CFO is calculated simultaneously with time synchronization, whereas the integer part of the CFO is estimated by counting the shifted positions of the pilot tone in the received spectrum. Only one training symbol per OFDM frame is needed for CFO acquisition, without the need of exhaustive search or tuning of any parameters. The typical OFDM frame consists of 20 to 50 symbols and reducing from two training symbols to one training symbol would result in more than 2% reduction in overhead.

The reminder of the chapter is organized as follows. In section 3.1, we describe the principle of our correlation-based and pilot-tone-assisted FOC method. In section 3.2, the experimental results are shown for our FOC method. Subsequently, correlation-based fraction part estimation methods are investigated in the presence of chromatic dispersion and linear phase noise in section 3.3, where analytical expressions and simulation results of error variances are given. In section 3.4, we evaluate the performance of pilot-tone assisted integer part estimation under dispersion and linear phase noise. In section 3.5 we draw the conclusions.

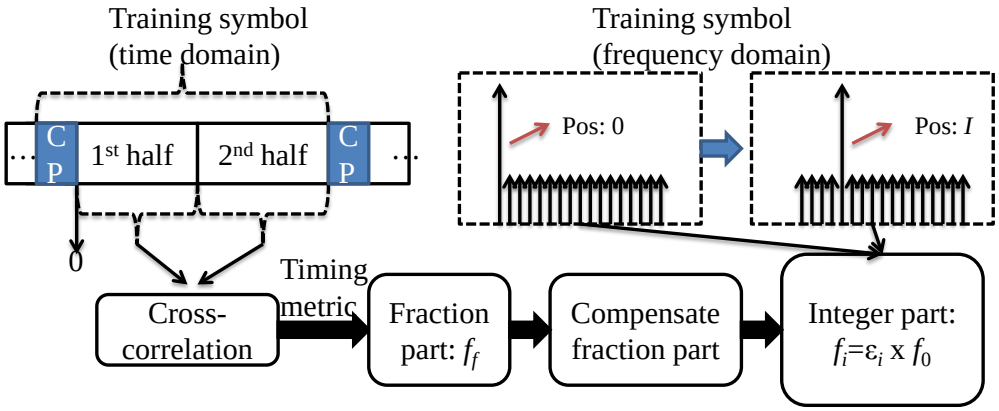

Figure 3.1: The time and frequency domain structure of training symbol

3.1 Principle of FOC Method

The CFO f is normalized by the subcarrier spacing f_0 and divided into the integer and fraction parts: $f = f_i + f_f = \epsilon f_0 = (\epsilon_i + \epsilon_f) f_0$, with ϵ_i being an integer and $|\epsilon_f| \leq 1$. A training symbol is inserted at the beginning of the frame with structure shown in Fig. 3.1. It consists of two identical halves in the time domain and a pilot-tone with larger energy at DC in the frequency domain. At the receiver side, a cross correlation function between the two halves is calculated and the timing metric $M(d)$ is computed as follows:

$$M(d) = \frac{|P(d)|^2}{(R(d))^2} \tag{3.1}$$

$$P(d) = \sum_{m=0}^{N/2-1} y^*_{d+m} y_{d+m+N/2} \tag{3.2}$$

$$R(d) = \sum_{m=0}^{N/2-1} \left| y_{d+m+N/2} \right|^2 \tag{3.3}$$

where $\{y_{d+m}\}$ and $\{y_{d+m+N/2}\}$ $(m = 0, \cdots, N/2-1)$ are the two halves of received training symbol in the time domain and N is the FFT size. The correct

timing offset is found with the maximum timing metric: $d_{max} = \text{argmax}(M(d))$. Assuming perfect window synchronization, the received signal sampled at $i/(Nf_0)$ ($i = 0, 1, \cdots, n, \cdots$) would be:

$$y_{N*i+n} = e^{j2\pi(N*i+n)\epsilon/N + j\phi_{N*i+n}} \sum_{l=0}^{L-1} h_l x_{N*i+n-l} + w_{N*i+n} \tag{3.4}$$

where x_n, h_l, ϕ_n and w_n are the transmitted time domain samples, channel distortion, linear phase noise and additive white Gaussian noise, respectively. Ignoring phase noise and additive noise, there is $\pi\epsilon$ phase shift between the first and second half of the training symbol. Thus, the fraction part of CFO is obtained from cross-correlation between two halves:

$$\epsilon_f = \frac{1}{\pi} \angle \{ \sum_{m=0}^{N/2-1} y_m^* y_{m+N/2} \} \tag{3.5}$$

We first compensate for the fraction part of CFO by multiplying the samples by $\exp(-j2\pi f_0 \epsilon_f t)$. Omitting the symbol index i for simplicity, we can obtain the frequency domain samples as follows:

$$Y_k = \sum_{l=0}^{N-1} \Psi_{k-l} H_l X_l + W_k \tag{3.6}$$

$$\Psi_m = \frac{1}{N} \sum_{n=0}^{N-1} e^{j2\pi n\epsilon/N + j\phi_n} e^{-j2\pi mn/N} \tag{3.7}$$

where X_k, Y_k, H_k and W_k are the frequency domain transmitted symbol, received symbol, channel transfer function and AWGN, respectively. Assuming zero phase noise ($\phi_n = 0$) and that ϵ_f has been compensated for, Ψ_m can be

calculated as:

$$\Psi_m = \frac{1}{N}\frac{\sin(\pi(\epsilon_i - m))}{\sin(\pi(\epsilon_i - m)/N)} e^{j\pi(\epsilon_i - m)(1-\frac{1}{N})} \tag{3.8}$$

With $(\epsilon_i - m)$ being an integer, we can conclude that $\Psi_m = 1$ when $\epsilon_i - m = 0$ and $\Psi_m = 0$ otherwise. The resulted received symbol would be:

$$Y_k = H_{k+\epsilon_i} X_{k+\epsilon_i} + W_k \tag{3.9}$$

From Eq. 3.9, we observe that the uncompensated integer part carrier frequency offset will shift the pilot-tone (peak in the received spectrum) ϵ_i positions away. We can thus calculate ϵ_i by:

$$\hat{\epsilon_i} = \begin{cases} I, & (0 \leq I \leq N/2 - 1) \\ I - N, & (N/2 \leq I \leq N - 1) \end{cases} \tag{3.10}$$

where $I = \text{argmax}_k \, |Y_k| \, (k = 0, \cdots, N-1)$. Note that fiber chromatic dispersion will not affect the energy of the received signal, which is formulated as a constant envelope function $H(\omega) = \exp(-j\omega^2 \beta_2 L/2)$, with L being the entire length of the transmission link and β_2 the GVD coefficient.

3.2 Experimental Demonstration of FOC Method

To investigate the performance of our correlation-based and pilot-tone assisted FOC method, we carry our experiment with setup shown in Fig. 3.2.

The original data are modulated onto 350 subcarriers (subcarrier index: $6 -$

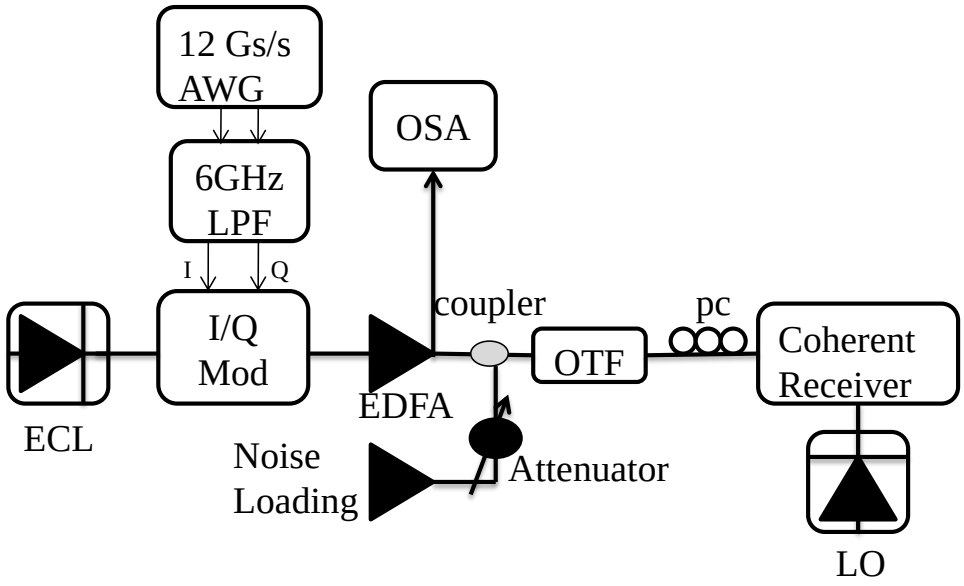

Figure 3.2: The experimental setup (ECL: external cavity laser, AWG: arbitrary waveform generator, LPF: low pass filter, Mod: modulator, OSA: Optical Spectrum Analyzer, OTF: optical tunable filter @ 0.3 nm, pc: polarization controller, LO: local oscillator).

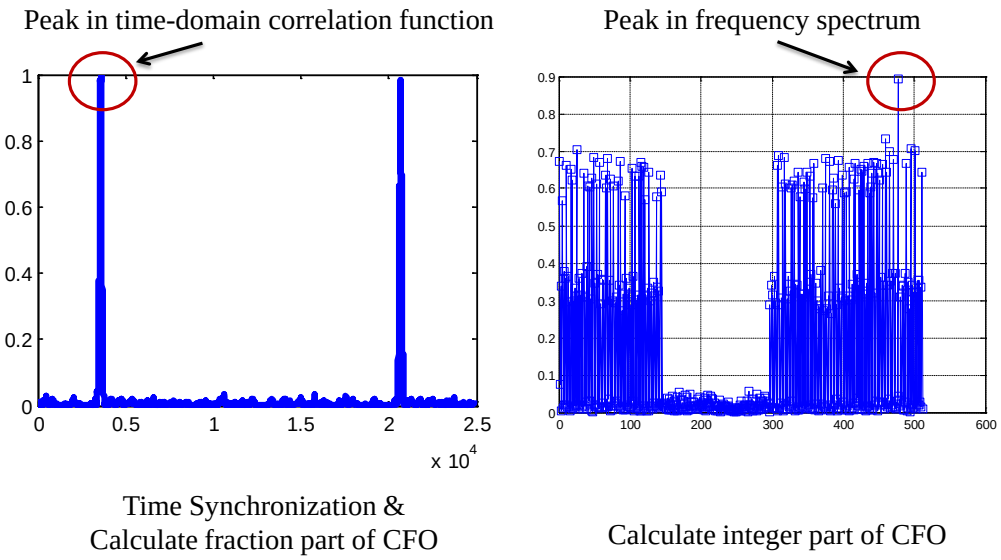

Figure 3.3: Demonstration of time synchronization and FOC using experimental data.

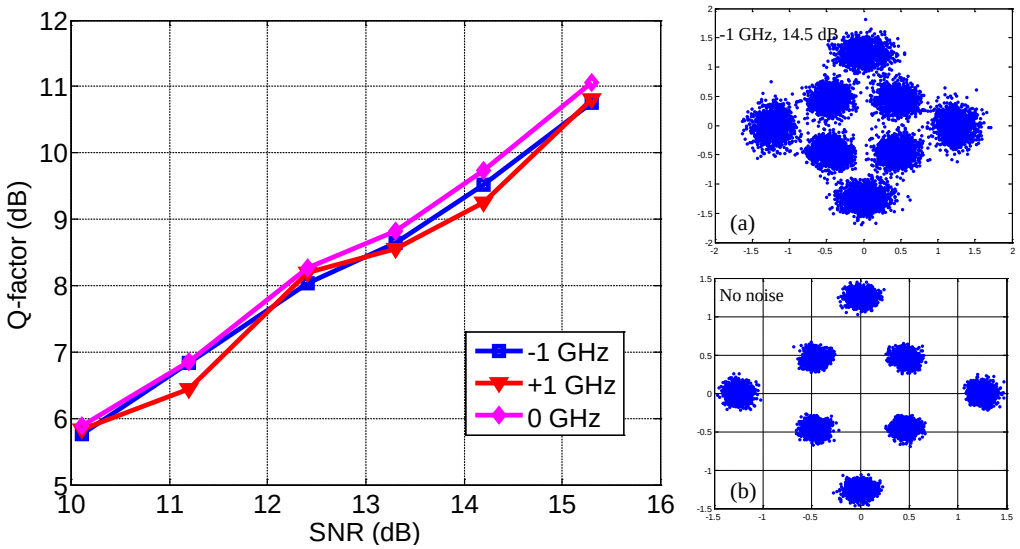

Figure 3.4: Q factor versus SNR for different CFO: 1 GHz, −1 GHz, 0 GHz. Inset: signal constellation with (a) −1-GHz CFO and 14.5-dB SNR; (b) w/o noise

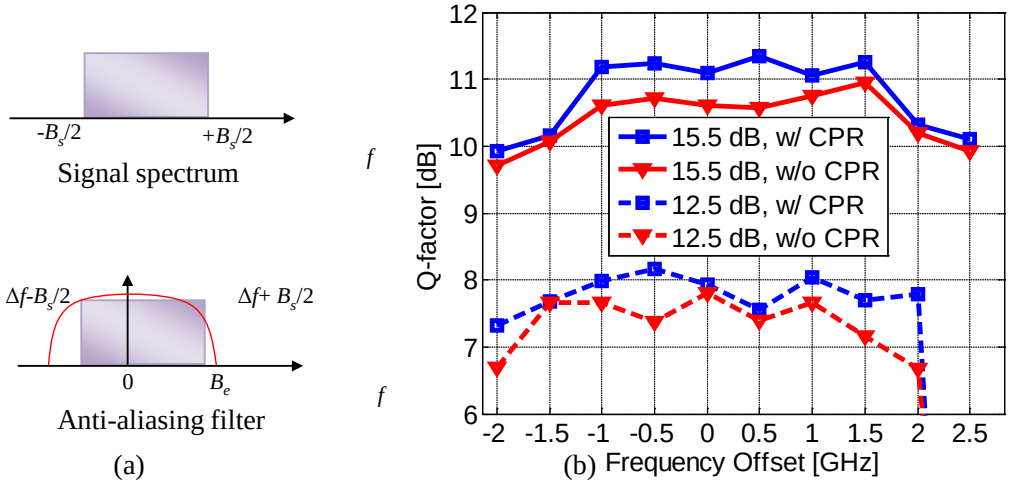

Figure 3.5: (a) Demonstration of signal spectrum and anti-aliasing filter;
(b) Q-factor versus CFO at 15.5-dB or 12.5-dB SNR, with or without carrier phase recovery.

180 and $334-508$) with 8QAM modulation. The data subcarriers, together with 4 pilot subcarriers (subcarrier index: 5, 181, 333 and 509) for phase estimation, are zero-padded and then transferred to the time domain with a FFT/IFFT size of 512. A pilot tone with higher energy (subcarrier index: 1) is inserted into the OFDM spectrum at zero frequency (DC) by adjusting the IQ-modulator bias. The power of the pilot-tone with respect to other data subcarriers is illustrated in Fig. 3.3 (right). Both the transmitter laser and the receiver local oscillator have a linewidth of 100 kHz. A cyclic prefix of 6 samples is added to the symbol. The time-domain samples are generated by a 12-Gsample/s AWG before modulated onto the IQ modulator, resulting in an effective data rate equal to 22.24 Gb/s. The OFDM frame is composed of three training symbols (one for synchronization, and two for channel estimation) and 32 payload data symbols.

As illustrated in Fig. 3.3, time synchronization is achieved by finding the peak of the correlation function in the time domain. The received data is then FFT processed and a peak can be found in the spectrum, which is used to calculate the integer part of CFO. Fig. 3.4 shows the Q-factor versus SNR for different values of CFO: +1 GHz, -1 GHz and 0 GHz. As shown in the figure, no performance degradation is observed due to CFO, which demonstrates the effectiveness and robustness of our proposed scheme. The subcarrier spacing f_0 in the experiment is 23.44 MHz. Thus 1 GHz corresponds to (42+2/3) f_0.

Fig. 3.5(a) demonstrates the maximum CFO that an OFDM system can tolerate. Supposing that an OFDM signal covers a bandwidth of B_s, its maximum bandwidth can only go up to the bandwidth of a digital-to-analog converter (DAC) which generates the OFDM signal. Here we use R_s to denote the sampling rate of the DAC. In other words, $B_s \leq R_s$. At the receiver side, af-

ter down-converting the OFDM signal into electrical domain, an anti-aliasing low-pass filter is necessary to prevent frequency overlapping when sampling the received signal back to R_s samples per second. The bandwidth of the low-pass filter is also capped at $R_s/2$ to avoid potential aliasing issue. Furthermore, CFO is quite severe in fiber optic communication due to the laser instability. In a practical system, it is very difficult to maintain the laser frequency with a small frequency offset because commercially available lasers have frequency stability within ± 2.5 GHz [88]. As a result, the OFDM signal is designed to have guard band to avoid the power loss because of the filtering from anti-aliasing low-pass filter at the receiver side. This guard band will determine the maximum CFO which the OFDM signal can tolerate. For example, when the B_s is only half of the total DAC bandwidth and anti-aliasing filter bandwidth is set at its maximum, i.e., $B_s = R_s/2$ and $B_e = R_s/2$, the CFO range of this designed OFDM system can vary from $-R_s/4$ to $+R_s/4$. Based on this design procedure of the OFDM systems, the proposed pilot-assisted FOE could have this full-range estimation with high accuracy, which is from -1.5 GHz to 1.5 GHz in the experiment. Fig. 3.5(b) shows the Q-factor versus CFO up to ± 2 GHz with SNR at 12.5 dB or 15.5 dB, and with or without carrier phase recovery (CPR) [89]. In addition to CFO, linear phase noise, which is a Wiener process, keeps rotating the phase of the transmitted signals. To retrieve the correct phase modulation, CPR is employed to remove the linear phase noise and improve the Q factor [89]. When the absolute value of CFO is smaller than 1.5 GHz, the Q-factor degradation is within 1 dB. Severe degradation only occurs when the absolute value of CFO is beyond 1.5 GHz, which is consistent with our analysis.

3.3 Performance Evaluation of Correlation-based Estimator

In our FOC method, the correlation-based fraction part estimator is based on the Schmidl estimator [67]. In this section, we investigate the performance of correlation-based fraction part estimators in the presence of chromatic dispersion and linear phase noise. Here, we will analytically derive the estimation variance in the presence of linear phase noise for the estimators. Three methods (Schmidl [67], Moose [44] and CP [90]) are included, and the derivation can be easily extended to other estimators. To our knowledge, there is no other work on this topic in the literature. The analytical expressions are confirmed through simulation. CP method is found to be the most robust to linear phase noise among the three. Furthermore, we investigate the performance of correlation-based methods under different amount of chromatic dispersion. Schmidl and Moose estimators are robust to dispersion whereas the CP estimator degrades severely in the presence of dispersion.

For fair comparison, we modify the Schmidl [67] method to include two identical training symbols instead of one. Ignoring phase noise and additive noise, there is $2\pi\epsilon$ phase shift between the first and second training symbol, both in time and frequency domain. Thus, the maximum likelihood estimation is obtained from cross-correlation between two received symbols:

$$\hat{\epsilon}_{Schmidl} = \frac{1}{2\pi}\angle\Big\{\sum_{n=0}^{N-1} y_{N+n}y_n^*\Big\} \tag{3.11}$$

$$\hat{\epsilon}_{Moose} = \frac{1}{2\pi}\angle\Big\{\sum_{k=0}^{N-1} Y_{k1}Y_{k0}^*\Big\} \tag{3.12}$$

where the two equations are the definition of Schmidl [67] and Moose [44] estimators, respectively. Taking the effect of CP into consideration, the actual carrier frequency offset is $\Delta f = \epsilon f_0 N/(N+CP)$. Similarly, the CP estimator [90] takes cross-correlation between the cyclic prefix and the data from which cyclic prefix is generated. A better estimation can be achieved by taking average over D consecutive symbols:

$$\hat{\epsilon}_{CP} = \frac{1}{2\pi} \angle \Big\{ \sum_{d=0}^{D-1} \sum_{n=0}^{CP-1} y_{(N+CP)*d+n+N} y^*_{(N+CP)*d+n)} \Big\} \tag{3.13}$$

We rewrite the relationship between the two training symbols of Schmidl estimator as follows:

$$y_n = r_n + w_n \tag{3.14}$$

$$y_{N+n} = r_n e^{j2\pi\epsilon + j(\phi_{N+n} - \phi_n)} + w_{N+n} \tag{3.15}$$

where $r_n = e^{j2\pi n\epsilon/N + j\phi_n} \sum_{l=0}^{L-1} h_l x_{n-l}$ according to Eq. 3.4. Following a similar approximation in [67], we can derive the estimation variance for Schmidl estimator from the tangent of the phase error:

$$\tan[2\pi(\hat{\epsilon}_{Schmidl} - \epsilon)] = \frac{\sum_{n=0}^{N-1} \mathrm{Im}[y_{N+n} y_n^* e^{-2\pi j\epsilon}]}{\sum_{n=0}^{N-1} \mathrm{Re}[y_{N+n} y_n^* e^{-2\pi j\epsilon}]} \tag{3.16}$$

For $|\hat{\epsilon}_{Schmidl} - \epsilon| \ll 1/2\pi$, Eq. 3.16 can be approximated as:

$$\hat{\epsilon}_{Schmidl} - \epsilon \approx \frac{1}{2\pi} \frac{\sum_{n=0}^{N-1} \mathrm{Im}[(r_n e^{j(\phi_{N+n} - \phi_n)} + w_{N+n} e^{-2\pi j\epsilon})(r_n^* + w_n^*)]}{\sum_{n=0}^{N-1} \mathrm{Re}[(r_n e^{j(\phi_{N+n} - \phi_n)} + w_{N+n} e^{-2\pi j\epsilon})(r_n^* + w_n^*)]} \tag{3.17}$$

With high signal-to-noise ratio, Eq. 3.17 may be further approximated by:

$$\hat{\epsilon}_{Schmidl} - \epsilon \approx \frac{\Delta\phi_{Schmidl}}{2\pi} + \frac{\sum_{n=0}^{N-1} \mathrm{Im}(w_{N+n} r_n^* e^{-j2\pi\epsilon} + r_n w_n^*)}{2\pi \sum_{n=0}^{N-1} |r_n|^2} \tag{3.18}$$

$$\mathrm{Var}[\hat{\epsilon}_{Schmidl}] = \frac{\sigma^2_{Schmidl} + N_0/(NE_s)}{(2\pi)^2} \tag{3.19}$$

where $\Delta\phi_{Schmidl} = 1/N \sum_{n=0}^{N-1}(\phi_{N+n} - \phi_n)$ and $E_s = |r_n|^2$ is the symbol energy. As $\{\phi_n\}$ is a Wiener process, the variance of $\Delta\phi$ is calculated as $\sigma^2_{Schmidl} = 2\pi[(2N^2+1)/3N + CP]vT_s$, with v as the combined laser linewidth and T_s as the sample interval. We can easily prove that $\Delta\Phi_{Moose} = \Delta\phi_{Schmidl}$ and Moose estimator shares the same variance as Schmidl. In Schmidl (or Moose) estimator, the channel distortion affects the two signals y_{N+n} and y_n in the same way as long as the guard interval is longer than channel memory L. The estimation result of Schmidl (or Moose) estimator will be robust to linear channel distortion. However, the linear channel distortion for the cyclic prefix and data from which the cyclic prefix is generated are different. Thus, the CP estimator works accurately only for zero channel distortion case. Assuming distortion has been removed prior to estimation, CP estimator follows a similar derivation as Schmidl (Eq. 3.17, 3.18, 3.19) but comes with a different variance for phase difference $\Delta\phi_{CP}$:

$$\mathrm{Var}[\hat{\epsilon}_{CP}] = \frac{1}{(2\pi)^2}\Big[\sigma^2_{CP} + \frac{N_0}{(D \cdot CP)E_s}\Big] \tag{3.20}$$

$$\Delta\phi_{CP} = \frac{1}{D \cdot CP} \sum_{d=0}^{D-1} \sum_{n=0}^{CP-1} [\phi_{(N+CP)\cdot d+n+N} - \phi_{(N+CP)\cdot d+n}] \tag{3.21}$$

$$\sigma^2_{CP} = \frac{1}{D}\Big(\frac{1-CP^2}{3CP} + N + 2\Big) \tag{3.22}$$

Assuming the performance of CP and Schmidl (or Moose) estimators are identical for zero dispersion and zero phase noise case ($D = N/CP$), we expect CP to be performing better than Schmidl (or Moose) under nonzero linear phase noise case. This is because CP estimator has a smaller variance of phase noise difference between the two signals taken for cross-correlation.

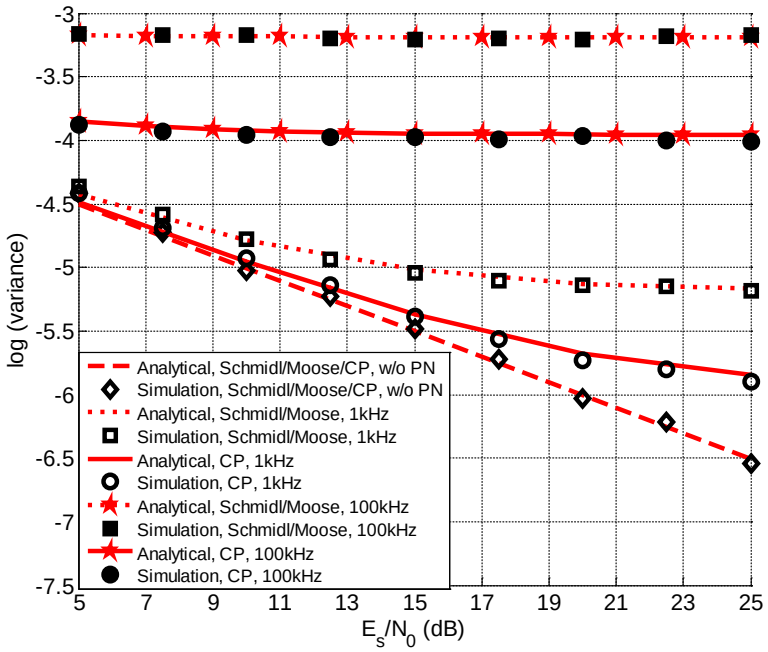

Figure 3.6: Analytical and simulation curves of estimation variance versus SNR for v=0,1,100 kHz, using Schmidl, Moose and CP estimator.

To verify the derived variance expressions, we built a CO-OFDM system using MATLAB. The system employs QPSK modulation with a DFT/IDFT size of 256 and a cyclic prefix of 32 samples. The signal is sampled at 10 Gsample/s. To match the performance of CP with Schmidl/Moose for the zero phase noise case, we set $D = N/CP = 8$.

Fig. 3.6, Fig. 3.7 and Fig. 3.8 show the simulation results in a back-to-back transmission. Fig. 3.6 shows the estimation accuracy in terms of vari-

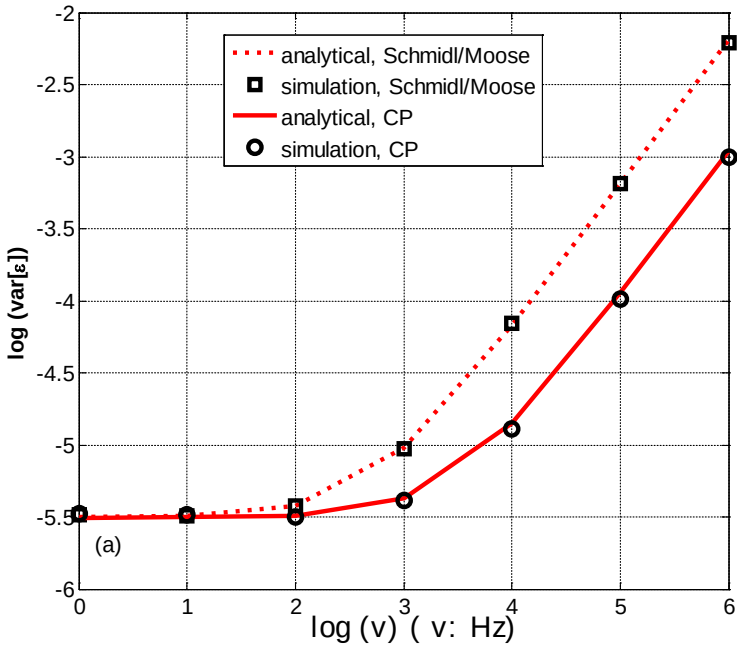

Figure 3.7: Analytical and simulation curves for estimation variance versus laser linewidth (v) at SNR=15 dB, using Schmidl, Moose and CP estimator.

ance ($\mathrm{Var}[\epsilon]$) versus signal-to-noise ratio (SNR, E_s/N_0) with different laser linewidths. All the simulation results (black symbol) agree well with the analytical curves (red line). At higher laser linewidth, say 100 kHz, the variance curves are no longer sensitive to SNR for all three methods, as $\sigma^2 >> N_0/(NE_s)$. CP estimator is more tolerant to linear phase noise than Schmidl (or Moose) estimator, e.g., it has nearly 10 times smaller variance than the other two methods at 100 kHz. Fig. 3.7 compares the laser linewidth tolerance of the three estimators at 15-dB SNR. In addition to the fact that no training symbol is required for CP estimator, it performs the best in the presence of linear phase noise. For any values of N, CP and D, CP has larger linear phase noise tolerance than Schmidl/Moose as long as we hold $D = N/CP$ and $CP \leq N$. Fig. 3.8 depicts the variance versus relative CFO ϵ for different methods and different laser

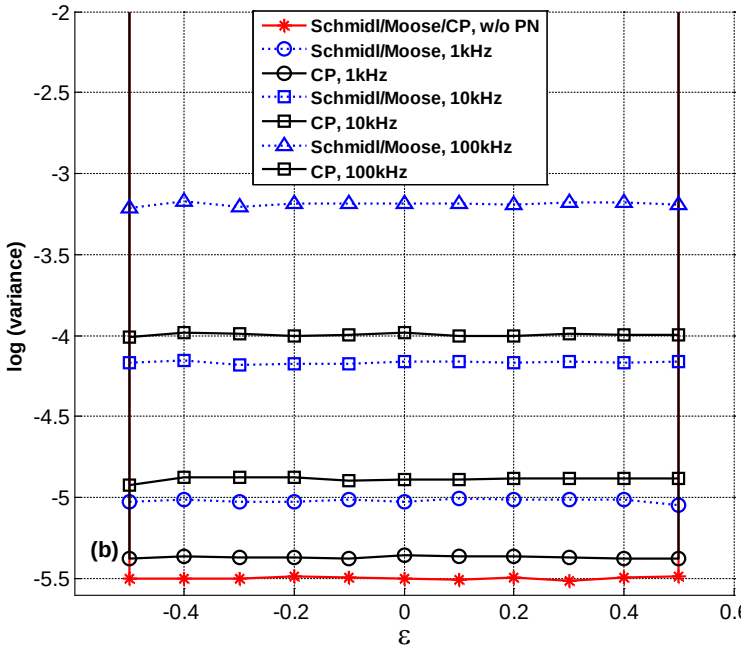

Figure 3.8: Estimation variance versus relative frequency offset for v=0, 1, 10, 100 kHz, using Schmidl, Moose and CP estimator.

linewidths . All the methods have the same estimation range and CP method has the most accurate estimation at nonzero laser linewidth.

In Fig. 3.9 and Fig. 3.10, we incorporate linear channel distortion (chromatic dispersion) with different dispersion values (0, 1700, 17000 ps/nm) into the system. As predicted, Schmidl (or Moose) estimator performs almost the same under different amount of dispersion. The small deviation from the ideal curve is due to the small nonzero components h_l for $l \geq CP$ generated by fiber chromatic dispersion. However, the degradation is almost negligible for as large as 17000-ps/nm dispersion (1000 km of standard single-mode fiber with 17-ps/nm/km dispersion parameter). To the contrary, the accuracy of the CP estimator is severely degraded by dispersion as small as 1700 ps/nm, especially for smaller linear phase noise case. The conclusions are expected to be the same for

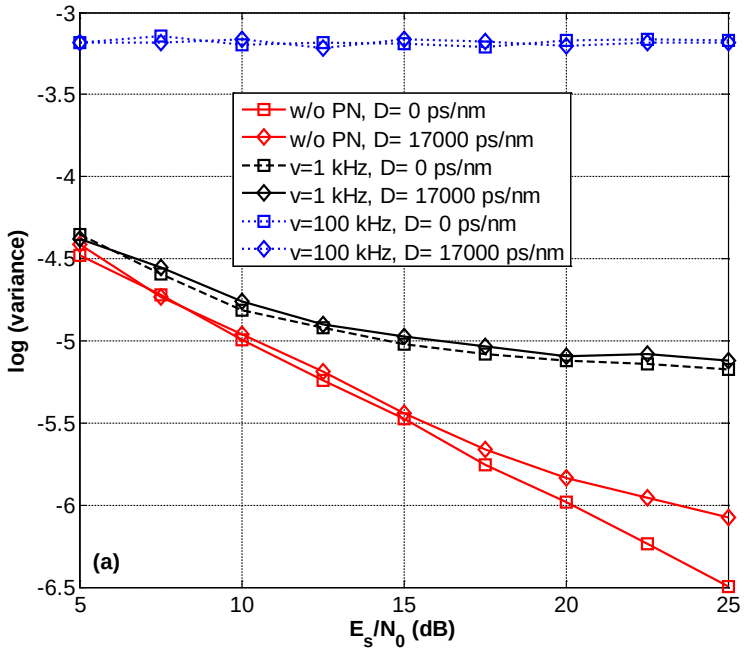

Figure 3.9: Simulation curves for estimation variance versus SNR under various dispersion values (0, 1700 ps/nm, 17000 ps/nm) using Schmidl/Moose.

polarization mode dispersion (PMD). We can transmit identical training symbols in different polarizations and thus PMD will affect the received signals in a similar way as CD in the single polarization case.

3.4 Performance Evaluation of Pilot-tone-assisted Estimator

The correct detection of ϵ_i depends on the correct detection of the peak (pilot-tone) in the received signal spectrum. Thus, the probability of correct detection (P_c) is calculated as the joint probability of the energy of pilot-tone being higher

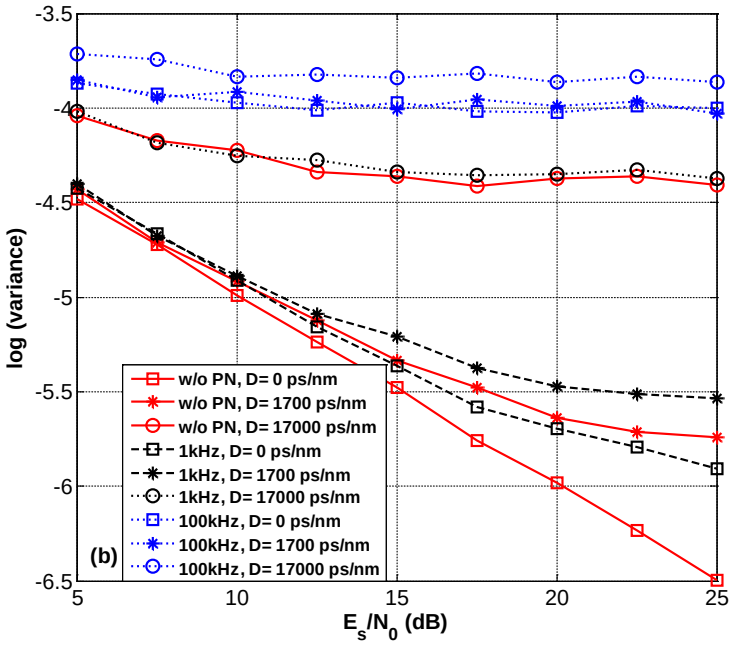

Figure 3.10: Simulation curves for estimation variance versus SNR under various dispersion values (0, 1700 ps/nm, 17000 ps/nm) using CP.

than any other subcarriers:

$$P_c = \prod_{k=1}^{N-1} P(|X_p + W_p|^2 > |X_k + W_k|^2) \tag{3.23}$$

where X_p is a real number representing the DC and X_k can be any point from the signal constellation. From Eq. 3.23, we can conclude that the error probability is only dependent on the pilot to average signal power ratio (E_p/E_s, $E_p = |X_p|^2$, $E_s = E[|X_s|^2]$), SNR (E_s/N_0) and DFT size (N). In Fig 3.11 we plot P_c versus pilot to average signal power ratio at different SNR in a back-to-back transmission with QPSK format. As predicted, the probability curve depends on SNR value and DFT size, but it is unaffected by f_0, ϵ_i or dispersion. For

constant amplitude modulation format, we can further reduce Eq. 3.23 to:

$$P_c = P^{N-1}(|X_p + W_p|^2 > |X_s + W_s|^2) \tag{3.24}$$

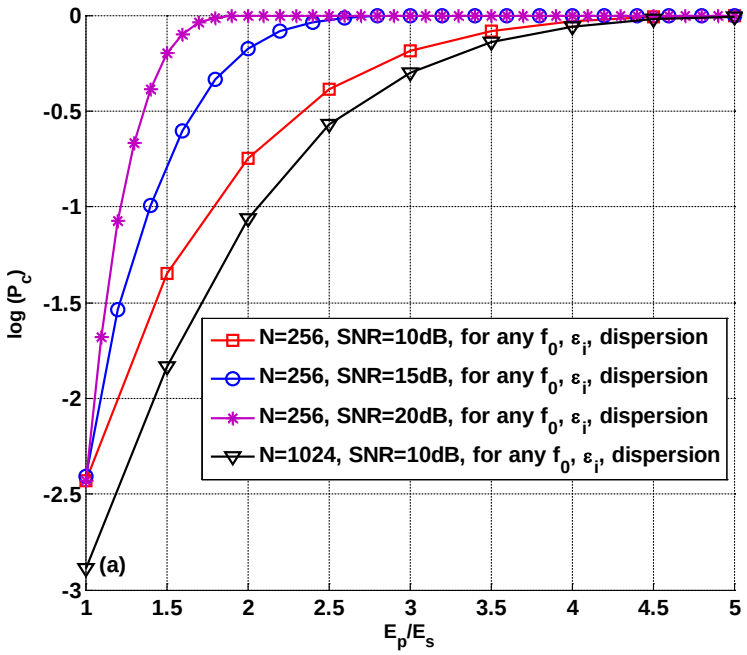

Figure 3.11: Probability of correct detection versus pilot to average signal power ratio for different DFT size, SNR, f_0, ϵ_i and dispersion.

As indicated by Eq. 3.24, a smaller SNR or larger DFT size requires higher pilot to average signal power ratio to achieve error free detection, which is verified by simulation. In Fig 3.12, P_c is ploted versus E_p/E_s for different laser linewidths, where degradation is hardly noticeable under 100 kHz. Larger laser linewidth (500 kHz, 1 MHz) affects the curves to a small extent but different curves still converge to 0 at almost the same speed. Linear phase noise affects the received signal through ICI, which will corrupt the peak in a similar way as AWGN noise.

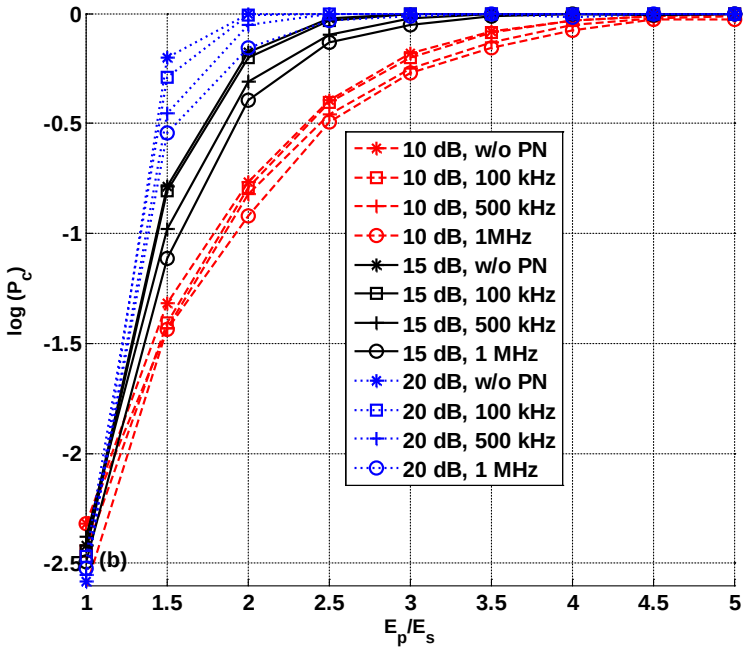

Figure 3.12: Probability of correct detection versus pilot to average signal power ratio for different SNR and linear phase noise.

3.5 Conclusion

In this chapter, we have proposed a novel FOC method by inserting one pilot-tone at the center of the OFDM spectrum, which can achieve the widest estimation range with only one training symbol. Our method is effectively demonstrated through experiment. Furthermore, we carried out a comprehensive analysis to examine the performance of our correlation-based and pilot-tone-assisted FOC method. We have analytically derived the fraction part estimation accuracy in the presence of linear phase noise for various correlation-based methods, Schmidl, Moose and CP, among which CP estimator is the most robust to linear phase noise. Schmidl and Moose estimators are shown to be robust to CD while CP estimator is quite sensitive to CD. The estimation accuracy of our pilot-tone-assisted integer part estimation method is proved to be independent of f_0, ϵ_i and

dispersion, dependent of DFT size, pilot to average signal power ratio, SNR and linear phase noise.

Chapter 4

Linear Phase Noise Compensation

One of the major challenges in coherent detection is to overcome the carrier phase noise when using a local oscillator (LO) to beat with the received signals to retrieve modulated information. The carrier phase noise can result from lasers. An optical phase-locked loop (PLL) is one solution to track the carrier phase with respect to the LO carrier in early days of coherent optical communication. However, an optical PLL operating at optical wavelengths in combination with distributed feedback lasers is quite difficult to implement [71]. With the availability of high-speed analog-to-digital converters (ADCs), the carrier phase estimation can be done in high-speed DSP units rather than using an optical PLL for carrier phase tracking, allowing for free-running LO laser [72]. Due to its longer symbol duration, OFDM is more sensitive to linear phase noise compared to a single carrier system. Moreover, as the OFDM symbol is modulated in the frequency domain, algorithms like M-th power cannot be applied in the time domain before FFT (fast Fourier transform). Uncompensated phase noise will cause common phase error (CPE) and intercarrier interference (ICI) to

the received signal after FFT. Thus, a compensation before FFT is preferred as it allows to remove intercarrier interference (ICI). Works in [70, 74, 75] insert an unmodulated RF-pilot tone in the middle of the OFDM band and a guard band around it, which provides the required reference for phase estimation and compensation. In this case, the power allocated to the pilot tone must be carefully selected with a tradeoff between phase estimation accuracy and energy wasted for pilot tone. However, if the linear phase noise varies within one OFDM symbol interval, residual phase noise exists and ICI still occurs as the RF-pilot is only able to monitor the average phase noise of one OFDM symbol. Alternatively, phase estimation can be done in the frequency domain after FFT block. In this case, compensation works include CPE compensation only [1, 73, 76, 77] or ICI compensation methods [80–86] with much higher computational complexity.

With perfect window and frequency synchronization, the received OFDM signal y_n in the time domain at sampling time instant nTs can be expressed as:

$$y_n = e^{j\phi_n} \sum_{l=0}^{L-1} h_l x_{n-l} + w_n \tag{4.1}$$

where x_n, y_n, h_n and w_n denote the transmitted signal, received signal, channel-impulse response and additive white Gaussian noise, respectively. The linear phase noise ϕ_n is a Wiener-Levy process described by:

$$\phi_{n+1} = \phi_n + \Delta\phi_n \tag{4.2}$$

where ϕ_n is the phase noise at sampling time instant nT_s and $\{\Delta\phi_n\}$ is a set of

independent and identically distributed, zero-mean Gaussian random variables, each with variance of $\sigma^2 = 2\pi v T_s$. v is the combined laser linewidth and T_s is the time difference between two samples. w_n is the additive white Gaussian noise from optical amplifiers. After removing cyclic prefix and taking the FFT, the resulting frequency domain signal is given by:

$$Y_{k,i} = I_{0,i} H_k X_{k,i} + \sum_{l=0, l\neq k}^{N-1} I_{k-l,i} H_l X_{l,i} + W_{k,i} \tag{4.3}$$

$$I_{m,i} = \frac{1}{N} \sum_{n=0}^{N-1} e^{j\phi_{n,i}} e^{-j2\pi mn/N} \tag{4.4}$$

where $X_{k,i}$, $Y_{k,i}$, H_k and $W_{k,i}$ are the frequency domain representations of x_n, y_n, h_n and w_n, respectively. The time subscript i in $H_{k,i}$ is dropped as the channel distortion could be considered constant throughout a certain OFDM frame (e.g., 30-50 symbols per frame). N is the FFT size. The term $I_{0,i}$ could be written as $|I_{0,i}|e^{j\Phi_i}$, with Φ_i defined as CPE for i-th symbol. The second additive term in Eq. 4.3 is defined as ICI. In this chapter, we will propose compensation methods to combat both CPE and ICI. In 4.1, we focus on CPE compensation. We first introduce the novel decision-aided carrier phase estimation algorithm. Based on that, we further propose new schemes which combine pilot-aided, decision-aided and decision-feedback methods. In 4.2, we propose a modified time-domain blind ICI mitigation method for non-constant amplitude modulation format, e.g., M-QAM.

4.1 Decision-aided CPE Estimation

In this section, we focus on CPE based estimation methods. There are mainly two groups of frequency-domain CPE estimation methods: pilot-aided (PA) method [1,73] and decision feedback (DF) method [76,77]. PA method makes use of pilot subcarriers (PSCs) to estimate the CPE. DF method, which is called decision-directed phase estimation (DDPE) in [76, 77] uses the initial decisions of the current symbol to re-estimate the phase noise, re-compensate and demodulate again, which involves two steps of estimation, compensation and demodulation. The decision-aided (DA) technique was initially proposed for carrier phase estimation in single carrier systems [78]. Here, we propose a novel decision-aided phase estimation method for CO-OFDM system. DA algorithm is also a CPE based method, which estimates the phase noise of the current symbol based on the decisions from the previous symbol. DF makes use of decision statistics of the current symbol whereas DA makes use of decision statistics of the previous symbol. By using the decisions from the previous symbol rather than the current symbol, DA incurs only one step of compensation and demodulation for each symbol, which exhibits a big difference from the DF method.

PA method takes up useful bandwidth whereas purely decision directed (DF or DA) methods are less tolerant to linear phase noise. Besides the DA method, we further propose two combined phase estimation schemes to combat these two problems: PA+DA and DA+DF. We compare the efficiency and effectiveness of PA, DA, DF methods and their combinations in a simulated 40-Gb/s single polarization CO-OFDM system with back to back transmission. The combination of DA and PA is shown to improve phase noise tolerance than DA while

reducing overhead compared to PA. The combination of DA and DF offers better tolerance to linear phase noise than DA and other purely decision-directed methods. Moreover, the performance of PA/DA/DA+PA in combination with DF converges to the same BER curve in the investigated situations. Thus, we only consider DA+DF because it has zero overhead. In section 4.1.2, we analytically evaluate the BER performance when only CPE is compensated for. BER expression under Gaussian approximation is derived, which is quite close to the simulation result, especially for smaller laser linewidth.

4.1.1 Principle

Inter-carrier interference (2nd term in Eq. 4.3) can be approximately considered as additive white Gaussian noise when a large number of subcarriers are used. Thus, the ICI term is lumped into the AWGN term $W_{k,i}$ and not dealt with here. Pilot symbols or preambles are inserted at the beginning of each OFDM frame to assist channel estimation and compensation:

$$\hat{H}_k = \sum_i \frac{Y_{k,i} X_{k,i}^*}{|X_{k,i}|^2} \tag{4.5}$$

$$\hat{Y}_{k,i} = \frac{Y_{k,i} \hat{H}_k^*}{|\hat{H}_k|^2} \tag{4.6}$$

After the channel distortion is removed, the model becomes:

$$\hat{Y}_{k,i} = e^{j\Phi_i} X_{k,i} + W'_{k,i} \tag{4.7}$$

where $W'_{k,i}$ includes both AWGN ($W_{k,i}$) and ICI. In the following derivations, we first focus on M-ary PSK OFDM system. Similar to the single carrier case

in [78], we introduce a complex phasor V^{DA} for M-ary PSK system based on the decision statistics of previous symbols as follows:

$$V_{k,i}^{DA} = \sum_{j=i-L}^{i-1} \hat{Y}_{k,j} D_{k,j}^{*} \tag{4.8}$$

where $D_{k,j}$ is the receiver's decision for symbol $X_{k,j}$, and L is defined as the memory length. Because the phase rotation is common for different subcarriers, we can get a more accurate phase reference by averaging across all the subcarriers. Due to the longer symbol duration in OFDM than in SC case, the optimum memory length L is found to be 1. The DA phasor for OFDM system is defined as:

$$V_{i}^{DA} = \frac{1}{N} \sum_{k=0}^{N-1} \hat{Y}_{k,i-1} D_{k,i-1}^{*} \tag{4.9}$$

Similar to the DA method, we define a new phasor V^{PA} based on the PSCs for the PA method:

$$V_{i}^{PA} = \frac{1}{N_p} \sum_{k=0}^{N_p-1} \hat{Y}_{k,i} X_{k,i}^{*} \tag{4.10}$$

To combine the DA and PA method, we define V^{DA+PA} as the weighted sum of V^{DA} and V^{PA}:

$$V_{i}^{DA+PA} = \gamma V_{i}^{DA} + (1-\gamma) V_{i}^{PA} \tag{4.11}$$

where γ is the weight factor defined over $(0, 1)$. Thus CPE is estimated from the

complex phasor as

$$\hat{\Phi}_i = \begin{cases} \angle V^{DA}, & \text{DA method} \\ \angle V^{PA}, & \text{PA method} \\ \angle V^{DA+PA}, & \text{DA+PA method} \end{cases} \tag{4.12}$$

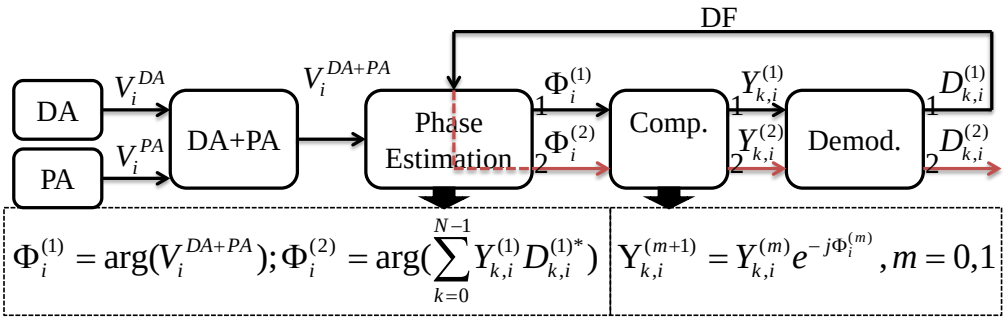

Figure 4.1: Phase estimation algorithm of DA+PA ($D_{k,i}^{(1)}$), DA+DF ($D_{k,i}^{(2)}$, $\gamma = 1$), PA+DF ($D_{k,i}^{(2)}$, $\gamma = 0$) and DA+PA+DF ($D_{k,i}^{(2)}$, $0 < \gamma < 1$) (Comp: compensation; Demod: demodulation)

A decision-feedback stage is added after DA, PA or DA+PA method with one extra step of residual phase noise estimation, compensation and demodulation. Fig. 4.1 shows the combined phase estimation scheme of DA, PA and DF.

Different from M-ary PSK system, the phasor is normalized by the energy of the decision for M-QAM system:

$$V_{k,i}^{DA} = \sum_{j=i-L}^{i-1} U_{k,i}^{-1} \hat{Y}_{k,j} D_{k,j}^{*} \tag{4.13}$$

$$U_{k,i} = \sum_{j=i-L}^{i-1} |D_{k,j}|^2 \tag{4.14}$$

By setting the memory length to 1 as well as averaging over all the subcarriers, we obtain the DA phasor for M-QAM system:

$$V_i^{DA} = \frac{1}{N} \sum_{k=0}^{N-1} |D_{k,i-1}|^{-2} \hat{Y}_{k,i-1} D_{k,i-1}^* \tag{4.15}$$

Similarly, PA phasor for M-QAM is formulated as:

$$V_i^{PA} = \frac{1}{N_p} \sum_{k=0}^{N_p-1} |X_{k,i}|^{-2} \hat{Y}_{k,i} X_{k,i}^* \tag{4.16}$$

For the complexity analysis, we only focus on complex multiplications and demodulations and ignore complex additions. The calculation of the DA phasor (Eq. 4.9) requires N complex multiplications per OFDM symbol whereas the calculation of the PA phasor requires N_p complex multiplications per OFDM symbol. The phase compensation stage requires N complex multiplications per OFDM symbol. Thus, the DA, PA and DA+PA methods require $2N$, $N_p + N$ and $N_p + 2N$ complex multiplications per OFDM symbol for phase estimation and compensation. Meanwhile, DA, PA and DA+PA methods require one-time demodulation only. The DF (DDPE) method in [76, 77] takes up $5N$ complex multiplications per symbol and two times of demodulation. The DA+DF method requires $4N$ complex multiplications and two times of demodulation, which is the second most computationally complex among all the methods. We sort the methods from most computationally intensive to least intensive as: DDPE $>$ DA+DF $>$ DA+PA $>$ DA $>$ PA.

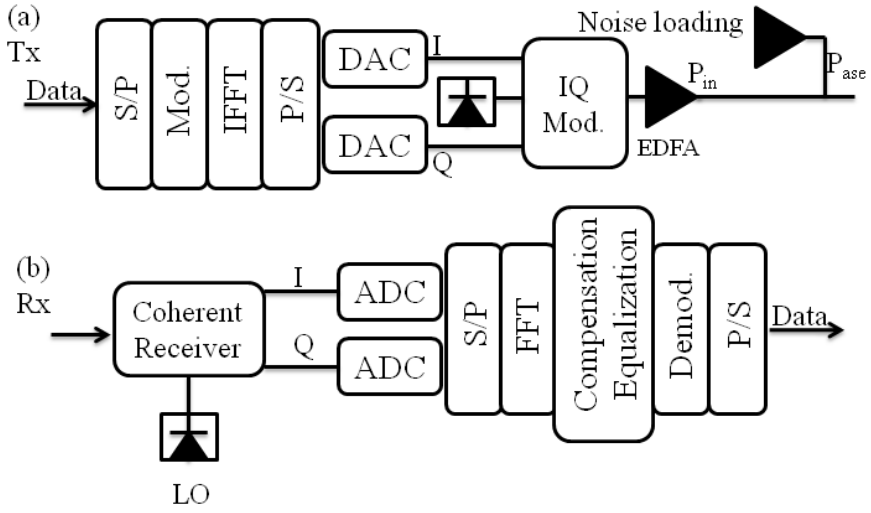

Figure 4.2: The schematic of CO-OFDM transmitter (a) and receiver (b) (Mod: modulation, Demod: demodulation, S/P: serial to parallel, P/S: parallel to serial, DAC: digital to analog converter, ADC: analog to digital converter)

4.1.2 Simulation Results

To investigate and compare the performance of DA, PA, DF and their combinations, we built a CO-OFDM system using VPI TransmissionMaker and MATLAB. The transmitter and receiver block diagram of our CO-OFDM is shown in Fig. 4.2. We only consider the linear phase noise case and back-to-back transmission. The original 40-Gb/s data are modulated onto 576 subcarriers with QPSK modulation and transferred to the time domain with a FFT/IFFT size of 1024. The other 448 subcarriers are zero padded for oversampling purpose and the filling ratio is 56%. A cyclic prefix of 128 samples is added to each symbol, resulting in an OFDM symbol size of 1152 samples. Decision-directed phase estimation (DDPE) [77] is included for comparison, which is a purely decision directed scheme. γ (for both DA+PA and DDPE) is optimized for each data

point by sweeping over all possible values from 0 to 1 with a step-size of 0.1.

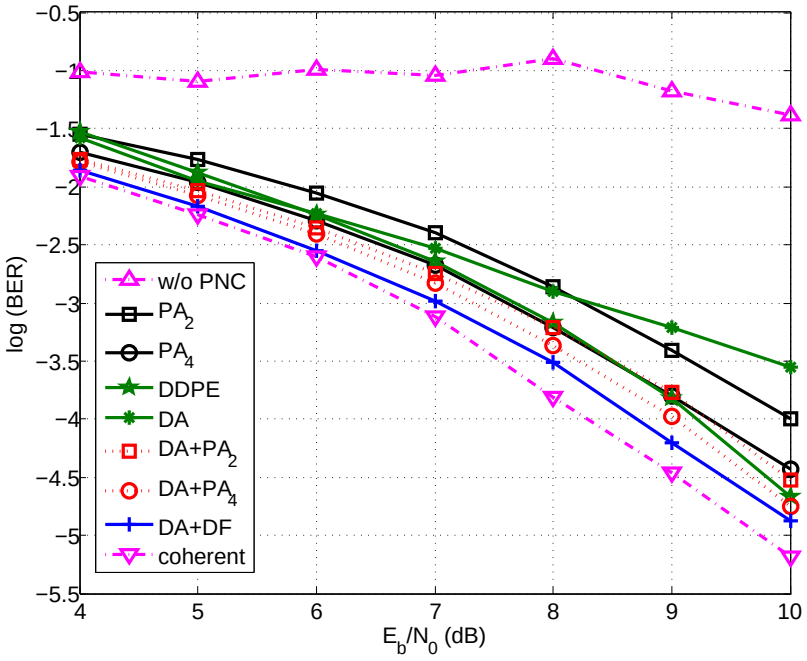

Figure 4.3: The BER curve of without phase noise compensation (w/o PNC), $\mathrm{PA}^{2/4}$, DDPE, DA, DA+$\mathrm{PA}^{2/4}$, DA+DF and coherent (no phase noise) for 80-kHz laser linewidth.

Fig. 4.3 shows the bit error rate (BER) performance versus the energy per bit to noise power spectral density ratio (E_b/N_0) for 80-kHz laser linewidth in the case of no compensation, $\mathrm{PA}^{2/4}$, DDPE, DA, DA+$\mathrm{PA}^{2/4}$ and DA+DF. PA^{n} means PA with n PSCs. In the figure, the coherent case (with no linear phase noise) is plotted as baseline for comparison, which always performs the best. DA+PA with 2 PSCs requires almost the same E_b/N_0 as PA with 4 PSCs to achieve a BER value of 10^{-3}, while the overhead is reduced by 50%. Moreover, the performance of PA/DA/DA+PA in combination with DF converges to the same BER curve, which is the best among all. Thus, we only consider DA+DF because it has zero overhead.

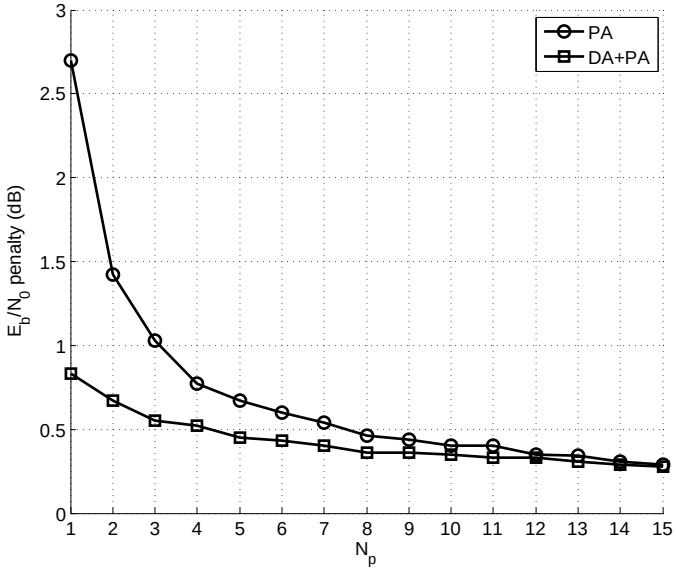

Figure 4.4: The E_b/N_0 penalty value versus N_p of PA and DA+PA method for 60-kHz laser linewidth.

To investigate the required number of pilot subcarriers N_p for both PA and DA+PA method, we plot the E_b/N_0 penalty (BER=10^{-3}) against N_p in Fig. 4.4 for 60-kHz laser linewidth. The E_b/N_0 penalty is calculated against the coherent case. DA+PA reduces the required E_b/N_0 significantly when the number of pilot subcarriers is small ($N_p < 4$). For example, DA+$\mathrm{PA}^{2/4}$ requires the same E_b/N_0 as $\mathrm{PA}^{5/7}$. Fig. 4.5 and Fig. 4.6 show the required E_b/N_0 (BER=10^{-3}) of $\mathrm{PA}^{2/4}$, DDPE, DA, DA+$\mathrm{PA}^{2/4}$ and DA+DF against laser linewidth (fixed FFT size=1024) or FFT size (fixed 80-kHz laser linewith), respectively. DDPE fails to achieve BER of 10^{-3} within 10-dB E_b/N_0 when the laser linewidth is beyond 120 kHz or the DFT size is beyond 1024 due to error propagation. Our proposed DA+DF performs best and is more tolerant to phase noise than DDPE with the same overhead and complexity. This is because the filtering window for phase noise in DA+DF is smaller than DDPE. DA+PA^2 requires about 1-dB

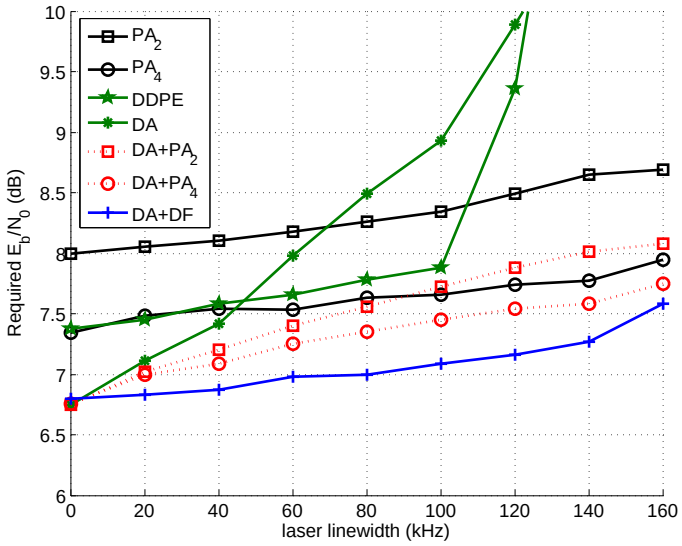

Figure 4.5: The required E_b/N_0 of $\mathrm{PA}^{2/4}$, DDEP, DA, DA+$\mathrm{PA}^{2/4}$ and DA+DF versus laser linewidth

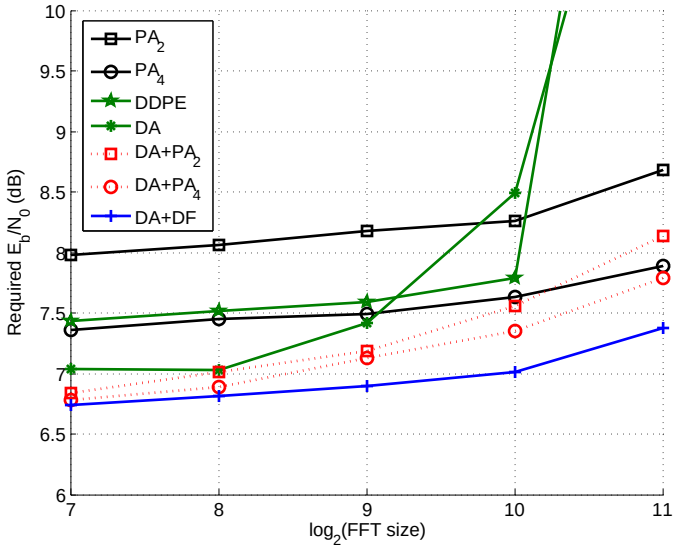

Figure 4.6: The required E_b/N_0 of $\mathrm{PA}^{2/4}$, DDPE, DA, DA+$\mathrm{PA}^{2/4}$ and DA+DF versus FFT/IFFT size.

less E_b/N_0 than PA^2 and requires almost the same E_b/N_0 as PA^4. The required E_b/N_0 of DA increases quickly as the laser linewidth or FFT size increases. This is because the phase variance between consecutive OFDM symbols ($\sigma^2 = 2\pi vt$) will increase with the increase of laser linewidth or FFT size. And the reliability of V^{DA}, which is calculated from the previous OFDM symbol, will decrease. Thus DA is performing better than $\mathrm{PA}^{2/4}$ and DDPE only with smaller laser linewith and FFT size.

Methods including PA, DA and DA+PA involve only one step of estimation, compensation and demodulation, while methods with DF stage involve two steps of those operations. In conclusion, we can either use DA+DF to reduce the overhead to zero with best performance, or use DA+PA to eliminate the additional demodulation step introduced by DF, with slightly worse performance.

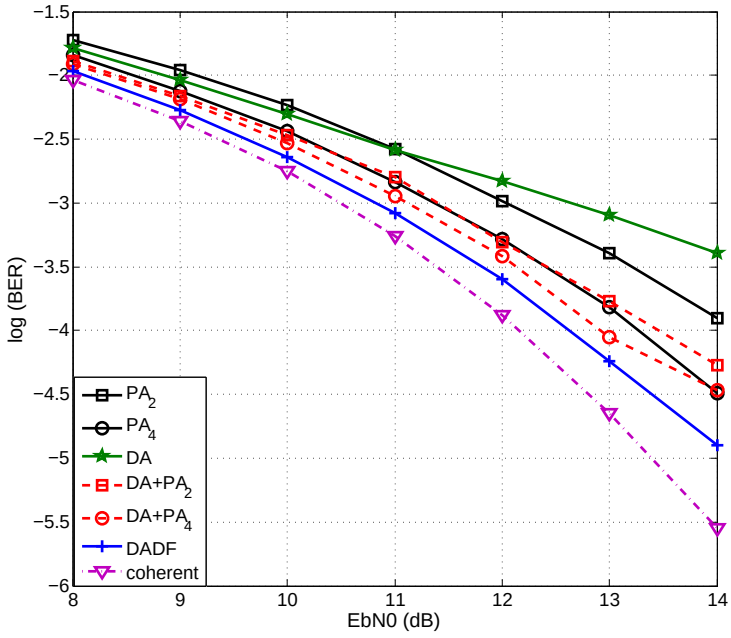

Figure 4.7: The BER curve of coherent(no phase noise), $\mathrm{PA}^{2/4}$, DDPE, DA, DA+$\mathrm{PA}^{2/4}$, DA+DF for 25-kHz laser linewidth, 100-Gb/s 16QAM system.

To demonstrate our methods in M-QAM system, we built a 16QAM CO-OFDM system at 100-Gb/s data rate. The rest parameters are the same with the QPSK system. In Fig. 4.7, we plot the BER performance for 25-kHz laser linewidth in case of $\mathrm{PA}^{2/4}$, DDPE, DA, DA+$\mathrm{PA}^{2/4}$ DA+DF. Similar conclusions could be reached for the 16-QAM case as for QPSK (Fig. 4.3).

4.1.3 BER Performance Evaluation

In this section, we will analytically derive the BER curves for the case in which only CPE is compensated for. Omitting the time subscript i and assuming the channel distortion is removed first, we rewrite the received signal model as follows:

$$Y_k = I_0 X_k + \sum_{\substack{l=0 \\ l\neq k}}^{N-1} I_{k-l} X_l + W_k \tag{4.17}$$

$$I_m = \frac{1}{N} \sum_{n=0}^{N-1} e^{j\phi_n} e^{-j2\pi mn/N} \tag{4.18}$$

The receiver compensates for CPE by rotating the signal over an angle $\Phi = \angle I_0$. This yields:

$$Y'_k = Y_k e^{-j\Phi} = |I_0| X_k + (\sum_{\substack{l=0 \\ l\neq k}}^{N-1} I_{k-l} X_l + W_k) e^{-j\Phi} \tag{4.19}$$

Since random variable I_m, X_k, X_j ($k \neq j$)are independent, we have that

$$\begin{aligned} E[|\sum_{\substack{l=0 \\ l\neq k}}^{N-1} I_{k-l}X_l|^2] &= E[(\sum_{\substack{l=0 \\ l\neq k}}^{N-1} I_{k-l}X_l)(\sum_{\substack{m=0 \\ m\neq k}}^{N-1} I^*_{k-m}X^*_m)] \\ &= \sum_{\substack{l=0 \\ l\neq k}}^{N-1} E[|I_{k-l}|^2|X_l|^2] + \sum_{\substack{l=0 \\ l\neq k, l\neq m}}^{N-1}\sum_{\substack{m=0 \\ m\neq k}}^{N-1} E[I_{k-l}I^*_{k-m}]E[X_lX^*_m] \\ &= \sum_{\substack{l=0 \\ l\neq k}}^{N-1} E[|I_{k-l}|^2|X_l|^2] \end{aligned} \tag{4.20}$$

The effective SNR is given by:

$$\text{SNR} = \frac{E_0E_s}{N_0+V_0} \tag{4.21}$$

$$E_0 = E[|I_0|^2] \tag{4.22}$$

$$V_0 = \sum_{\substack{l=0 \\ l\neq k}}^{N-1} E[|I_{k-l}|^2|X_l|^2] \tag{4.23}$$

According to [82], the cross correlation between I_n and I_p can be calculated as follows:

$$\begin{aligned} \mathbf{R}_I(n,p) &= E\{I_nI^*_p\} \\ &= \frac{1}{N^2}E\Big\{\sum_{k=0}^{N-1}\sum_{l=0}^{N-1} e^{j(\phi_k-\phi_l)}e^{-j\frac{2\pi}{N}(nk-pl)}\Big\} \\ &= \frac{1}{N^2}\sum_{k=0}^{N-1}\sum_{l=0}^{N-1} E\{e^{j\Delta\phi_{kl}}\}e^{-j\frac{2\pi}{N}(nk-pl)} \end{aligned} \tag{4.24}$$

where $\Delta\phi_{kl}$ denotes the cumulative linear phase noise increment between the l^{th} and k^{th} samples. With the linear phase noise being a Wiener process, $\Delta\phi_{kl}$ is a Gaussian random variable $\Delta\phi_{kl} \sim \mathcal{N}(0, |k-l|\sigma^2)$, where $\sigma^2 = 2\pi v T_s$. v

is the combined laser linewidth and T_s is the sample interval. The characteristic function of the random variable $\Delta\phi_{kl}$ is defined as $\Phi_{kl}(\omega) = E\{e^{j\omega\Delta\phi_{kl}}\}$. It follows that $E\{e^{j\Delta\phi_{kl}}\} = \Phi_{kl}(1) = e^{-\frac{|k-l|\sigma^2}{2}}$. Finally we obtain:

$$\begin{aligned}\mathbf{R}_I(n,p) &= \frac{1}{N^2}\sum_{k=0}^{N-1}\sum_{l=0}^{N-1} e^{-\frac{|k-l|\sigma^2}{2}} e^{-j\frac{2\pi}{N}(nk-pl)} \\ &= \frac{1}{N^2}\mathbf{F}(n,-p) \end{aligned} \tag{4.25}$$

where $\mathbf{F}(n,p)$ is the two-dimensional discrete Fourier transform of function $e^{-\frac{|k-l|\sigma^2}{2}}$. The ICI power can be easily calculated as

$$\begin{aligned} V_0 &= \sum_{\substack{l=0 \\ l\neq k}}^{N-1} E[|I_{k-l}|^2|X_l|^2] \\ &= \sum_{\substack{l=0 \\ l\neq k}}^{N-1} E[|I_{k-l}|^2]E[|X_l|^2] \\ &= E_s\sum_{v=1}^{N-1} E\{|I_v|^2\} \end{aligned} \tag{4.26}$$

which equals E_s multiplied by the sum of the diagonal elements (except the first element) of the correlation matrix $\mathbf{R}_I$. Under the central limit theorem, the ICI term will approximately follow Gaussian distribution with a large number of subcarriers. If we approximate the ICI noise distribution as Gaussian distribution, the approximate theoretical bit error rate of QPSK CO-OFDM system

under ideal CPE compensation will be:

$$BER = \frac{1}{2}\,\mathrm{erfc}(\sqrt{\frac{E_s}{2N_0}}) \tag{4.27}$$

$$\frac{E_s}{N_0} = \frac{E_s \mathbf{R}_I(0,0)}{N_0 + E_s \sum_{v=1}^{v=N-1} \mathbf{R}_I(v,v)} \tag{4.28}$$

In the following context, we will omit the word "approximate" before theoretical or analytical BER. Compared to the original $SNR = E_s/N_0$ in the absence of linear phase noise, we define the degradation in dB as:

$$\begin{aligned} D &= -10\log(\frac{\mathbf{R}_I(0,0)}{1+\frac{E_s}{N_0}\sum_{v=1}^{v=N-1}\mathbf{R}_I(v,v)}) \\ &= -10\log(\mathbf{R}_I(0,0)) + 10\log(1+\frac{E_s}{N_0}\sum_{v=1}^{v=N-1}\mathbf{R}_I(v,v)) \end{aligned} \tag{4.29}$$

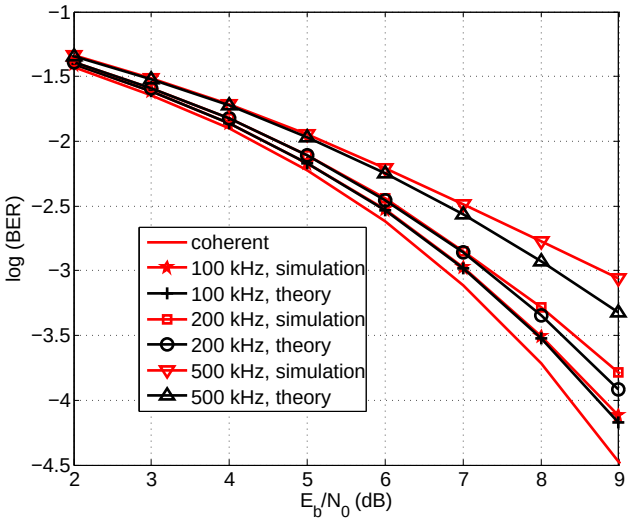

Figure 4.8: The analytical and simulation BER curve of a 40-Gsample/s QPSK CO-OFDM system (FFT size: 1024) under ideal CPE compensation with different laser linewidth.

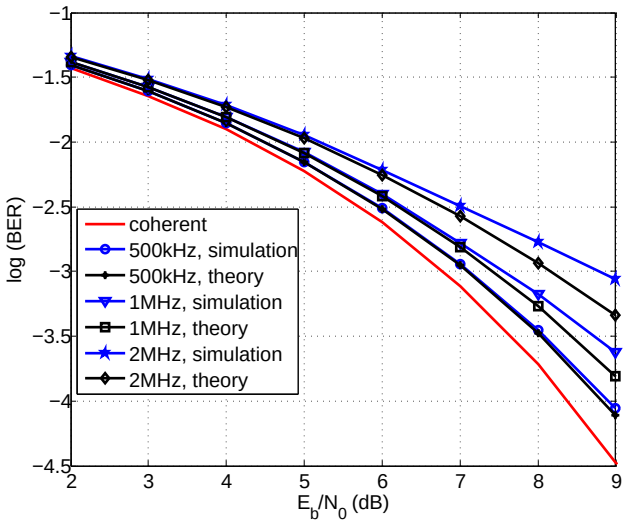

Figure 4.9: The analytical and simulation BER curve of a 40-Gsample/s QPSK CO-OFDM system (FFT size: 256) under ideal CPE compensation with different laser linewidth.

To verify our analytical BER and SNR penalty expression, we built a CO-OFDM simulation system with QPSK modulation format. The sample rate is 40 Gsample/s and the respective sample interval T_s is 0.025 ns. In all the simulations, the given laser linewidth value is single laser linewidth for both Tx and Rx laser and the combined laser linewidth would be double of the value given. The FFT size is set to 1024 for all the figures except Fig. 4.9, which employs an FFT size of 256.

In the first case, we investigate the analytical BER expression. In Fig. 4.8 and Fig. 4.9, we plot both analytical and simulation BER curves with different laser linewidth. At smaller laser linewidth (100 kHz, 200 kHz for Fig. 4.8 and 500 kHz for Fig. 4.9), the required SNR at BER equal to 10^{-3} is almost the same between simulation and theory using Gaussian approximation. An SNR difference of 0.8-dB (or 0.7-dB) between simulation and theoretical curves is

observed for 500-kHz (or 2-MHz) laser linewidth at 10^{-3} BER value in Fig. 4.8 (or Fig. 4.9). For both FFT size (1024 or 256), we can get accurate enough theoretical BER estimate using Eq. 4.27 for low enough laser linewidth (100 kHz or 500 kHz).

From Eq. 4.25 and Eq. 4.26, we know that the ICI power depends on both the FFT size (N) and phase noise variance ($\sigma^2 = 2\pi v T_s$). A comparison between Fig. 4.8 and Fig. 4.9 further reveals that the BER performance depends on the product of vNT_s. Thus, we could expect similar BER performance for different values of laser linewidth (v), FFT size (N) and sample rate ($R_s = 1/T_s$) as long as we keep the product of the three constant.

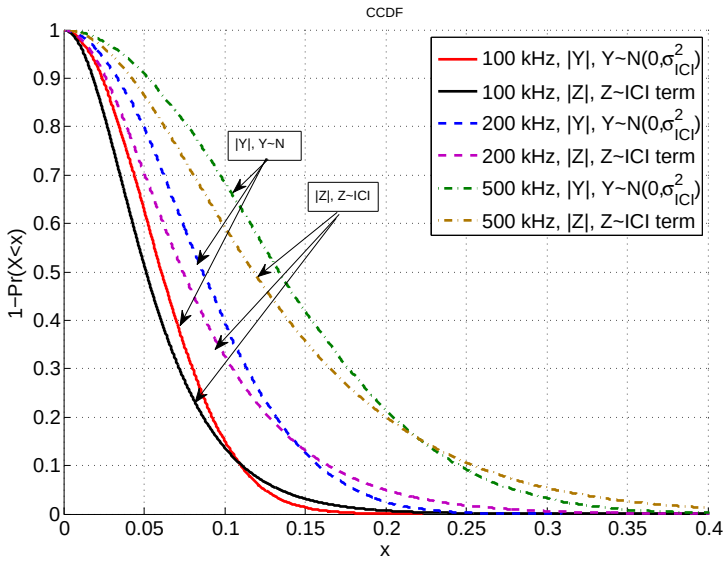

Figure 4.10: The CCDF of the ICI term amplitude.

Fig. 4.10 plots the complementary cumulative density function (CCDF) of the ICI term amplitude ($|Z|$) obtained by simulation in the presence of phase noise, where $Z = \sum_{l=0,l\neq k}^{N-1} I_{k-l} X_l$. The CCDF of the Gaussian variable amplitude ($|Y|$) is also plotted, with the variance equal to the ICI power calculated

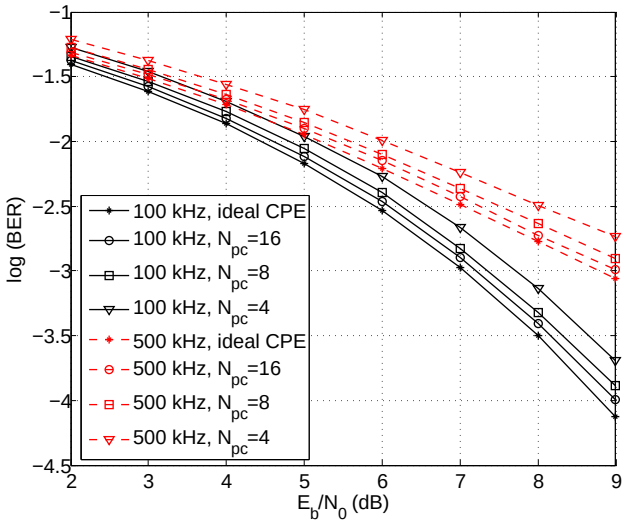

Figure 4.11: The simulation BER curve with ideal CPE compensation or PA CPE compensation with different number of pilot subcarriers

from Eq. 4.26. The actual ICI distribution has thinner head and broader tails compared to Gaussian distribution. The larger the linear phase noise values, the slower the CCDF curve approaches zero and the bigger difference exists between two CCDF curves. Moreover, the CCDF of $|Y|$ approaches zero slightly faster compared to the CCDF of $|Z|$. It is thus expected that the theoretical BER using Gaussian approximation would be slightly lower than the real BER, especially at larger phase noise variance. The more the ICI distribution deviates from the Gaussian distribution, the less accurate are the BER results obtained from Gaussian approximation. The conclusion is consistent with the result that the theoretical BER curves are an underestimate of the simulation ones and they deviate more from simulation curves at higher laser linewidth.

Fig. 4.11 plots the BER curves of PA method with different pilot subcarriers. With a large number of pilot subcarriers (e.g., 8, 16), the angular information of I_0 can be accurately estimated. Thus, the resulting BER curve is quite

close to the ideal CPE compensation case.

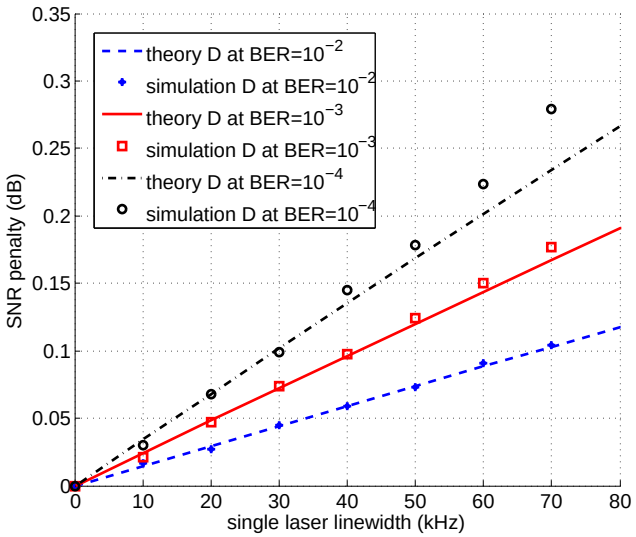

Figure 4.12: The analytical and simulation SNR penalty versus laser linewidth at different BER levels starting from the zero phase noise case.

In the second case, we investigate the analytical SNR degradation expression. Fig. 4.12 compares the SNR penalty at various BER levels due to ICI caused by LPN. For higher BER levels (10^{-2} and 10^{-3}) and smaller laser linewidth, the simulation result is perfectly consistent with the analysis given by Eq. 4.29. For lower BER or larger laser linewidth, the analytical curves become an underestimate for simulation results. This is because the marginal degradation given by Eq. 4.29 would be smaller than the exact SNR penalty as penalty becomes too large.

This analytical result provides us a lower limit of the BER (or SNR penalty) curve when only CPE is compensated for and ICI is ignored. Given the conventional parameters of a QPSK CO-OFDM system (FFT size, sample rate), we can easily estimate BER based on Eq. 4.27. With the help of Eq. 4.27, we can easily tell whether ICI compensation is necessary under certain BER requirement

of the system. The analytical result in Eq. 4.29 shows the approximate SNR penalty for achieving a certain BER value with a certain laser linewidth without the need of simulation.

4.2 Time-domain Blind ICI Compensation

The linear phase noise will generate two effects: rotation of all subcarriers of an OFDM symbol by a common angle defined as common phase error (CPE) and an additive term called inter-carrier interference (ICI). Lots of research on phase noise suppression assumes the ICI to be additive white Gaussian noise and takes care of CPE only [1, 74, 76]. However, the correction of the CPE does not always suffice, especially for larger laser linewidth and higher-order modulation format. Methods have been proposed to estimate the higher spectral components of phase noise thus reducing ICI in either wireless [80–82] or optical [83–86] domain. Works including [81–83] compensate for CPE using pilots and make hard decisions first. In [84], the authors proposed to replace the pilots in [83] with pseudo-pilots to achieve higher spectral efficiency. ICI is then estimated based on the initial decisions, which will suffer from falsely detected symbols. Paper [85] discards pilots and estimates both CPE and ICI in a decision-aided manner by running multiple iterations. Those decision-aided ICI (DA-ICI) compensation methods will suffer from decision errors, resulting in performance degradation. The matched filtering approach in [86] uses adaptive equalization based on an FIR filter which cancels the phase noise. However, it requires as many as $2N$ (N is the DFT size) iterations to converge and the calculation also involves decision statistics. A blind ICI (BL-ICI) compensation

scheme over constant amplitude modulation was proposed in [80] for wireless communication. The author partitioned one received OFDM symbol into sub blocks and used the approximate average phase noise over each sub block to cancel ICI.

In this section, we propose a new algorithm derived from [80] for CO-OFDM system over higher order non-constant amplitude modulation format, e.g., 16-QAM. To calculate the actual signal power in BL-ICI algorithm, we propose three schemes: (i) use the average power; (ii) use the approximate power; (iii) use the average power for 1st iteration and approximate power for 2nd iteration. We test our algorithm and compare it with the DA-ICI algorithm [81,82] through simulation over different formats: 8-QAM, 16-QAM, 32-QAM and 64-QAM. The 2-iterations-BL-ICI (2Iter-BL-ICI) mitigation method is demonstrated to be most effective amongst the three methods, followed by average-power-BL-ICI (Avg-BL-ICI) scheme. We have demonstrated that our Avg-BL-ICI algorithm is performing better than the DA-ICI method at large laser linewidth (e.g., 200 or 300-kHz for 16-QAM, 50 or 100 kHz for 64-QAM) in a simulated 56-Gb/s CO-OFDM system for both 16-QAM and 64-QAM after spans of fiber transmission. Moreover, Avg-BL-ICI shares the same order of complexity compared with DA-ICI [81, 82], yet does not suffer from symbol decision errors. As higher-order modulation formats like 16-QAM are quite sensitive to linear phase noise and decision errors, we employ pilot-aided CPE (PA-CPE) compensation instead of decision-aided methods after ICI mitigation.

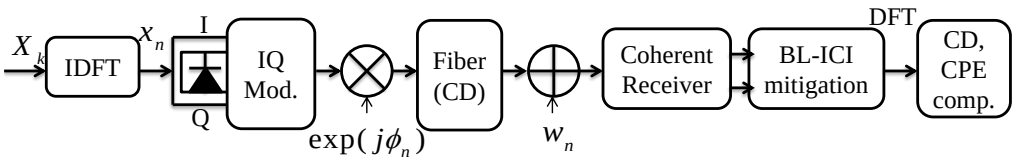

Figure 4.13: Simulation setup for CO-OFDM system. Mod.: modulator, CD: chromatic dispersion, comp.: compensation

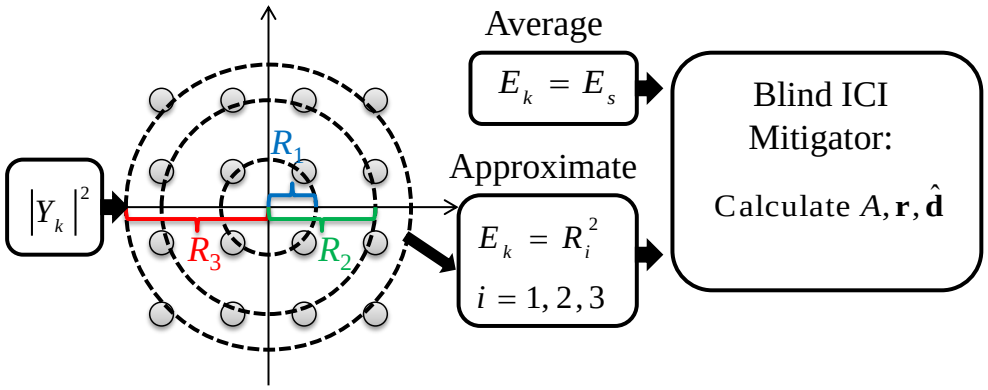

Figure 4.14: Blind ICI mitigation algorithm for non-constant amplitude modulation format using average signal power or approximate signal power

4.2.1 Principle

Fig. 4.13 shows the simulation model of our CO-OFDM system. We denote by $X_{k,i}$, the frequency-domain complex modulation symbol associated to the k-th subcarrier and i-th OFDM symbol, with $k = 0, \cdots, N-1$. The discrete time-domain samples are obtained by DFT transform:

$$x_{N*i+n} = \frac{1}{\sqrt{N}} \sum_{k=0}^{N-1} X_{k,i} e^{j2\pi kn/N} \tag{4.30}$$

The received signal y_n is distorted by linear phase noise ϕ_n, channel chromatic dispersion (CD) as well as additive white Gaussian noise (AWGN) w_n

from optical amplifiers:

$$y_n = e^{j\phi_n} \sum_{l=0}^{L-1} h_l x_{n-l} + w_n \tag{4.31}$$

where h_l is the channel impulse response accounting for CD and symbol index i is omitted for simplicity. We assume a finite impulse response of length L samples. Taking an N-point DFT on the received samples $y = [y_0, y_1, \cdots, y_{N-1}]^T$, we get the frequency-domain signal:

$$Y_k = \Psi_0 H_k X_k + \sum_{l=0, l\neq k}^{N-1} \Psi_{k-l} H_l X_l + W_k \tag{4.32}$$

$$\Psi_m = \frac{1}{N} \sum_{n=0}^{N-1} e^{j\phi_n} e^{-j2\pi mn/N} \tag{4.33}$$

where X_k, Y_k, H_k and W_k are the frequency domain transmitted symbol, received symbol, channel transfer function and AWGN, respectively. Ψ_0 is the CPE and the 2nd additive term in Eq. 4.32 is the ICI. Similar to [80], one received OFDM symbol is partitioned into N_B subblocks with equal length $S = N/N_B$ in the time-domain, and the time-average of the phase noise at each subblock is defined as $\bar{\phi}_q (0 \leq q \leq N_B - 1)$. In the high signal-to-noise ratio (SNR) region, a relation between the squared magnitude of the channel gain multiplied by the data symbol and the time averages $\bar{\phi}_q$ can be established as follows:

$$|H_k|^2 |X_k|^2 = \Big| \sum_{q=0}^{N_B-1} \exp(-j\bar{\phi}_q) \exp(-j\frac{2\pi qSk}{N} C_{k,q}) \Big|^2 \tag{4.34}$$

where $C_{k,q}$ is the N-point DFT of the received samples at the qth subblock with

zero padding. The method in [80] assigns a constant E_x to $|X_k|^2$. To extend the blind estimation method to non-constant amplitude modulation format, e.g., 16-QAM, we assign E_k with either the average signal power equal to E_s or approximate signal power equal to R_i^2 where $i = \text{argmin}_j \left||Y_k|^2 - R_j^2\right|$. As depicted in Fig. 4.14, each received symbol Y_k can be approximately located on one of the three rings from 16-QAM constellation, and its approximate power equals the squared ring radius. Exploiting the relationship in Eq. 4.34, the blind ICI mitigator then calculates the differences $d_q = \bar{\phi}_q - \bar{\phi}_0$ [80]:

$$\hat{\mathbf{d}} = [\hat{d}_1, \cdots, \hat{d}_{N_B-1}]^T = (A^T A)^{-1} A^T \mathbf{r} \tag{4.35}$$

$$\begin{aligned} r_k &= |H_k|^2 E_k - \sum_{q=0}^{N_B-1} |C_{k,q}|^2 \\ &- 2 \sum_{q_1=0}^{N_B-1} \sum_{q_2=q_1+1}^{N_B-1} |C_{k,q_1}||C_{k,q_2}| \cos(\theta_{k,q_1,q_2}) \end{aligned} \tag{4.36}$$

$$\begin{aligned} A_{m,n} &= 2 \sum_{q=n+2}^{N_B-1} |C_{m,n+1}||C_{m,q}| \sin(\theta_{m,n+1,q}) \\ &- 2 \sum_{q=0}^{n} |C_{m,n+1}||C_{m,q}| \sin(\theta_{m,q,n+1}) \end{aligned} \tag{4.37}$$

where $A_{m,n}$ is the (m,n)th entry of matrix A and $\theta_{k,q_1,q_2} = \angle C_{k,q_1} - \angle C_{k,q_2} + 2\pi(q_2 - q_1)Sk/N$. To further improve the performance, we could run two iterations of the algorithm (Eq. 4.35) using average power for the 1st iteration and approximate power for the 2nd iteration. After ICI compensation in the time domain, the pilot-aided (PA) method [1] is applied to remove the CPE in the frequency domain.

4.2.2 Simulation Results

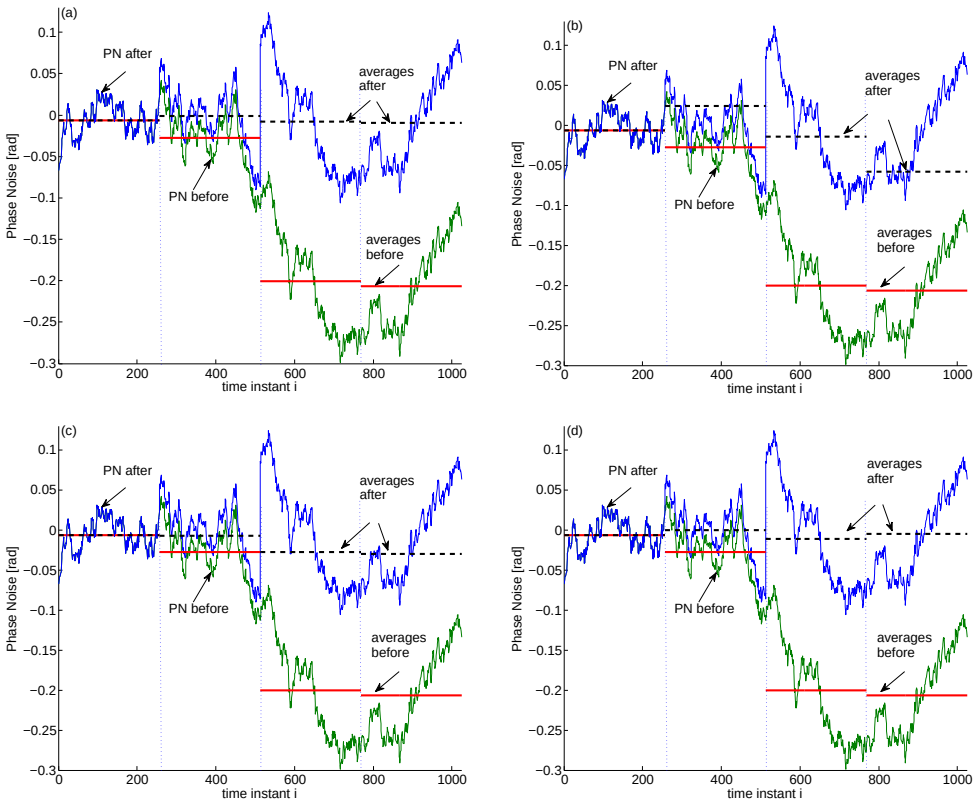

Figure 4.15: A phase noise realization and its time-averages over the subblocks before (phase noise: green solid, average: red solid) and after (phase noise: blue solid, average: black dashed) ICI compensation when $v = 100$ kHz for different knowledge of E_s: (a) perfect, (b) average, (c) approximate and (d) two iterations

To investigate the performance of our blind ICI mitigation algorithm, we built a 14 Gbaud 16-QAM CO-OFDM system using MATLAB. The original 56-Gb/s data is modulated onto 576 subcarriers with 16-QAM modulation and transferred to the time domain with a FFT/IFFT size of 1024. The other 448 subcarriers are zero padded for oversampling purpose and the filling ratio is 56%. A cyclic prefix of 128 samples is added to each symbol, resulting in an OFDM symbol size of 1152 samples. 5 pilot subcarriers are inserted for CPE compensation. A frequency-domain decision-aided ICI (DA-ICI) miti-

gation method [81, 82] is included for comparison. Compared to the method employed in [81, 82], the optical methods in [83–85] are based on the same frequency-domain model and follow quite similar procedure by calculating the ICI components up to a degree L using hard decisions. The principle and performance of [81–85] are almost the same. Thus, we only compare our time-domain BL-ICI mitigation algorithm with one implementation of the frequency-domain method for simplicity.

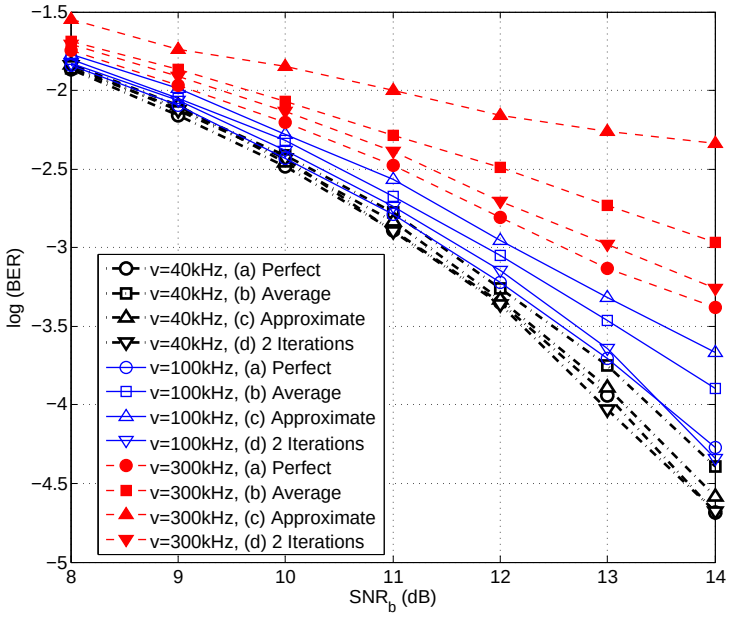

Figure 4.16: BER performance with different laser linewidths (40, 100, 300 kHz) and different knowledge of E_k for b2b transmission of 16-QAM-CO-OFDM

Fig. 4.15 shows the approximation on a realization of the phase noise for different knowledge of E_s: (a) perfect, (b) average, (c) approximate and (d) two iterations. The perfect knowledge case treated the transmitted symbol as known and is shown as an upper limit of performance. As depicted by the figure, both average and approximate cases can greatly remove ICI while the two iterations case is almost as good as the perfect case. This is further demonstrated in Fig.

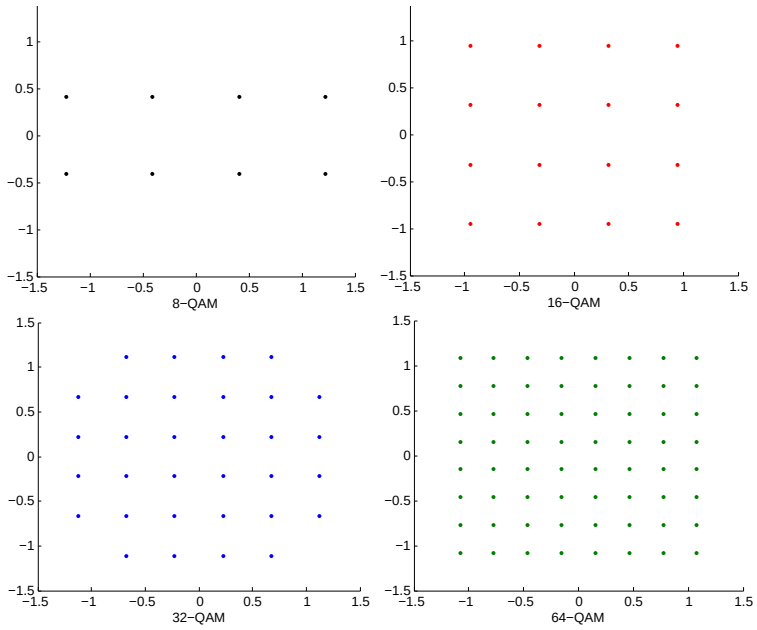

Figure 4.17: Constellation used in simulation for different M-QAM format.

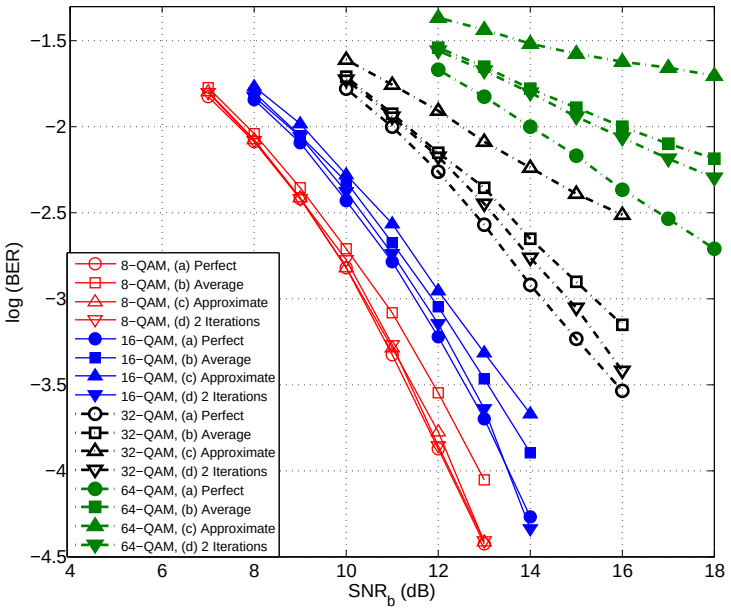

Figure 4.18: BER versus $\mathrm{SNR_b}$ with different knowledge of E_s at 100-kHz laser linewidth for different modulation formats: M-QAM ($M = 8, 16, 32, 64$).

4.16, where the bit error rate (BER) versus signal-to-noise ratio per bit ($\mathrm{SNR_b}$) curves are plotted in a back-to-back transmission with different laser linewidths v. For v=100/300 kHz, approximate result is worse than average result because lager linear phase noise will introduce larger ICI, which makes the approximate result less accurate. However, running two iterations will greatly improve the performance as approximate results are much closer to the actual power waveform at 2nd iteration. To demonstrate the applicability of our method to other modulation formats, we simulate the system for different M-QAM constellations (Fig. 4.17) with the same bit rate. We plot the BER versus $\mathrm{SNR_b}$ at 100-kHz laser linewidth using different knowledge of E_s for different M-QAM format in Fig. 4.18. It is observed that 2Iter-BL-ICI and Avg-BL-ICI achieve the best and second best performance among the three methods for higher-order modulation formats (16-QAM to 64-QAM). The performance degradation compared to the perfect case becomes larger for higher-order modulation formats. In Fig. 4.16 and Fig. 4.18, Avg-BL-ICI method achieves slightly worse yet still satisfactory performance compared to 2Iter-BL-ICI. Satisfactory performance has been achieved using average power while running only one iteration, thus we will use this setup for the following simulation.

Fig. 4.19(a) and (b) compare the performance of our Avg-BL-ICI mitigation algorithm against the DA-ICI algorithm for 16-QAM and 64-QAM, respectively. The transmission link was consisted of 5 or 2 spans of 80-km SSMF (attenuation: 0.2 dB/km, dispersion: 17 ps/nm/km, nonlinear coefficient: 1.3 $\mathrm{W^{-1}km^{-1}}$) and EDFA (noise figure=6 dB) without optical dispersion compensation for 16-QAM or 64-QAM respectively. Linear phase noise is added at both transmitter and receiver. The channel compensation is done in the fre-

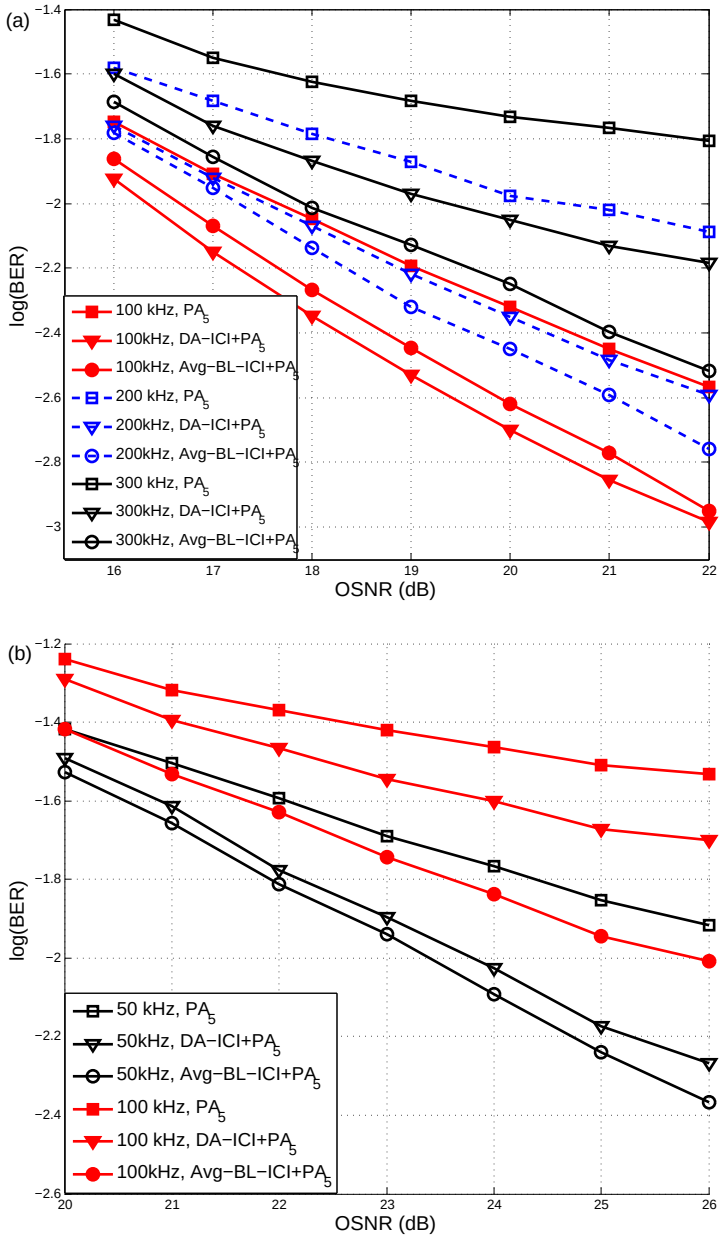

Figure 4.19: BER performance with different laser linewidths over 5 (or 2) spans transmission using PA_5 (5 pilot subcarriers) only, Avg-BL-ICI+PA_5 or DA-ICI+PA_5 for: (a)16-QAM and (b) 64-QAM.

quency domain similar to [1] after ICI mitigation. The parameters for both algorithms (N_B, u) are set such that DA-ICI and Avg-BL-ICI share the same order of complexity and further increasing N_B or u will not noticeably improve the performance under current circumstances. At 100-kHz laser linewidth, DA-ICI is performing slightly better than our time-domain Avg-BL-ICI algorithm for 16-QAM case. However, at larger (200-kHz or 300-kHz) laser linewidth, Avg-BL-ICI achieves better performance than DA-ICI for 16-QAM case. In the case of 64-QAM, our Avg-BL-ICI is consistently performing better than DA-ICI at 50-kHz or 100-kHz. From Fig. 4.19 we conclude that the time-domain Avg-BL-ICI method is performing better compared with frequency-domain DA-ICI at larger laser linewidth, especially for higher-order modulation format. This is because in DA-ICI, the estimation of higher spectral components will suffer from falsely detected symbols, especially for larger laser linewidth or higher-order modulation format.

Table 4.1: Computational complexity comparison between Avg-BL-ICI and DA-ICI

	Avg-BL-ICI	DA-ICI
N-point DFT	$N_B + 1$	1
Demodulation	1	2
Matrix Inversion	$(N_B - 1) \cdot (N_B - 1)$	$(2u + 1) \cdot (2u + 1)$

Table 4.1 lists the computational complexity comparison between Avg-BL-ICI and DA-ICI. As matrix inversion is the most complex operation (O(L^3)), we conclude that Avg-BL-ICI and DA-ICI share the same order of complexity with $N_B - 1 = 2u + 1$. Note that 2Iter-BL-ICI needs two times of operation for N-point DFT and matrix inversion as compared to Avg-BL-ICI.

4.3 Conclusion

In this chapter, we have proposed a novel decision-aided phase noise estimation algorithm. Based on that, we further propose to combine decision-aided algorithm with pilot-aided as well as decision-feedback methods. DA+PA is able to reduce the overhead of PA while improve the phase noise tolerance of DA. DA+DF is demonstrated to be performing the best among all the phase estimation schemes with zero overhead in a simulated 40-Gb/s CO-OFDM system.

A time-domain blind ICI mitigation algorithm was first proposed for constant amplitude modulation formats in wireless networks. Here, we propose new power estimation methods for this algorithm to adapt to non-constant amplitude modulation format in CO-OFDM system. The modified algorithm is demonstrated to be effective in mitigating ICI for a simulated 56-Gb/s CO-OFDM system over various non-constant amplitude modulation formats: 8-QAM, 16-QAM, 32-QAM and 64-QAM. Furthermore, it shows superior performance with the same complexity compared to the decision-aided ICI compensation algorithm at larger laser linewidths, especially for higher-order modulation format.

Chapter 5

Decision-aided IQ mismatch Compensation

OFDM is sensitive to non-idealities in the transmitter and receiver front-ends. IQ imbalance is one of the key front-end effects caused by the mismatch in amplitude and phase between I and Q branches. IQ imbalance will cause inter-carrier interference and thus degrade the performance of CO-OFDM system. Fig. 5.1 shows a generic block diagram with both transmitter and receiver IQ mismatch of a CO-OFDM transceiver. The IQ phase and amplitude imbalance can be modeled by parameters θ_t, η_t for Tx and θ_r, η_r for Rx, respectively. Without loss of generality, we can assume $0 \leq \theta_{t/r} < \pi/2$ and $0 < \eta_{t/r} \leq 1$ due to the symmetry of I and Q. In the ideal case, $\theta_{t/r}$ is equal to 0° and $\eta_{t/r}$ is equal to 1.

In the case of Tx IQ mismatch, the optically up-converted signal by non-

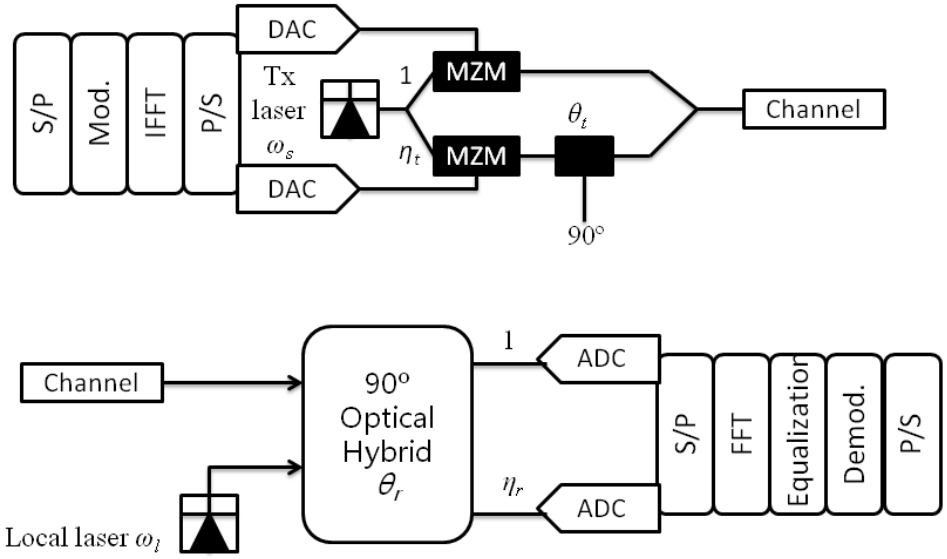

Figure 5.1: Block diagram of CO-OFDM transceiver with Tx and Rx IQ mismatch. S/P: serial to parallel, P/S: parallel to serial, Mod: modulation, Demod: demodulation, DAC: digital to analog converter, ADC: analog to digital converter, MZM: Mach-Zehnder modulator.

ideal optical IQ modulator can be modeled as [91]:

$$\begin{aligned} \hat{x}_{Tx,iq}(t) &= \Big[G_1 x(t) + G_2^* x^*(t)\Big] e^{j(\omega_s t + \phi_s(t))} \\ &+ \Big[G_1^* x^*(t) + G_2 x(t)\Big] e^{-j(\omega_s t + \phi_s(t))} \qquad (5.1) \\ G_1 &= (1 + \eta_t e^{j\theta_t})/2, G_2 = (1 - \eta_t e^{-j\theta_t})/2 \qquad (5.2) \end{aligned}$$

where $x(t)$, $\phi_s(t)$ and ω_s represent electrical OFDM signal, linear phase noise and laser frequency of Tx and $(\cdot)^*$ denotes the conjugation operation. After mixing the incoming signal with the 90° optical hybrid, the down-converted signal at the Rx can be expressed as [3]:

$$\hat{y}_{Tx,iq}(t) = \Big[G_1 x(t) + G_2^* x^*(t)\Big] e^{j(\omega_o t + \phi(t))} \qquad (5.3)$$

where ω_o is the frequency offset between Tx and local oscillator laser ($\omega_o = \omega_s - \omega_l$) while $\phi(t)$ is the combined linear phase noise of Tx and LO laser ($\phi(t) = \phi_s(t) - \phi_l(t)$). $\phi(t)$ can be modeled as a Wiener process with variance $2\pi v\Delta t$, with v being the combined laser linewidth and Δt being the time difference between two phase realizations.

In the case of Rx IQ mismatch,the signal after the ideal IQ modulator (i.e., $G_1 = 1, G_2 = 0$) can be written as:

$$\hat{x}(t) = x(t)e^{j(\omega_s t+\phi_s(t))} + x^*(t)e^{-j(\omega_s t+\phi_s(t))} \tag{5.4}$$

After down-conversion with the non-ideal 90° optical hybrid, the received signal can be expressed as [3]:

$$\hat{y}_{Rx,iq}(t) = K_1 x(t)e^{j(\omega_o t+\phi(t))} + K_2^* x^*(t)e^{-j(\omega_o t+\phi(t))} \tag{5.5}$$

$$K_1 = (1 + \eta_r e^{j\theta_r})/2, K_2 = (1 - \eta_r e^{-j\theta_r})/2 \tag{5.6}$$

As indicated by Eq. 5.3, frequency offset induces circularly rotating phase shift ($e^{j\omega_o t}$) to each sample, which has to be removed before Tx IQ mismatch compensation. However, if the frequency offset is removed prior to Rx IQ mismatch compensation, the signal will be corrupted by a term $K_2^* x^*(t)e^{-j(2\omega_o t)}$ as in Eq 5.5. Thus, the correct order of compensation is: (1)Rx IQ mismatch compensation, (2)frequency offset compensation, and (3)joint Tx IQ mismatch and channel distortion compensation.

As IQ imbalance destroys the orthogonality between the two received branches, Gram-Schmidt orthogonalization procedure (GSOP) was first proposed to com-

pensate for the IQ imbalance in CO-OFDM system [2, 3]. GSOP is a time-domain method which transforms a set of nonorthogonal samples into a set of orthogonal samples. GSOP operating before FFT could effectively remove the Rx IQ mismatch at the Rx side. In [3], GSOP is applied again after FFT to remove Tx IQ mismatch. However, it was not effective in compensating for Tx IQ imbalance in the presence of channel distortion. This is because the correlation between I and Q of the received signal is not only induced by Tx IQ imbalance, but also caused by channel distortion (CD/PMD). Thus a joint compensation of channel distortion and Tx IQ mismatch is necessary for this case. Recently, a pilot-assisted (PA) compensation method was proposed with a specially-structured pilot [36], which effectively compensates for Tx IQ mismatch in the presence of channel distortion.

Since Rx IQ mismatch can be first removed by GSOP before FFT, we only focus on the compensation of Tx IQ mismatch method in this chapter. The reminder of the chapter is organized as follows. In section 5.1, we propose a decision-aided joint compensation (DAJC) scheme for both Tx IQ mismatch and channel distortion, which shows superior performance compared to other methods. In section 5.2, we test our DAJC method in the presence of linear phase noise. We propose to employ another stage for phase noise compensation after DAJC. The scheme is demonstrated to be effective through simulation. In 5.3, we compare pre-distortion and post-equalization schemes for compensating IQ mismatch in coherent Optical OFDM system. It is shown that pre-distortion scheme has much larger tolerance to both phase and amplitude mismatch compared to post-equalization.

5.1 Decision-aided Joint Compensation of Channel Distortion and Tx IQ Mismatch

In this section, we propose a decision-aided joint compensation method for both channel distortion and Tx IQ imbalance. The channel transfer function and IQ imbalance factor are estimated jointly based on two pilot symbols, and updated after each decision-making stage. Our method is superior to the previous methods in several aspects. Firstly, DAJC makes use of standard pilot symbols, which simplifies the design compared to the special pilot structure proposed in [36]. Secondly, the adaptive characteristic of DAJC makes it more robust to time-variant channel and imbalance parameters, and also reduces the requirement on overhead. Last but not least, DAJC performs better than both GSOP and PA, with tolerable and adjustable increase in complexity. As shown in the simulation later, we can adjust the complexity of DAJC by applying the decision-aided stage every D symbols.

5.1.1 Principle

In the presence of Tx IQ mismatch, the distorted signal in the time domain would be:

$$\hat{x}(t) = G_1 x(t) + G_2^* x^*(t) \tag{5.7}$$

$$G_1 = (1 + \eta_t e^{j\theta_t})/2, G_2 = (1 - \eta_t e^{-j\theta_t})/2 \tag{5.8}$$

where $x(t)$ represents the electrical OFDM signal and $(\cdot)^*$ denotes the conjugation operation. Under Tx IQ mismatch and channel distortion, the received

frequency domain signal can be modeled as follows [36]:

$$Y_{k,i} = H_k(X_{k,i} + G\bar{X}^*_{k,i}) + W_{k,i} \quad (5.9)$$

$$G = \frac{G_2^*}{G_1} = \frac{1-\eta e^{j\theta}}{1+\eta e^{j\theta}} \quad (5.10)$$

$$\bar{X}^*_{k,i} = X^*_{k',i}, k' = \mathrm{mod}((N-k), N) \quad (5.11)$$

where the transmitted signal $X_{k,i}$ is distorted by channel distortion H_k and optical noise from optical amplifiers $W_{k,i}$. Subscripts i and k stand for the ith symbol and kth subcarrier, $\mathrm{mod}(x, y)$ gives the remainder of division of x by y and N is the total number of subcarriers. Each subcarrier experiences interference from its mirror-image position subcarrier proportional to G. This model incorporates both the channel distortion and the Tx IQ imbalance effects. There are $N + 1$ unknowns in Eq. 5.9, so at least 2 pilot symbols are required for calculation of all parameters. Two pilot symbols ($X_{k,1}$,$Y_{k,1}$) and ($X_{k,2}$,$Y_{k,2}$) are inserted at the beginning of the OFDM frame to provide the initial estimation. Ignoring the noise term $W_{k,i}$, we can calculate G and H as follows:

$$G = \frac{1}{N}\sum_{k=0}^{N-1} \frac{Y_{k,2}X_{k,1} - Y_{k,1}X_{k,2}}{Y_{k,1}\bar{X}^*_{k,2} - Y_{k,2}\bar{X}^*_{k,1}} \quad (5.12)$$

$$H_k = \frac{Y_{k,1/2}}{X_{k,1/2} + G\bar{X}^*_{k,1/2}} \quad (5.13)$$

To deal with frequency-dependent mismatch, we can modify Eq. 5.12 by adding frequency subscript k to G and removing or restricting the averaging window for G. To further improve the estimation accuracy as well as track the time-variant changes in the parameters, we employ a decision-aided method. Using the decision statistics ($D_{k,i}$ and $D_{k,i-1}$) obtained from the two previous

symbols, we can predict a new estimate for G and H_k:

$$\hat{G} = \frac{1}{N}\sum_{k=0}^{N-1}\frac{Y_{k,2}D_{k,1} - Y_{k,1}D_{k,2}}{Y_{k,1}\bar{D}^*_{k,2} - Y_{k,2}\bar{D}^*_{k,1}} \tag{5.14}$$

$$\hat{H}_k = \frac{Y_{k,1/2}}{D_{k,1/2} + G\bar{D}^*_{k,1/2}} \tag{5.15}$$

The IQ mismatch and channel distortion parameters used to compensate for the next received symbol $Y_{k,i+1}$ becomes a weighted sum of the previous parameters and the current estimation:

$$G^{\text{new}} = \gamma_g\hat{G} + (1-\gamma_g)G^{\text{old}} \tag{5.16}$$

$$H_k^{\text{new}} = \gamma_h\hat{H}_k + (1-\gamma_h)H_k^{\text{old}} \tag{5.17}$$

Zero-forcing (ZF) [36] compensation is then imposed to compensate for IQ mismatch and channel distortion:

$$\tilde{X}_k = f_{\text{ZF}}(k)Y_k + g_{\text{ZF}}(k)\bar{Y}^*_k \tag{5.18}$$

$$f_{\text{ZF}}(k) = \frac{1}{H_k(1-|G|^2)} \tag{5.19}$$

$$g_{\text{ZF}}(k) = \frac{-G}{\bar{H}^*_k(1-|G|^2)} \tag{5.20}$$

5.1.2 Simulation Results

To investigate the performance of our DAJC method, we built a CO-OFDM system at 20 Gb/s. The OFDM data was generated and processed by MATLAB, and the IQ modulation and demodulation as well as the channel transmission were done by VPI TransmissionMaker. The OFDM signal was modulated using

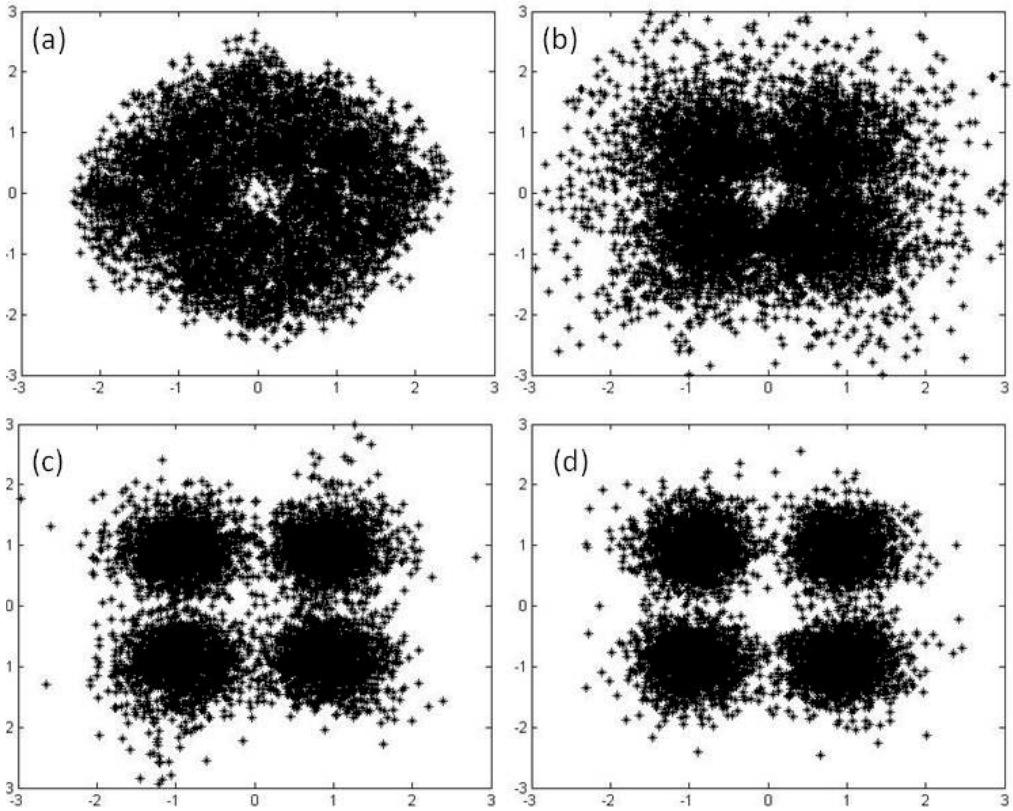

Figure 5.2: Received constellation after 800-km transmission with 50° phase and 2-dB amplitude imbalance for: (a) w/o compensation; (b) GSOP; (c) PA; (d) DAJC.

4QAM and consisted of 128 data carriers. The DFT/IDFT window size is 256 with a cyclic prefix of 32 samples. Every OFDM frame contains 2 pilot symbols, followed by 100 data symbols. To exclude the effect of phase noise, we set the linewidths of Tx laser and the local oscillator to zero. The performance was evaluated in transmission over 10 spans of 80-km standard single-mode fiber (SSMF) and erbium-doped fiber amplifier (EDFA, noise figure=6 dB) without optical dispersion compensation. GSOP [2] and PA [36] were implemented for performance comparison. For equality, the number of training symbols per frame was set to 2 in all cases. Amplitude imbalance was measured in terms of dB, where $\eta = 0.5$ corresponds to 3 dB. Fig. 5.2 shows the received constella-

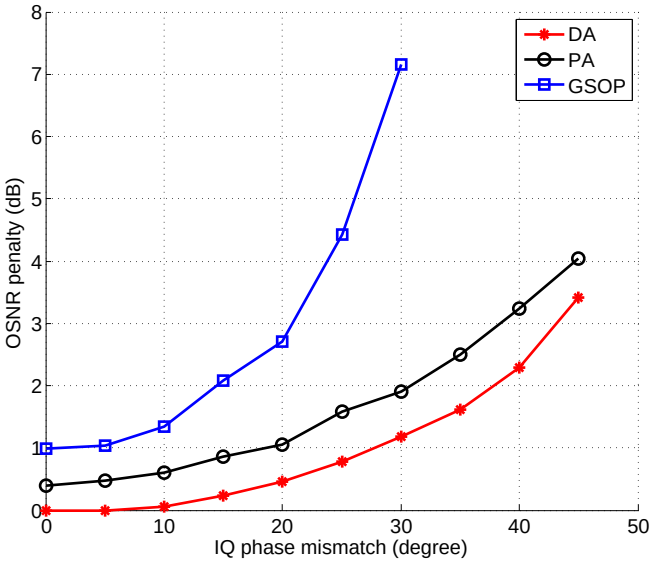

Figure 5.3: OSNR penalty versus IQ phase imbalance after 800-km transmission with three different methods: GSOP, PA and DAJC.

tion maps with 50° phase and 2-dB amplitude mismatch for four cases: without any compensation, with GSOP, with PA and with DAJC methods. In the presence of channel distortion and Tx IQ imbalance, GSOP almost fails and DAJC achieves the best performance among all.

Fig. 5.3 shows the optical signal-to-noise ratio (OSNR) penalty for a target BER of 10^{-3} versus Tx IQ phase imbalance over 800-km transmission in the case of equalization with GSOP, PA and DAJC. Fig. 5.4 compares the OSNR penalty versus Tx IQ amplitude imbalance under the same case for the three methods. The OSNR penalty was calculated against the best performance case using GSOP method with no IQ mismatch. As can be seen from Fig. 5.3 and Fig. 5.4, our DAJC method has about 0.5-dB improvement over the PA method in the presence of either phase or amplitude imbalance. This is because our DAJC adaptively updates the channel transfer function and IQ imbalance factor,

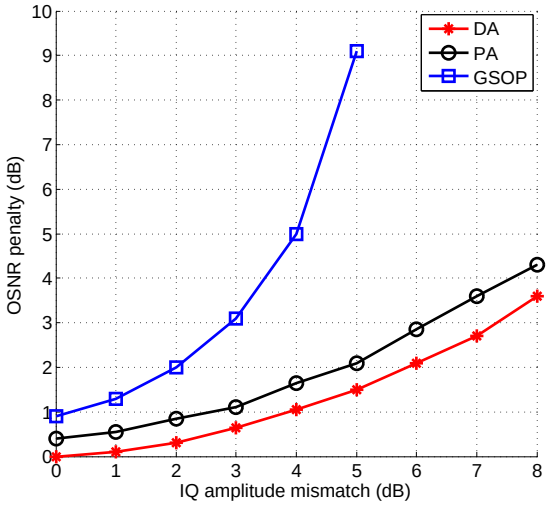

Figure 5.4: OSNR penalty versus IQ amplitude imbalance after 800-km transmission with three different methods: GSOP, PA and DAJC.

which provides a more accurate estimation.

To further investigate the performance of the proposed DAJC method, we reduce the overhead from 2% to 0.25% by increasing the data per frame from 100 symbols to 800 symbols. Fig. 5.5 shows the BER curve for PA method and DAJC method when the number of OFDM data symbols per frame is 100 and 800, respectively. The phase imbalance is 50° while the amplitude imbalance is 2 dB. Our DAJC method has considerably better BER performance than the PA method. Besides, PA method achieves almost the same performance for 100 and 800 symbols per frame while our DAJC method has even lower BER with longer frame size. The BER performance depends on the estimation accuracy of the IQ mismatch and channel distortion parameters if the parameters stay unchanged within the OFDM frame, which is the case in our simulation. For PA method, the estimation is only conducted once at the beginning, whose accuracy is independent of frame size. For decision-aided method, it becomes more sta-

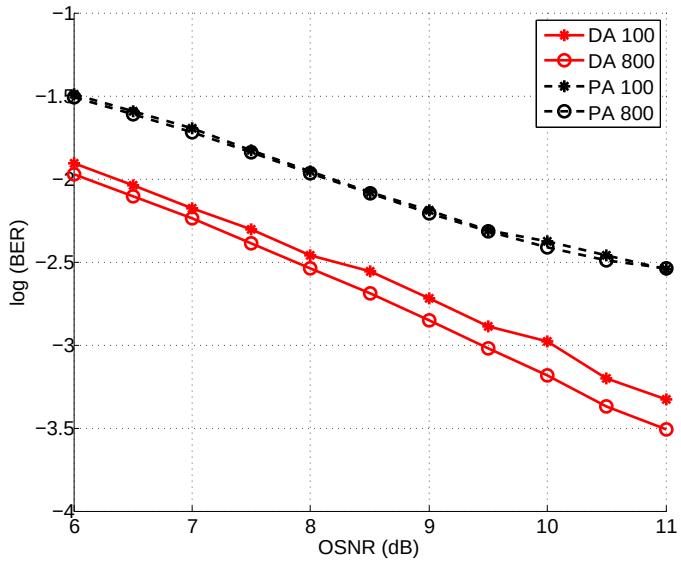

Figure 5.5: OSNR sensitivities for different frame sizes (100 or 800) after 800km transmission with 50° phase and 2-dB amplitude imbalance.

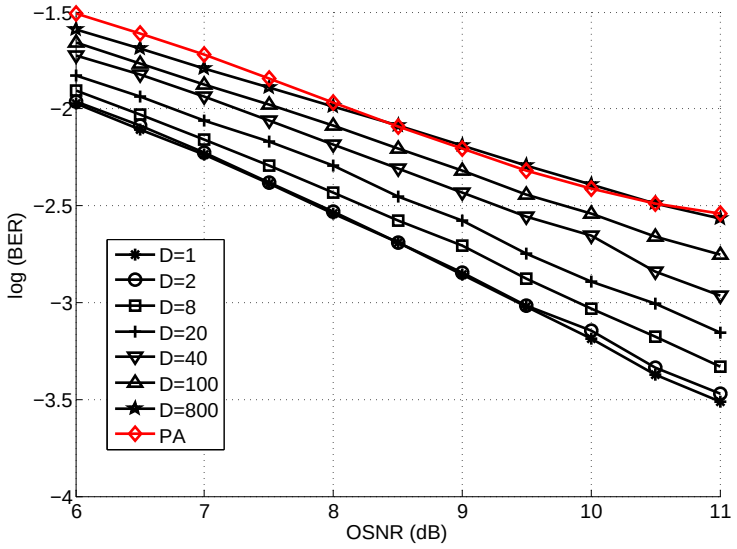

Figure 5.6: OSNR sensitivities for different values of D after 800-km transmission with 50° phase and 2-dB amplitude imbalance.

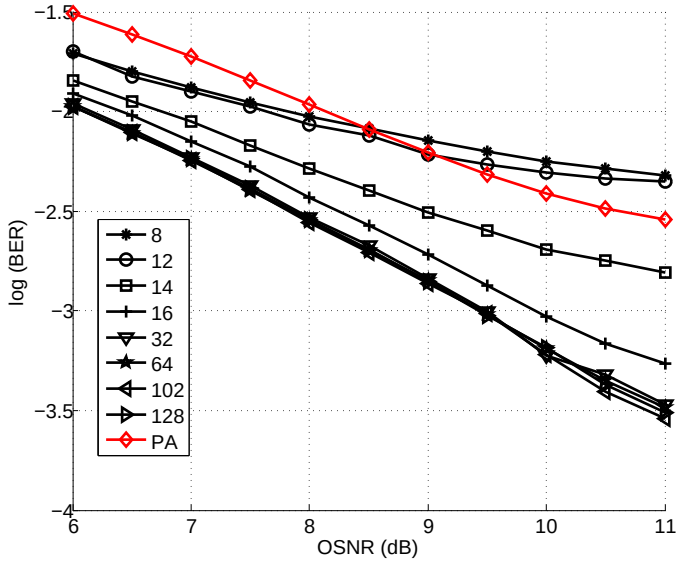

Figure 5.7: OSNR sensitivities for different number of PSC after 800-km transmission with 50° phase and 2-dB amplitude imbalance.

ble and thus more accurate after a longer data sequence.Thus, we can expect a lower pilot symbol overhead for DAJC by increasing the frame size, especially at higher OSNR values.

With the decision-aided stage incorporated into DAJC, the computational complexity is increased with respect to the PA method. However, we can apply the DA stage only once every D symbols. D is a parameter to weigh the trade-off between complexity and performance. Fig. 5.6 illustrates the influence of D on the performance of DAJC with 800 symbols per frame over 800-km transmission with 50° phase and 2-dB amplitude mismatch. When D is increased from 1 to 20, the OSNR penalty at a BER of 10^{-3} is increased by 1 dB, while the computational complexity is reduced significantly by about 95%. The case of $D = 800$ totally removes the decision-aided stage from our method, and its performance becomes similar to that of the PA method.

Different from the PA method, our method utilizes all the subcarriers as pilots in the preamble in previous simulations. As a matter of fact, we can reduce the number of PSCs and estimate the channel matrix by interpolation. In Fig. 5.7, we compare the BER curves with different number of PSCs under the same case as in Fig. 5.6. The location of PSCs is randomly set, and the optimal value is chosen out of 10 settings for the 8-dB OSNR case. When the percentage of PSCs out of total subcarriers is larger than a certain threshold, say, 25%, the performance is not affected much by reducing the number of PSCs. The overhead can thus be further reduced (e.g., by 75%) without affecting the performance. It is expected that our DAJC method will perform even better in the real situations where the channel transfer function and the IQ mismatch factors are likely to change with time.

For the PA method [36], the required number of estimation per OFDM frame is once only. As discussed, if our proposed DA method is employed every D symbols and the OFDM frame size is L, the required number of estimation per OFDM frame is L/D. Our DA method is more computationally complex than the PA method. The parameter D could be carefully chosen to achieve tradeoff between performance and complexity.

5.1.3 Conclusion

This section describes a decision-aided joint compensation method for channel distortion and Tx IQ imbalance. We inserted 2 pilot symbols into each OFDM frame to jointly estimate the channel transfer function and IQ imbalance factor, and updated the estimation after every decision making stage. Simulations

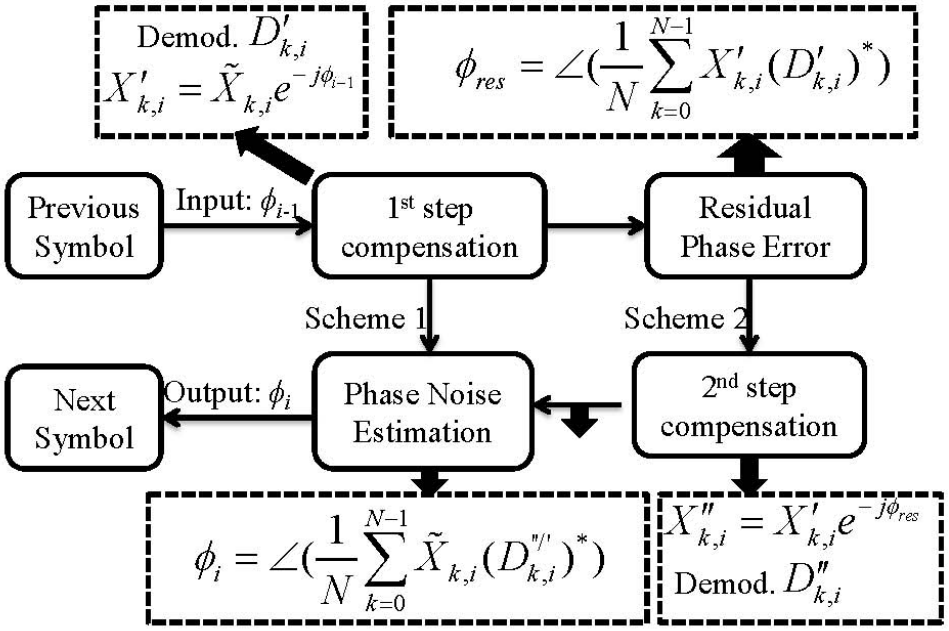

Figure 5.8: Block diagram for decision-aided phase estimation.

showed that our proposed DAJC method can achieve better performance with simpler pilot structure and lower overhead than existing methods.

5.2 DAJC and LPN

In this section, we investigate our DAJC method in the presence of linear phase noise. To combat linear phase noise, we propose a second step in addition to our DAJC method. After the Tx IQ mismatch and channel distortion have been removed using the DAJC method described in section 5.1, we compensate for the linear phase noise in a decision-aided manner, as described in Fig. 5.8. $\tilde{X}_{k,i}$, $X'_{k,i}$ and $X''_{k,i}$ are the received signals after ZF, ZF & scheme1, and ZF & scheme 2, while $D'_{k,i}$ and $D''_{k,i}$ ($\pm 1 \pm j$) are the demodulated signals from $X'_{k,i}$ and $X''_{k,i}$.

In scheme 1, we first compensate for linear phase noise by removing the CPE estimated from the previous symbol, i.e., ϕ_{i-1}. The compensated signal ($X'_{k,i}$) is then demodulated ($D'_{k,i}$) and its common phase error (ϕ_i) is estimated using the received signal ($\tilde{X}_{k,i}$) as well as the decision ($D'_{k,i}$). The common phase error of the current symbol (ϕ_i) is then passed to the next OFDM symbol for its compensation. In Scheme 2, after 1^{st} step of compensation and demodulation, the residual phase error (ϕ_{res}) is calculated from the compensated signal ($X'_{k,i}$) and the demodulated signal ($D'_{k,i}$). We then apply 2^{nd} step compensation by removing the residual phase error from $X'_{k,i}$. The newly compensated signal ($X''_{k,i}$) is demodulated ($D''_{k,i}$). In scheme 2, the CPE of the current symbol (ϕ_i) is calculated from the received signal ($\tilde{X}_{k,i}$) and final decisions ($D''_{k,i}$). The CPE of the current symbol (ϕ_i) is also passed to the next OFDM symbol for its compensation.

In a word, scheme 1 directly derotates the current symbol by the CPE estimation ϕ_{i-1} obtained from the previous symbol. Scheme 2 employs one more iteration to compensate for the residual phase error, which is the mean phase difference between $D'_{k,i}$ and $X'_{k,i}$. This iteration greatly improves the performance, especially for larger laser linewidth. Finally, a new CPE estimation ϕ_i for next symbol is calculated as the mean phase difference between $D'_{k,i}$ (or $D''_{k,i}$) and $\tilde{X}_{k,i}$ for scheme 1 or 2, respectively.

To investigate the performance of the decision-aided joint compensation technique, we built a CO-OFDM system at 20 Gb/s using VPI TransmissionMaker. The OFDM signal was modulated using 4QAM and contained 256 subcarriers with a cyclic prefix length of 32 samples. 128 out of a total of 256 subcarriers carried data, and the other half were zero-padded for oversampling

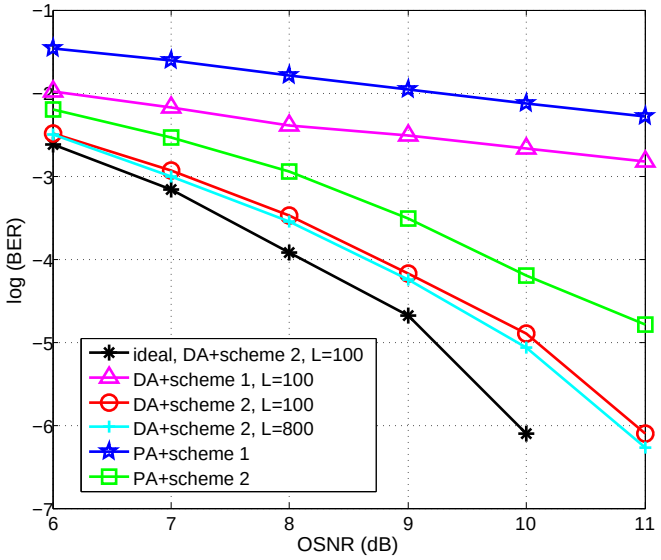

Figure 5.9: BER performance for DA(or PA) + scheme 1 (or 2) with $L = 100$ (or 800) for case ($\theta = 10°$, $\eta = 1$ dB, 60 kHz, 200 km) and ideal case ($\theta = 0°$, $\eta = 0$ dB, 0 kHz, 200 km).

purpose. 2 pilot symbols are added at the beginning of the OFDM frame. The training symbol is inserted only once to start the decision-aided process. In all simulations, the signals are transmitted over 2 spans of 100-km SMF and optical amplifier with 6-dB noise figure, without inline dispersion compensation. At the receiver side, digital coherent detection with polarization diversity is employed. PA [36] was implemented for performance comparison. Only frequency-independent mismatch is considered. Amplitude mismatch is measured in dB, where $\eta = 0.5$ corresponds to 3 dB.

Fig. 5.9 compares the four compensation schemes: DA & scheme1, DA & scheme 2, PA & scheme 1 and PA & scheme 2 in the setting of $10°$ phase and 1-dB amplitude mismatch. In the simulation, Tx and Rx lasers have a linewidth both equal to 60 kHz. The ideal case with zero linewidth and no IQ mismatch is plotted. For simplicity, we keep $\gamma_g = \gamma_h = \gamma$ and the optimal γ is found

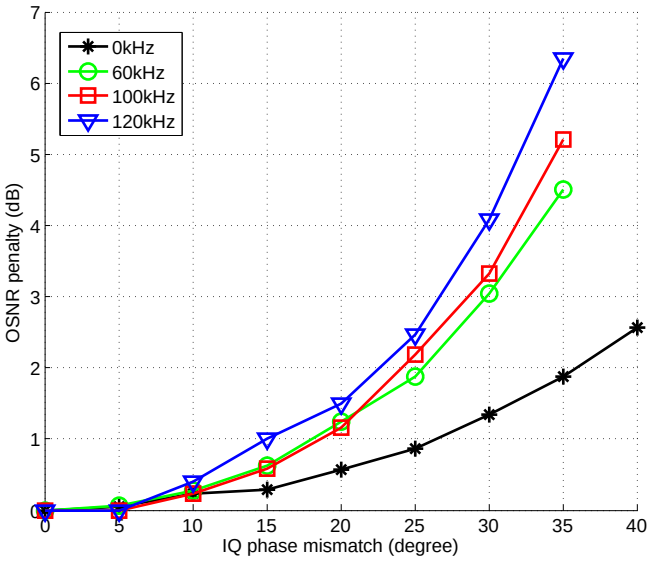

Figure 5.10: OSNR penalty versus IQ phase mismatch after 200-km transmission with Tx and Rx laser linewidths = 0 kHz, 60 kHz, 100 kHz and 120 kHz.

to be 0.9, which is used in simulations for Fig. 5.9, 5.10, 5.11. DA & scheme 2 performs best out of the four schemes, with only 0.5-dB or 0.8-dB OSNR penalty at the BER value of 10^{-3} or 10^{-4}. In later simulations, we only focus on DA & scheme 2. An OFDM frame in VPI contains a certain number of training symbols and data symbols. L is the number of data symbols after the preamble. As shown in the figure, an increase in L (from 100 to 800) even improves the performance. This is because the longer sequence averages out the noise, which helps improve the performance. So the preamble only needs to be inserted once in this decision-aided scheme.

Fig. 5.10 and Fig. 5.11 show the OSNR penalty for BER of 10^{-3} versus transmitter IQ phase and amplitude mismatch, respectively. The received OSNR is 7 dB for no IQ mismatch case. From the figure, it is observed that under 2-dB OSNR penalty, the tolerable phase mismatches are $36°$, $26°$, $24°$ and $22°$, while

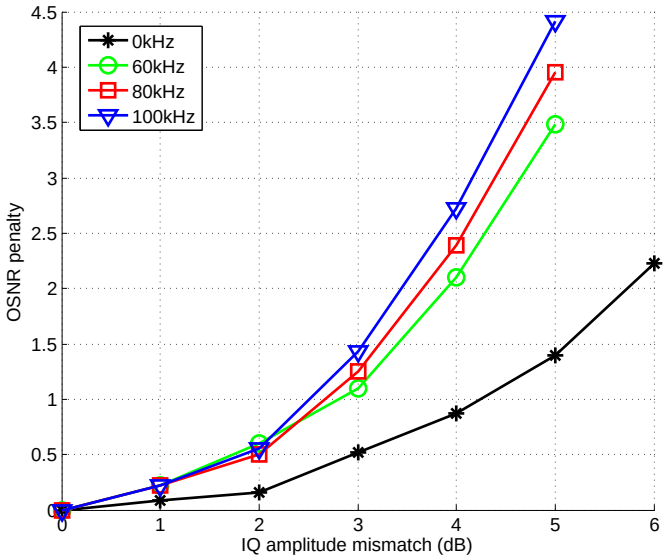

Figure 5.11: OSNR penalty versus IQ amplitude mismatch after 200-km transmission with Tx and Rx laser linewidths = 0 kHz, 60 kHz, 80 kHz and 100 kHz.

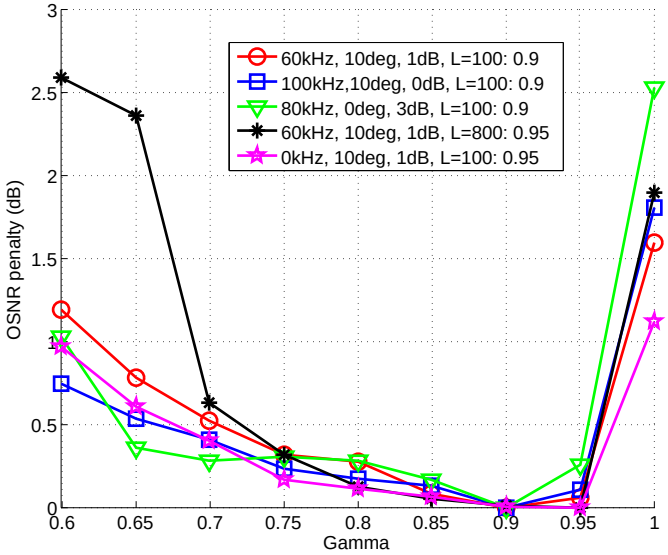

Figure 5.12: OSNR penalty for non-optimal γ for different parameters (laser linewidth, IQ phase mismatch, amplitude mismatch, frame size).

the tolerable amplitude mismatches are 5.6 dB, 3.9 dB, 3.7 dB and 3.4 dB, for 0-kHz, 120-kHz, 160-kHz and 200-kHz combined laser linewidths, respectively. It shows that our method is effective in mitigating both IQ mismatch and phase noise at the same time.

The optimal γ for different parameters (OSNR, θ, η and L) is slightly different, but a value of 0.9 was found to be performing well in all cases, as illustrated in Fig. 5.12 with a few different settings. The OSNR penalty between the optimal $gamma$ and 0.9 was less than 0.2 dB. In real experiment, γ may be tuned according to the changing speed of channel and IQ mismatch parameters.

5.3 Pre-distortion versus Post-equalization

All of the previous schemes are based on post-equalization (PE) only. Pre-distortion (PD) schemes have also been widely used in OFDM systems to compensate for channel distortion and nonlinearity. In this section, we propose a new pre-distortion scheme for compensating IQ mismatch in the presence of channel distortion. PD and PE schemes are compared in a simulated system at 56 Gb/s per polarization. PE requires lower OSNR than PD under small values of IQ phase and amplitude mismatch. For larger values of IQ mismatch, PD is performing better than PE and has much larger tolerance.

As shown by Eq. 5.9, each subcarrier experiences interference proportional to G from its mirror-image position subcarrier under IQ mismatch. And an even number $2L$ of training symbols is transmitted to provide an estimation of G and

H_k as follows:

$$\begin{cases} Y_{k,2i-1} = H_k(X_{k,2i-1} + G\bar{X}^*_{k,2i-1}) \\ Y_{k,2i} = H_k(X_{k,2i} + G\bar{X}^*_{k,2i}) \end{cases} \tag{5.21}$$

$$\begin{cases} G = \frac{1}{LN}\sum_{i=1}^{L}\sum_{k=0}^{N-1}\frac{Y_{k,2i}X_{k,2i-1} - Y_{k,2i-1}X_{k,2i}}{Y_{k,2i-1}\bar{X}^*_{k,2i} - Y_{k,2i}\bar{X}^*_{k,2i-1}} \\ H_k = \frac{1}{2L}\sum_{i=1}^{2L}\frac{Y_{k,i}}{X_{k,i}+G\bar{X}^*_{k,i}} \end{cases} \tag{5.22}$$

After the estimation is obtained, zero-forcing is imposed either at Tx side or Rx side for PD or PE as in Eq. 5.18.

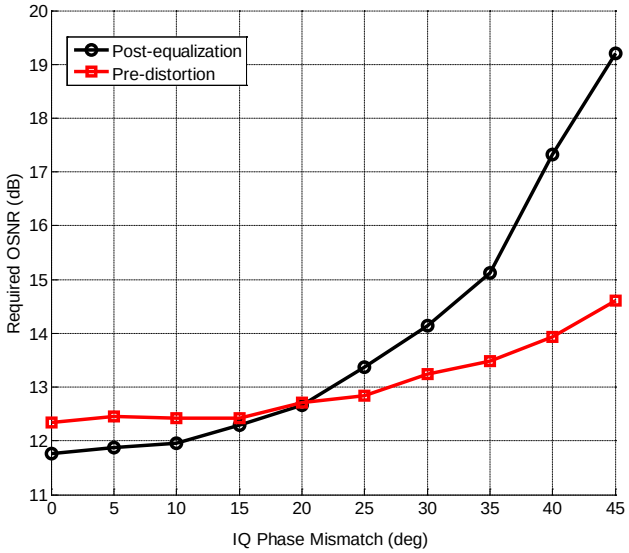

Figure 5.13: Required OSNR versus IQ phase mismatch after 400-km transmission for PE and PD.

To investigate the performance of the PD and PE compensation schemes, we built a CO-OFDM system using VPI Transmission Maker and MATLAB. The system setup is identical to the 112-Gb/s standard system [92], but only one polarization is considered here. To exclude the effect of linear phase noise, we

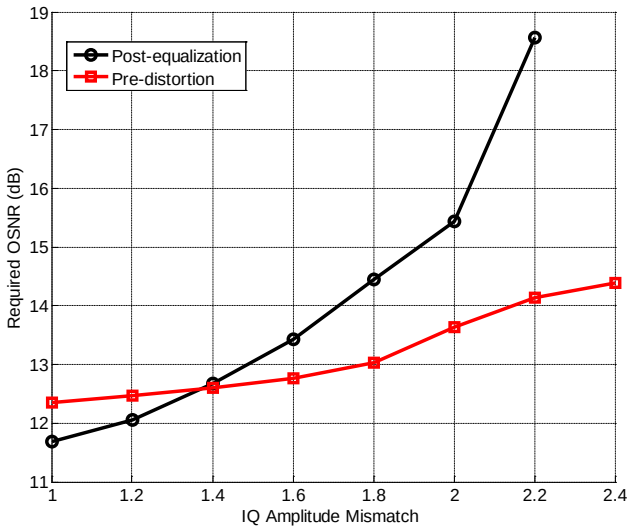

Figure 5.14: Required OSNR versus IQ amplitude mismatch after 400-km transmission for PE and PD.

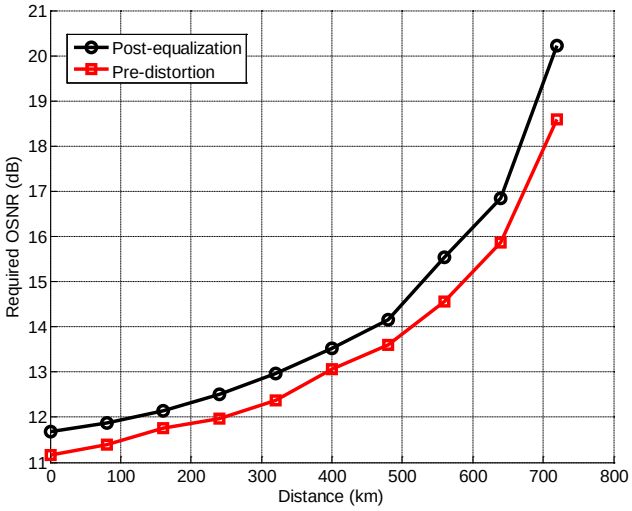

Figure 5.15: Required OSNR versus transmission distance with $\theta = 15^{\circ}$ and $\eta = 1.5$ for PE and PD

set the linewidths of Tx laser and the local oscillator to zero. The performance was evaluated in transmission over 5 spans of 80-km SSMF and EDFA (noise figure = 6 dB) without optical dispersion compensation. Two training symbols are used for estimation, followed by a frame of 50 data symbols. A total number of 15 frames are used to obtain the curve.

Fig. 5.13 shows the required OSNR for a target BER of 10^{-3} versus Tx IQ phase mismatch over 400-km transmission for PE and PD. Fig. 5.13 compares the required OSNR versus Tx IQ amplitude mismatch under the same case. For an IQ phase mismatch value smaller than 20°, PE requires lower OSNR value compared to PD. Under 1-dB or 2-dB OSNR penalty, the tolerable phase mismatch is 32° or 43° for PD and 21° or 28° for PE. For an IQ amplitude mismatch value smaller than 1.4, PE is performing better than PD. Under 1-dB or 2-dB OSNR penalty, the tolerable amplitude mismatch is 1.9 or 2.4 for PD and 1.4 or 1.65 for PE. For both phase and amplitude mismatch, PE outperforms PD when the mismatch value is small ($\theta < 20^{\circ}$ or $\eta < 1.4$), and PD performs better when the mismatch value exceeds the threshold. PD has larger phase or amplitude mismatch tolerance than PE.

Fig. 5.15 shows the required OSNR value for different spans of transmission (1 to 9) when η is equal to 1.5 and θ is equal to 15°. PD requires about 0.5-dB less OSNR when the transmission distance is smaller than 500 km. And the OSNR penalty differences are as big as 1 dB and 1.6 dB respectively for transmission distance of 560 km (or 640 km) and 720 km.

5.4 Conclusion

In this chapter, we investigated the system model with carrier frequency offset, linear phase noise, Tx and Rx IQ mismatch and channel distortion. Based on the model, the correct order of compensation should be: (1) Rx IQ mismatch compensation (GSOP), (2) frequency offset compensation, (3) Tx IQ mismatch and channel distortion compensation. We have proposed a decision-aided joint compensation method for Tx IQ mismatch and channel distortion. In addition to DAJC, we further propose a second phase compensation stage to deal with the linear phase noise. Simulation results show that our proposed algorithm can effectively mitigate Tx IQ mismatch, channel distortion and linear phase noise at the same time. Lastly, we propose a pre-distortion scheme for compensating Tx IQ mismatch in the presence of channel distortion for CO-OFDM system, which is compared with post-equalization through simulation. PE is performing better than PD for smaller phase or amplitude mismatch values while PD has larger tolerance towards the mismatch.

Chapter 6

Log-likelihood Ratio for LDPC Coded OFDM System with Linear Phase Noise

Graph-based low-density parity-check (LDPC) codes have become standard in many communication applications, including digital video broadcasting (DVB-S2) [26, 27], 10 Gigabit Ethernet (10GBASE-T) [28], broadband wireless access (WiMax) [29], wireless local area network (WiFi) [30], deep-space communications [31], and magnetic storage in hard disk drives [32]. LDPC codes, invented by Gallager [52] in 1960s, have been proved to achieve close to Shannon limit performance [49]. LDPC codes are linear block codes for which the parity check matrix has low density of ones. LDPC coded orthogonal frequency division multiplexing (OFDM) is a suitable coded modulation technique for long-haul optical communication [33]. Compared to single carrier, OFDM is more robust to chromatic dispersion and polarization mode dispersion. Re-

cently, there have been quite a few experimental demonstrations using LDPC coded coherent optical OFDM (CO-OFDM) for high speed long-haul transmission [34, 35]. However, CO-OFDM is prone to linear phase noise. In this chapter, we will study the performance of LDPC coded OFDM system in the presence of linear phase noise. The performance of decoding algorithms depends on the calculation of the decoding metric, i.e., the log-likelihood ratio (LLR). Previously, all the conventional LLR metrics (Gaussian metric for differential BPSK or conventional metrics for MPSK, M-QAM) are only calculated from the received signal, without the consideration of linear phase noise statistics. Here, we propose to analytically derive new log-likelihood ratios for both differential M-ary phase shift keying (DMPSK) system (6.1) and pilot-aided M-ary phase shift keying (PA-MPSK) system (6.2) with linear phase noise. Lastly, we derive the LLR for non-constant amplitude modulation format, M-QAM OFDM with linear phase noise in section 6.3. All the LLR metrics have been verified through simulation. The plotted BER curves in the chapter are all corrected BER values after LDPC decoding.

6.1 LLR for LDPC Coded DMPSK-OFDM

Differential encoding has been used in single carrier systems to offer a simple solution to linear phase noise by using the leading signal as a phase reference. The detection of a transmitted symbol is based on two consecutive received signals. In CO-OFDM systems, the carrier phase does not vary much across different subcarriers. Ignoring the intercarrier interference, the unknown phase noise within the same OFDM symbol are assumed to be constant over different sub-

carriers, defined as the common phase error (CPE). Thus, differential encoding might be helpful in combatting CPE if it is applied across the frequency domain of each OFDM symbol. In 6.1.1, we study the performance of LDPC coded differential BPSK (DBPSK) OFDM system transmitting over AWGN channel with unknown linear phase noise. We extend this work to differential MPSK (DMPSK) OFDM system in 6.1.2.

6.1.1 Differential Binary PSK

In this section, we investigate the performance of an LDPC coded DBPSK-OFDM system in AWGN channel with unknown carrier phase. Firstly, the system model is introduced. Secondly, we derive the LLR and approximate-LLR (A-LLR) metrics based on the joint pdf of the two consecutive received signals, conditioned on each possible value of the code bit concerned, similar to [93] for the single carrier case. We model the CPE as a random variable uniformly distributed over the interval $[-\pi, \pi)$. Finally, simulation results are presented. The performance of the LLR and A-LLR metrics derived in this section are compared with the Gaussian metric (GM) in [94].

The system model of LDPC coded DBPSK-OFDM is shown in Fig. 6.1. A binary message sequence $\boldsymbol{m} = [m_1, m_2, \cdots, m_K]$ is first encoded by an LDPC encoder to a code word $\boldsymbol{c} = [c_1, c_2, \cdots, c_N]$, with a code rate equal to K/N. The code word is modulated with DBPSK format to become $\boldsymbol{s} = [s_1, s_2, \cdots, s_N]$, where $s_k = \sqrt{E_s}\exp(j\alpha_k)$, with E_s as the energy of the signal and $\alpha_k \in \{0, \pi\}$. The information of the code bit is carried in the phase difference of two consecutive signals s_k and s_{k-1}: $\alpha_k = \alpha_{k-1} + \Delta\alpha_k$, where $\Delta\alpha_k$ is equal to 0 if $c_k = 0$

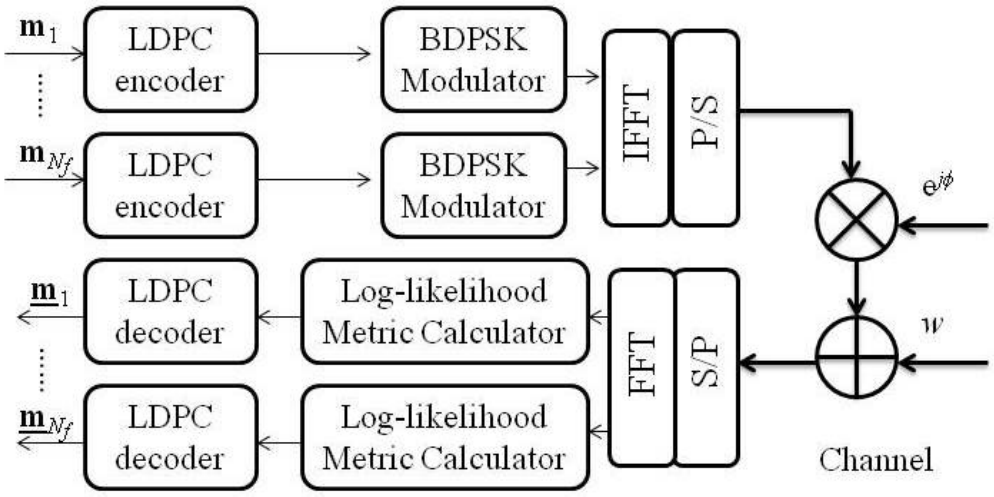

Figure 6.1: LDPC coded BDPSK-OFDM system model (N_f: number of frames, w: AWGN noise, ϕ: unknown carrier phase).

and π otherwise. Differential encoding is realized across subcarriers within one OFDM symbol. $\boldsymbol{s}$ is then zero-padded to a length of N_{FFT}, which constitutes the subcarriers of one OFDM symbol. After taking IFFT and P/S, we transmit the signal over an AWGN channel with unknown carrier phase. The received signal after FFT is modeled as:

$$r_{ik} = s_{ik}e^{j\phi_i} + w_{ik}, i = 1, \cdots, N_f, k = 1, \cdots, N_{FFT} \tag{6.1}$$

where r_{ik}, s_{ik}, w_{ik} and ϕ_i are the frequency domain received signal, transmitted signal, AWGN, and unknown carrier phase at time instant i, respectively. i and k stand for the time and frequency subscripts. In the model, it is assumed that intercarrier interference is ignored and only common phase error is considered. Although Eq. 6.1 is derived in AWGN channel, it is also applicable to optical channel assuming the channel distortion is removed first.

At the receiver, the LLR metric is calculated based on the received signal

and passed to the iterative LDPC decoder, where the estimated message $\underline{\boldsymbol{m}}$ is obtained. Because individual LDPC encoder/decoder is used for different subscript i, we can drop this subscript when deriving the LLR metrics for decoder. The information of code bit c_k is contained in the two received signals r_k and r_{k-1} with consecutive frequency domain subscripts. According to [93], the LLR metric $L(k)$ is defined as:

$$L(k) = \ln \frac{p(c_k = 0|r_k, r_{k-1})}{p(c_k = 1|r_k, r_{k-1})} \tag{6.2}$$

The event of $\{c_k = l\}$ is equivalent to the event of $\{\Delta\alpha_k = l\pi\}$, for $l = 0, 1$. Because the priori probabilities of c_k are equal, we can rewrite Eq. 6.2 as:

$$L(k) = \ln \frac{p(r_k, r_{k-1}|\Delta\alpha_k = 0)}{p(r_k, r_{k-1}|\Delta\alpha_k = \pi)} \tag{6.3}$$

Following a similar procedure as in [93], we first evaluate the joint pdf ($p(r_k, r_{k-1}|\Delta\alpha_k)$) conditioned on ϕ. For a memoryless channel, the likelihood function can be expressed as:

$$\begin{aligned} & p(r_k, r_{k-1}|\Delta\alpha_k = l\pi, \phi) \\ &= \frac{1}{2} p(r_k|\alpha_k = 0, \phi) \cdot p(r_{k-1}|\alpha_{k-1} = l\pi, \phi) \\ &+ \frac{1}{2} p(r_k|\alpha_k = \pi, \phi) \cdot p(r_{k-1}|\alpha_{k-1} = (1-l)\pi, \phi) \end{aligned} \tag{6.4}$$

where:

$$p(r_k|\alpha_k = l\pi, \phi) = \frac{1}{\pi N_0} \exp\Big[- \frac{|r_k - (-1)^l E_s^{\frac{1}{2}} e^{j\phi}|^2}{N_0} \Big] \tag{6.5}$$

Substituting Eq. 6.5 in Eq. 6.4, we have [93]:

$$\begin{aligned} & p(r_k, r_{k-1}|\Delta\alpha_k = l\pi, \phi) \\ = \ & \frac{1}{2}C\Big\{ \exp\Big[\frac{2E_s^{\frac{1}{2}}}{N_0}|r_k + (-1)^l r_{k-1}| \cdot \cos(\angle(r_k + (-1)^l r_{k-1}) - \phi)\Big] \\ + \ & \exp\Big[- \frac{2E_s^{\frac{1}{2}}}{N_0}|r_k + (-1)^l r_{k-1}| \cdot \cos(\angle(r_k + (-1)^l r_{k-1}) - \phi)\Big]\Big\} \end{aligned} \quad (6.6)$$

where

$$C = \frac{\exp[-\frac{1}{N_0}(|r_k|^2 + |r_{k-1}|^2 + 2E_s)]}{(\pi N_0)^2} \quad (6.7)$$

The above equation could be simplified as:

$$\begin{aligned} & p(r_k, r_{k-1}|\Delta\alpha_k = l\pi, \phi) \\ = \ & C\cosh\Big[\frac{2E_2^{\frac{1}{2}}}{N_0}|r_k + (-1)^l r_{k-1}| \cdot \cos(\angle(r_k + (-1)^l r_{k-1}) - \phi)\Big] \end{aligned} \quad (6.8)$$

We assume that ϕ is a random variable uniformly distributed in the interval $[-\pi, \pi)$. To remove the dependence on ϕ, we integrate the conditional pdf over all possible values of ϕ.

$$p(r_k, r_{k-1}|\Delta\alpha_k = l\pi) = \int_\phi p(r_k, r_{k-1}|\Delta\alpha_k = l\pi, \phi)p(\phi)d\phi \quad (6.9)$$

After substituting Eq. 6.8 into Eq. 6.9, we obtain:

$$p(r_k, r_{k-1}|\Delta\alpha_k = l\pi) = CI_0\Big[\frac{2E_s^{\frac{1}{2}}}{N_0}|r_k + (-1)^l r_{k-1}|\Big] \quad (6.10)$$

where $I_0[|x|] = \frac{1}{2\pi}\int_{-\pi}^{\pi}\exp[|x|\cos\phi]d\phi$ is the zeroth-order modified Bessel

function. Our resulting LLR is calculated as:

$$L(k) = \ln \frac{I_0\left[\frac{2E_s^{\frac{1}{2}}}{N_0}|r_k + r_{k-1}|\right]}{I_0\left[\frac{2E_s^{\frac{1}{2}}}{N_0}|r_k - r_{k-1}|\right]} \tag{6.11}$$

For high SNR such that $\frac{E_s}{N_0} >> 1$, the metric can be approximated as approximate-LLR (A-LLR):

$$L(k) \approx \frac{2E_s^{\frac{1}{2}}}{N_0}[|r_k + r_{k-1}| - |r_k - r_{k-1}|] \tag{6.12}$$

The calculation of A-LLR is much computationally simpler than the calculation of LLR, with the modified Bessel function, which requires integration, and the ln() operation being removed. For comparison with our LLR, GM [94] is employed here:

$$L(k) = \frac{2E_s \,\mathrm{Re}[r_k r_{k-1}^*]}{\sigma^2} \tag{6.13}$$

where $\sigma^2 = E_s N_0 + (N_0/2)^2$. From Eq. 6.12 and Eq. 6.13, we can conclude that the A-LLR metric and the GM involve only a few complex multiplication/addition and they have the same order of computational complexity.

In the simulation, half-rated, regular (204,102) binary LDPC codes [95] is used with IDFT/DFT size of 256. The noise variance is assumed to be known at the receiver side. In the first case, ϕ is assumed to be constant over different subcarriers in one symbol. Fig. 6.2 shows the BER performance of GM and our LLR metrics against SNR per information bit, E_b/N_0, where E_b is the energy per information bit. The performance gain of our LLR over GM is about 0.12

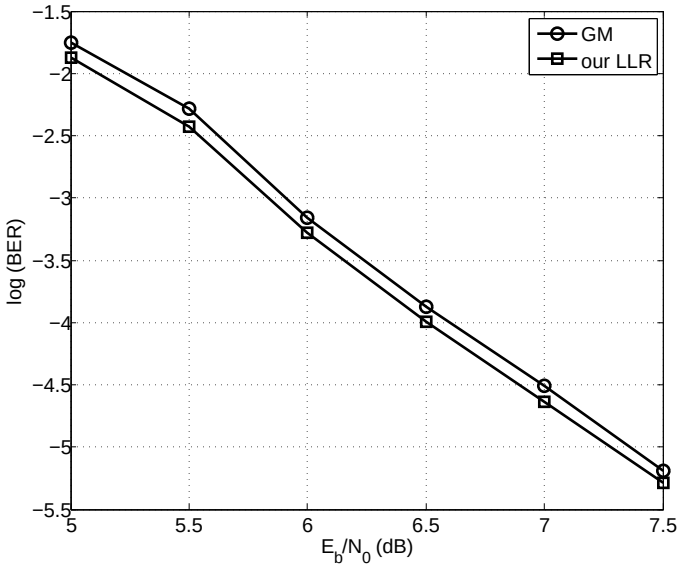

Figure 6.2: BER performance of (204,102) LDPC coded DBPSK OFDM signal over noncoherent AWGN channel.

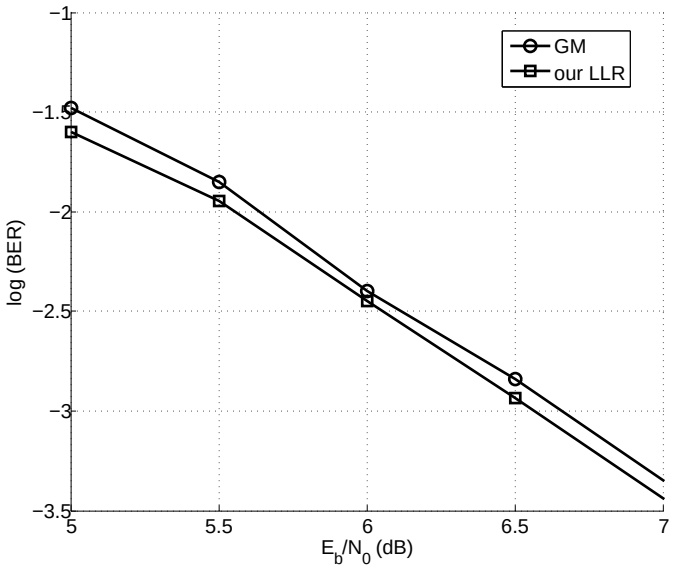

Figure 6.3: BER performance of (204,102) LDPC coded DBPSK OFDM signal over noncoherent AWGN channel with phase noise $\sigma^2 = 5 \cdot 10^{-4}$.

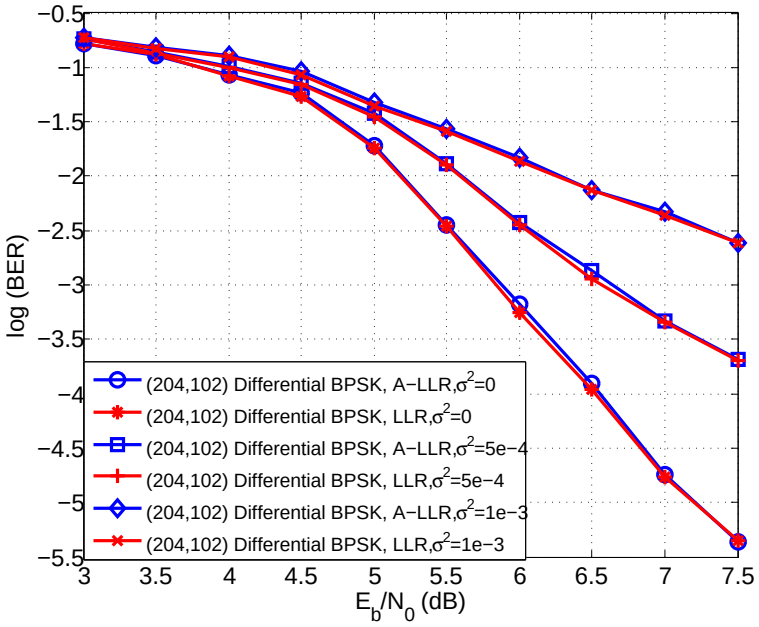

Figure 6.4: BER performance of (204,102) LDPC coded DBPSK OFDM signal over noncoherent AWGN channel with different phase noise statistics $\sigma^2 = 0, \sigma^2 = 5 \cdot 10^{-4}, \sigma^2 = 10^{-3}$.

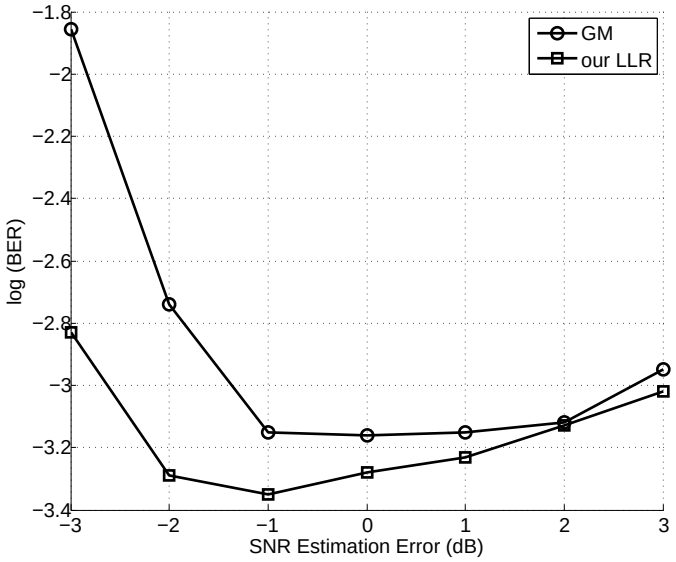

Figure 6.5: BER performance of (204,102) LDPC coded DBPSK OFDM signal over noncoherent AWGN channel at $E_b/N_0 = 6$ dB, subjected to SNR estimation error.

dB at BER of 10^{-4}.

In the second case, the unknown carrier phase is modeled as a random-walk process: $\phi_k = \phi_{k-1} + n_{\phi_k}$, where $\{n_{\phi_k}\}$ is independent, identically distributed Gaussian random variables with zero mean and variance σ^2. In Fig. 6.3, we plot the BER curve using GM or our LLR metrics in the presence of phase noise where $\sigma^2 = 5{\cdot}10^{-4}$. This σ^2 value corresponds to a 800-kHz (v) combined laser linewidth ($\sigma^2 = 2\pi v T_s$) in 10-Gsample/s OFDM system. Our LLR requires 0.09-dB less SNR compared to GM at BER of 10^{-3}.

In Fig. 6.4, we plot the BER curve using our LLR and A-LLR metrics in the presence of different phase noise statistics: $\sigma^2 = 0, \sigma^2 = 5 \cdot 10^{-4}, \sigma^2 = 10^{-3}$. It is observed that LLR and A-LLR metric achieve almost the same performance in different cases.

Fig. 6.5 shows the effect of estimation error in SNR on the performance with time-invariant unknown carrier phase at 6-dB SNR. Both metrics are more tolerant to SNR over-estimation than under-estimation. The tolerable SNR under-estimation value is -2.7 dB for our LLR and -1.7 dB for GM at two-times BER degradation (a difference of 0.3 in y axis).

In conclusion, our LLR metric (Eq. 6.11) is performing slightly better than the GM metric (Eq. 6.13), with larger tolerance to SNR under-estimation error. A-LLR metric (Eq. 6.12) has almost identical performance compared to the LLR metric (Eq. 6.11) but with much lower computational complexity.

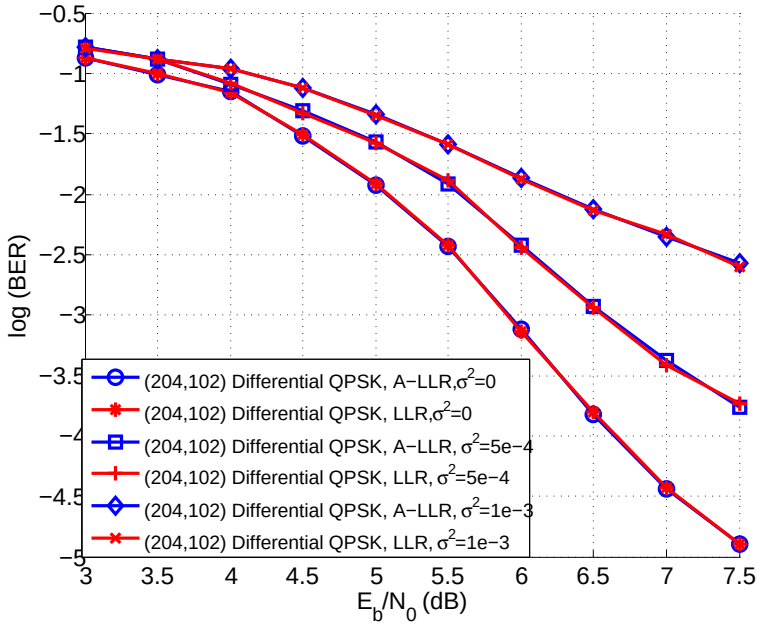

Figure 6.6: BER performance of (204,102) LDPC coded DQPSK OFDM signal over noncoherent AWGN channel with different phase noise statistics $\sigma^2 = 0, \sigma^2 = 5 \cdot 10^{-4}, \sigma^2 = 10^{-3}$.

6.1.2 Differential M-ary PSK

In the previous section, we derived the LLR metric for DBPSK OFDM system in the presence of linear phase noise. In this section, we expand our derivation to more general case: differential M-ary PSK OFDM system.

For DMPSK modulation, the LLR metric for bit m of signal k ($m = 0, \cdots, \log_2(M)$, $k = 0, 1, \cdots, N-1$) is defined as:

$$L(c_{k,m}) = \ln \frac{p(c_{k,m} = 0 | r_k, r_{k-1})}{p(c_{k,m} = 1 | r_k, r_{k-1})} \tag{6.14}$$

For DMPSK, the code bits are gray-coded in the phase difference of two

consecutive signals s_k and s_{k-1}:

$$\alpha_k = \alpha_{k-1} + \Delta\alpha_k \tag{6.15}$$

$$\Delta\alpha_k = \frac{2\pi m}{M}(m = 0, \cdots, M-1) \tag{6.16}$$

Assuming the priori probabilities of c_k are equal, we can rewrite Eq. 6.14 by replacing the code bits with the phase differences:

$$L(c_{k,m}) = \ln \frac{\sum_{\Delta\alpha_k \in \mathbf{P}_+} p(r_k, r_{k-1}|\Delta\alpha_k)}{\sum_{\Delta\alpha_k \in \mathbf{P}_-} p(r_k, r_{k-1}|\Delta\alpha_k)} \tag{6.17}$$

where $\mathbf{P}_+$ denotes the set of phase differences for which the m-th code bit is 0 and similarly $\mathbf{P}_-$ denotes the set of phase differences for which the m-th code bit is 1. We can calculate the probability term in the likelihood function by integrating $p(r_k, r_{k-1}|\Delta\alpha_k, \phi)$ over the unknown carrier phase ϕ:

$$\begin{aligned} p(r_k, r_{k-1}|\Delta\alpha_k) &= \int_{-\pi}^{\pi} p(r_k, r_{k-1}|\Delta\alpha_k, \phi)p(\phi)d\phi \\ &= \frac{1}{2\pi}\int_{-\pi}^{\pi} p(r_k, r_{k-1}|\Delta\alpha_k, \phi)d\phi \end{aligned} \tag{6.18}$$

Based on the Gaussian distribution of noise, we firstly derive the general probability of $p(r_k, r_{k-1}|\alpha_k = a, \alpha_{k-1} = b, \phi)$ as follows:

$$\begin{aligned} &p(r_k, r_{k-1}|\alpha_k = a, \alpha_{k-1} = b, \phi) \\ &= p(r_k|\alpha_k = a, \phi)p(r_{k-1}|\alpha_{k-1} = b, \phi) \\ &= \frac{1}{(\pi N_0)^2}\exp\Big\{-\frac{|r_k - E_s^{1/2}e^{j(\phi+a)}|^2 + |r_{k-1} - E_s^{1/2}e^{j(\phi+b)}|^2}{N_0}\Big\} \\ &= C\exp\Big\{\frac{2E_s^{1/2}}{N_0}[|z|\cos(\angle z - \phi)]\Big\} \end{aligned} \tag{6.19}$$

where $z = r_k e^{-ja} + r_{k-1} e^{-jb}$ and $C = \frac{\exp[-\frac{1}{N_0}(|r_k|^2+|r_{k-1}|^2+2E_s)]}{(\pi N_0)^2}$. Incorporating this result into the integration, we get:

$$\begin{aligned} & p(r_k, r_{k-1}|\alpha_k = a, \alpha_{k-1} = b) \\ &= C\Big\{\frac{1}{2\pi}\int_{-\pi}^{\pi} \exp\Big\{\frac{2E_s^{1/2}}{N_0}[|z|\cos(\angle z - \phi)]\Big\}d\phi\Big\} \\ &= CI_0\Big[\frac{2E_s^{1/2}}{N_0}|r_k e^{-ja} + r_{k-1}e^{-jb}|\Big] \\ &= CI_0\Big[\frac{2E_s^{1/2}}{N_0}|r_k + r_{k-1}e^{j\Delta\alpha_k}|\Big] \end{aligned} \tag{6.20}$$

where $I_0[|x|] = \frac{1}{2\pi}\int_{-\pi}^{\pi}\exp[|x|\cos\phi]d\phi$ is the zeroth-order modified Bessel function. The final LLR metric for M-ary PSK system is:

$$L(c_{k,m}) = \ln\frac{\sum_{\Delta\alpha\in\mathbf{P}_+} I_0\Big[\frac{2E_s^{1/2}}{N_0}|r_k + r_{k-1}e^{j\Delta\alpha}|\Big]}{\sum_{\Delta\alpha\in\mathbf{P}_-} I_0\Big[\frac{2E_s^{1/2}}{N_0}|r_k + r_{k-1}e^{j\Delta\alpha}|\Big]} \tag{6.21}$$

For high SNR such that $E_s/N_0 >> 1$, $I_0(x)$ may be approximated as $e^x/\sqrt{2\pi x}$. After the approximation and removal of the $\ln(*)$ term, we obtain the approximate LLR (A-LLR) metric:

$$L(c_{k,m}) \approx \frac{2E_s^{1/2}}{N_0}\Big[\max_{l\in\mathbf{P}_+}|r_k + r_{k-1}e^{j\Delta\alpha}| - \max_{l\in\mathbf{P}_-}|r_k + r_{k-1}e^{j\Delta\alpha}|\Big] \tag{6.22}$$

The calculation of A-LLR is much computationally simpler than the calculation of LLR, with the modified Bessel function, which requires integration, and the ln() operation being removed.

In the simulation, a half-rated regular (204,102) binary LDPC code [95] is used with IDFT/DFT size of 256. The noise variance is assumed to be known at

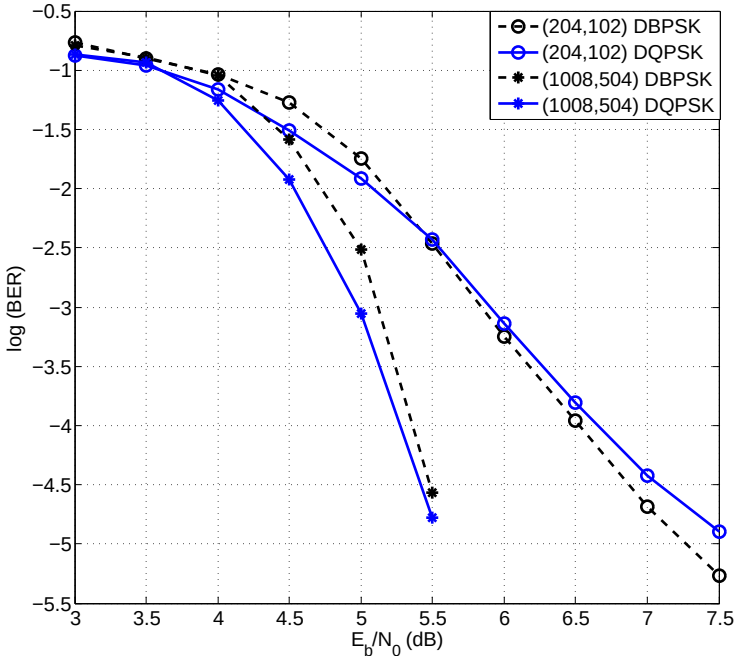

Figure 6.7: BER performance of DBPSK and DQPSK OFDM system using the LLR metric with different LDPC codes (204,102) and (1008, 504) using A-LLR ($\sigma^2 = 0$).

the receiver side.

In Fig. 6.6, we plot the BER curves of LDPC coded DQPSK OFDM system using our LLR and A-LLR metrics in the presence of different phase noise statistics: $\sigma^2 = 0, \sigma^2 = 5 \cdot 10^{-4}, \sigma^2 = 10^{-3}$. It is observed that LLR and A-LLR metrics achieve almost the same performance for DQPSK OFDM system with different phase noise statistics.

In Fig. 6.7, we compare the BER performance of DBPSK and DQPSK OFDM system using the A-LLR metric with different LDPC codes (204,102) and (1008, 504) for $\sigma^2 = 0$. In Fig. 6.8, BER curves with $\sigma^2 = 5 \cdot 10^{-4}$ are shown for the same parameters.

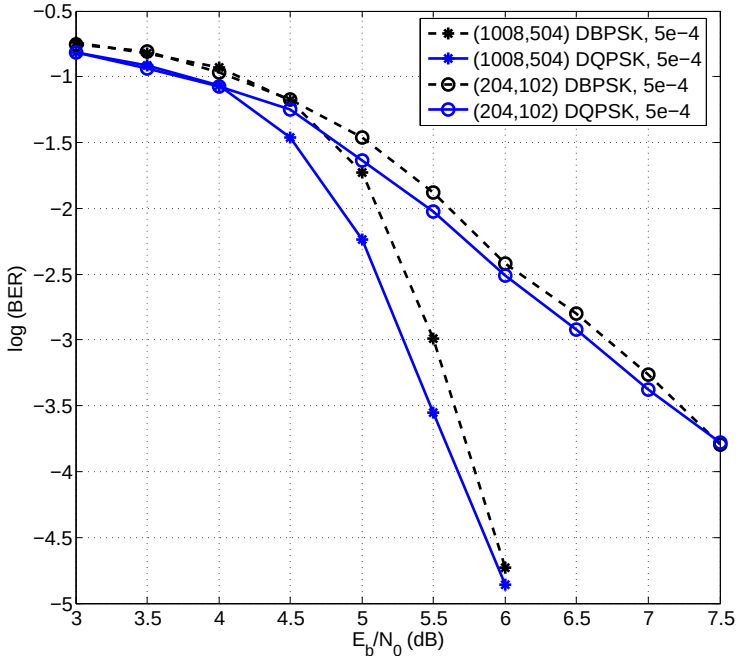

Figure 6.8: BER performance of DBPSK and DQPSK OFDM system using the LLR metric with different LDPC codes (204,102) and (1008, 504) using A-LLR ($\sigma^2 = 5 \cdot 10^{-4}$).

6.2 PA-LLR for LDPC Coded MPSK-OFDM

In this section, we will derive a pilot-aided LLR (PA-LLR) metric for LDPC coded M-ary PSK (MPSK) CO-OFDM with consideration of linear phase noise. The bit LLR metric is evaluated from the likelihood function, given the received signal which carries that bit, and a set of pilot subcarriers which carries the information of linear phase noise. A similar derivation of PA-LLR metric with respect to phase noise has been proposed for LDPC coded pilot-symbol assisted single carrier system [96]. In Pol-Mux LDPC coded coherent OFDM transmission [87], the authors also describe how to determine the symbols log-likelihood ratios in the presence of linear phase noise. The average likelihood function was obtained over all possible values of phase noise but no analytical expression was

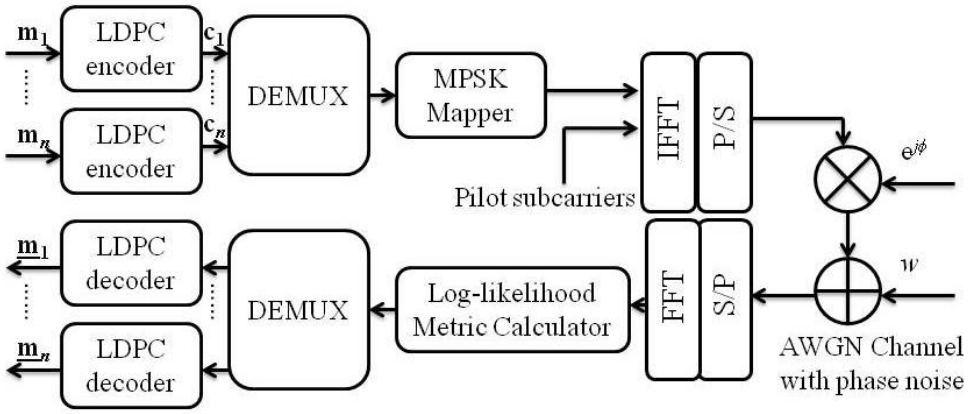

Figure 6.9: LDPC coded PA-MPSK-OFDM system model (DEMUX: demultiplexer, w: AWGN noise, ϕ: unknown phase noise).

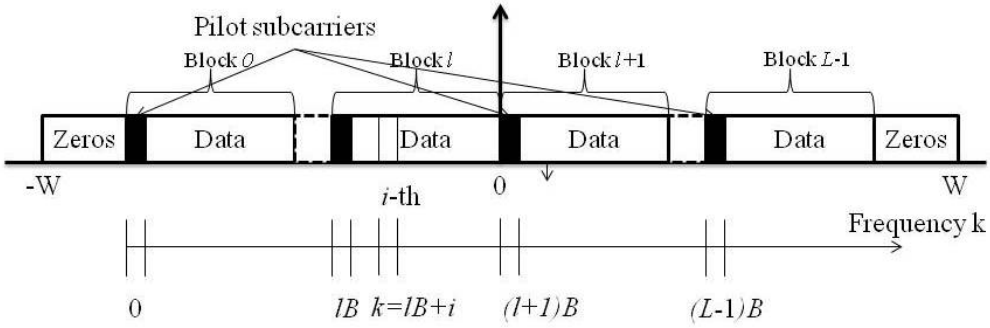

Figure 6.10: OFDM symbol structure in frequency domain.

given for the final metric. The metric is only obtained numerically [87].

6.2.1 System Model

The system model of LDPC coded pilot-aided BPSK-OFDM is shown in Fig. 6.9. On the transmitter side, the data streams $\{\boldsymbol{m}_1, \cdots, \boldsymbol{m}_n\}$ are encoded using identical LDPC codes to code words $\{\boldsymbol{c}_1, \cdots, \boldsymbol{c}_n\}$, with a code rate equal to K/N, where K and N are the vector length of $\boldsymbol{m}_i$ and $\boldsymbol{c}_i$, respectively. The outputs of these LDPC encoders are demultiplexed and parsed into groups of

$D * b$ bits, where D is the number of modulated subcarriers per symbol and b is the number of bits per constellation point. The b bits of each subcarrier are mapped into a complex-valued signal from the constellation of M-ary PSK. The modulated subcarriers together with the pilot subcarriers are zero-padded and further processed with length-N_{FFT} IFFT and parallel to serial transformation to construct one OFDM symbol.

The frequency-domain structure of one OFDM symbol is shown in Fig. 6.10. Suppose there are L pilots uniformly distributed at location lB ($l = 0, \cdots, L-1$) in one OFDM symbol, with $B-1$ data symbols between every two consecutive pilots. At time instant $k = lB + i (i = 1, \cdots, B-1, l = 0, 1, \cdots, L-1)$, the transmitted signal is $s(k) = E_s^{\frac{1}{2}} e^{j\alpha(k)}$. E_s and $\alpha(k) \in \{0, \pi\}$ denote the energy and information of $s(k)$, respectively. The first subcarrier in each block is the pilot with transmitted phase fixed at 0. The remaining $B-1$ subcarriers of each block correspond to LDPC-coded bits. The linear phase noise, which is a Wiener process, will introduce both common phase error (CPE) and inter-carrier interference (ICI). For deriving the PA-LLR, only CPE is considered and the received signal at the ith OFDM symbol and kth subcarrier can be modeled as [73]:

$$r_{ik} = H_k s_{ik} e^{j\phi_i} + w_{ik} \tag{6.23}$$

where s_{ik}, r_{ik}, H_k and w_{ik} are the transmitted signal, received signal, channel distortion and AWGN, respectively. ϕ_i is the same for different subcarriers, defined as CPE. Assuming the channel distortion is removed first, we can simplify the model as an AWGN channel with unknown carrier phase noise: $r(k) = s(k)e^{j\phi} + w(k)$. The time subscript i for the investigated OFDM signal

is assumed to be fixed and thus omitted. $w(k)$ is a complex AWGN sequence with $E[|w(k)|^2] = N_0$. At the receiver, the LLR metric is calculated based on the received signal and passed to the iterative LDPC decoder, where the estimated message $\underline{\boldsymbol{m}}$ is obtained.

6.2.2 Derivation of LLR Metric

The information of the code bit c_k at subcarrier k is contained in the received signal $r(k)$. In our system, pilot subcarriers are employed for CPE estimation [1, 73]. Thus, the knowledge of CPE ϕ is contained in the received pilot subcarriers within the same symbol, i.e., $\{r(gB)\}_{g=0}^{L-1}$, g as the index number for pilots. To incorporate the pilot information into the LLR, we define it for $c(k)$ as:

$$\begin{aligned}\lambda(k) &= \ln \frac{p\Big(c_k = 0 \Big| r(k), \{r(gB)\}_{g=0}^{L-1}\Big)}{p\Big(c_k = 1 \Big| r(k), \{r(gB)\}_{g=0}^{L-1}\Big)} \\ &= \ln \frac{\sum_{l\in\mathbf{P}_+} p\Big(\alpha(k) = \frac{2\pi l}{M} \Big| r(k), \{r(gB)\}_{g=0}^{L-1}\Big)}{\sum_{l\in\mathbf{P}_-} p\Big(\alpha(k) = \frac{2\pi l}{M} \Big| r(k), \{r(gB)\}_{g=0}^{L-1}\Big)}\end{aligned} \tag{6.24}$$

where $\alpha(k) = \frac{2\pi l}{M}(l = 0, \cdots, M-1)$ is the modulated phase of k-th subcarrier, and $\mathbf{P}_+$ or $\mathbf{P}_-$ is the set of all possible l-values corresponding to $c_k = 0$ or 1, respectively. Because $\alpha(k)$ is independent of the pilots, i.e., $p(\alpha(k)|\{r(gB)\}_{g=0}^{L-1}) = p(\alpha(k))$ and $p(\alpha(k) = \frac{2\pi l}{M}) = \frac{1}{M}$,we can rewrite Eq. 6.24 as:

$$\lambda(k) = \ln \frac{\sum_{l\in\mathbf{P}_+} p\Big(r(k) \Big| \{r(gB)\}_{g=0}^{L-1}, \alpha(k) = \frac{2\pi l}{M}\Big)}{\sum_{l\in\mathbf{P}_-} p\Big(r(k) \Big| \{r(gB)\}_{g=0}^{L-1}, \alpha(k) = \frac{2\pi l}{M}\Big)} \tag{6.25}$$

Each likelihood function is evaluated by averaging over all possible values

of phase noise ϕ:

$$\begin{aligned} & p\Big(r(k)\Big|\alpha(k)=\tfrac{2\pi l}{M},\{r(gB)\}_{g=0}^{L-1}\Big) \\ &= \int_{-\pi}^{\pi} p\Big(r(k)\Big|\alpha(k)=\tfrac{2\pi l}{M},\phi,\{r(gB)\}_{g=0}^{L-1}\Big) \\ &\cdot p\Big(\phi\Big|\alpha(k)=\tfrac{2\pi l}{M},\{r(gB)\}_{g=0}^{L-1}\Big)d\phi \end{aligned} \tag{6.26}$$

Conditioned on $\alpha(k)=\frac{2\pi l}{M}$ and ϕ, the only randomness in $r(k)$ is due to $w(k)$, which is a Gaussian variable. Hence, we have:

$$\begin{aligned} & p\Big(r(k)\Big|\alpha(k)=\tfrac{2\pi l}{M},\phi,\{r(gB)\}_{g=0}^{L-1}\Big) \\ &= p\Big(r(k)\Big|\alpha(k)=\tfrac{2\pi l}{M},\phi\Big) \\ &= C(k)\exp\Big[\frac{2E_s^{\frac{1}{2}}}{N_0}|r(k)|\cos(\angle r(k)-\phi-\tfrac{2\pi l}{M})\Big] \end{aligned} \tag{6.27}$$

where $C(k)=\frac{1}{\pi N_0}\exp(-\frac{|r(k)|^2+E_s}{N0})$. Since CPE ϕ is independent of information phase $\alpha(k)$, we have:

$$p\Big(\phi\Big|\alpha(k)=\tfrac{2\pi l}{M},\{r(gB)\}_{g=0}^{L-1}\Big)=p\Big(\phi\Big|\{r(gB)\}_{g=0}^{L-1}\Big) \tag{6.28}$$

From [96], Eq. 6.28 can be derived as:

$$p\Big(\phi\Big|\{r(gB)\}_{g=0}^{L-1}\Big)=\frac{\exp\Big(\frac{2E_s^{\frac{1}{2}}}{N_0}|v|\cos(\phi-\angle v)\Big)}{2\pi I_0\Big(\frac{2E_s^{\frac{1}{2}}}{N_0}|v|\Big)} \tag{6.29}$$

where $I_0[|x|]=\frac{1}{2\pi}\int_{-\pi}^{\pi}\exp[|x|\cos\phi]d\phi$ is the zeroth-order modified Bessel function and $v=\sum_{g=0}^{L-1}r(gB)$, which is the reference phasor based on the re-

ceived pilot subcarriers. Now, substituting Eq. 6.27 and Eq. 6.29 into Eq. 6.26, we have:

$$\begin{aligned} & p\Big(r(k)\Big|\alpha(k)=\tfrac{2\pi l}{M},\{r(gB)\}_{g=0}^{L-1}\Big) \\ & = \frac{C(k)}{I_0\Big[\frac{2E_s^{\frac{1}{2}}}{N_0}|v|\Big]} I_0\Big[\frac{2E_s^{\frac{1}{2}}}{N_0}|v+e^{-j2\pi l/M}r(k)|\Big] \end{aligned} \tag{6.30}$$

Substituting Eq. 6.30 into Eq. 6.25, we obtain the pilot-aided LLR (PA-LLR) metric:

$$\lambda(k)=\ln\frac{\sum_{l\in\mathbf{P}_+} I_0\Big[\frac{2E_s^{\frac{1}{2}}}{N_0}|v+e^{-j2\pi l/M}r(k)|\Big]}{\sum_{l\in\mathbf{P}_-} I_0\Big[\frac{2E_s^{\frac{1}{2}}}{N_0}|v+e^{-j2\pi l/M}r(k)|\Big]} \tag{6.31}$$

For high SNR such that $E_s/N_0 >> 1$, $I_0(x)$ may be approximated as $e^x/\sqrt{2\pi x}$. After the approximation and removal of the $\ln(*)$ term, the metric becomes simplified-approximate LLR (PA-SA-LLR):

$$\lambda(k)\approx\frac{2E_s^{\frac{1}{2}}}{N_0}\Big[\max_{l\in\mathbf{P}_+}|v+e^{-j2\pi l/M}r(k)|-\max_{l\in\mathbf{P}_-}|v+e^{-j2\pi l/M}r(k)|\Big] \tag{6.32}$$

The calculation of PA-SA-LLR is much computationally simpler than the calculation of PA-LLR, with the modified Bessel function, which requires integration, and the ln() operation being removed.

6.2.3 Simulation Study

In the simulation, a half-rated, regular (204, 102) binary LDPC code [95] is used with IDFT/DFT size of 256 and data subcarriers of 204, resulting in an oversampling ratio of about 1.25. Both BPSK and QPSK modulations are em-

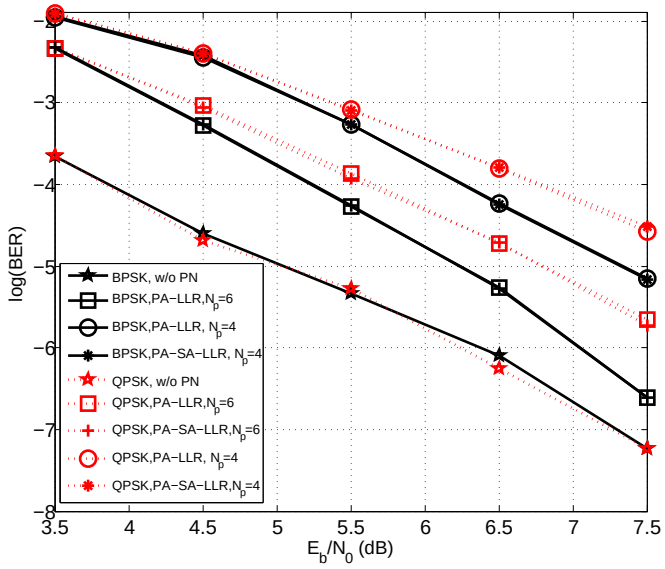

Figure 6.11: BER performance of (204,102) LDPC codes with phase noise (N_p=4 or 6, PA-LLR or PA-SA-LLR) and without phase noise for BPSK/QPSK.

ployed. The noise variance is assumed to be known at the receiver side.

In the first case, only CPE is considered, i.e., the phase noise ϕ is constant over different subcarriers, modeled as a random variable with uniform distribution in the interval $[-\pi, \pi)$. Fig. 6.11 shows the BER performance for PA-LLR and PA-SA-LLR with 4 or 6 pilot subcarriers against SNR per information bit, E_b/N_0, where E_b is the energy per information bit. The BER performance without phase noise is plotted for comparison. As the number of pilot subcarriers (N_p) increases, the performance with linear phase noise approaches the performance without linear phase noise. This is because the estimation of phase noise becomes more accurate given more pilot subcarriers. It is observed that both PA-LLR and PA-SA-LLR achieve almost same performance. In terms of computational complexity, PA-LLR (Eq. 6.31) involves an extra integration and

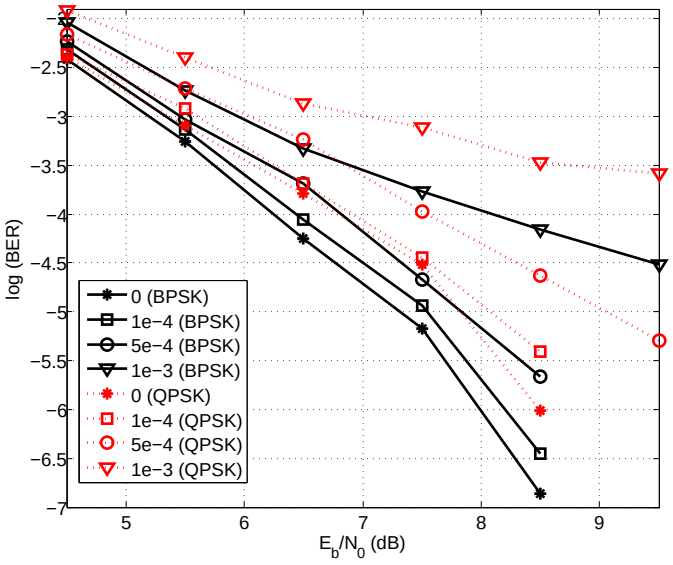

Figure 6.12: BER performance of (204,102) LDPC codes for different distribution of phase noise ($N_p = 4$, PA-SA-LLR) for BPSK/QPSK.

$\ln(*)$ term compared to PA-SA-LLR (Eq. 6.32) but they have the same performance. Thus the approximated version (PA-SA-LLR) would be a better alternative of PA-LLR. As expected, QPSK performs slightly worse than BPSK in the presence of linear phase noise.

In the second case, we model the linear phase noise as a zero-mean Gaussian process (the Wiener-Levy process) with a variance of $\sigma^2 = 2\pi vt$, where v is the combined laser linewidth and t is the time difference between two samples. In Fig. 6.12, we plot the BER curve with 4 pilots, σ^2 equal to 0, 10^{-4}, $5 \cdot 10^{-4}$ and 10^{-3} for PA-SA-LLR. PA-LLR is found to be performing almost the same as PA-SA-LLR and thus omitted. Now linear phase noise will introduce both CPE and ICI. When the variance (or laser linewidth) is small enough, the ICI part is negligible. Within a range of linear phase noise variance, e.g., $\sigma^2 < 5 \cdot 10^{-4}(10^{-4})$, which corresponds to $< 800(160)$ kHz for a 10-Gsample/s

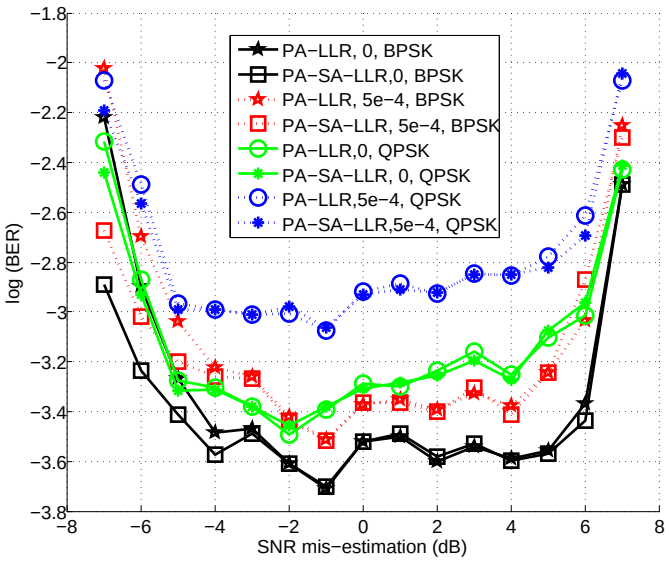

Figure 6.13: BER performance of (204,102) LDPC codes at $E_b/N_0 = 6$ dB, $\sigma^2 = 0$ or $5 \cdot 10^{-4}$, $N_p = 4$, subjected to SNR estimation error, for BPSK/QPSK.

BPSK/QPSK OFDM system, the BER performance only suffers small degradation from the ideal case. As the variance increases beyond $5 \cdot 10^{-4}$ for BPSK or 10^{-4} for QPSK, there is more severe degradation due to ICI. This is because BPSK is more tolerant to phase noise compared to QPSK, which is apparent from their constellation.

Fig. 6.13 shows the effect of an estimation error in SNR on the performance with σ^2 equal to 0 or $5 \cdot 10^{-4}$, at 6-dB SNR with 4 pilot subcarriers for BPSK and QPSK. Both metrics perform slightly better with 1-dB SNR underestimation. Both metrics are quite tolerant to SNR mis-estimation with up to 4-dB underestimation or overestimation. The calculation of LLR metric requires the knowledge of SNR. As shown in [97], with CO-OFDM, OSNR (SNR) can be estimated through receiver signal processing before decoding using the derived LLR metrics. Moreover, any estimation method with accuracy within

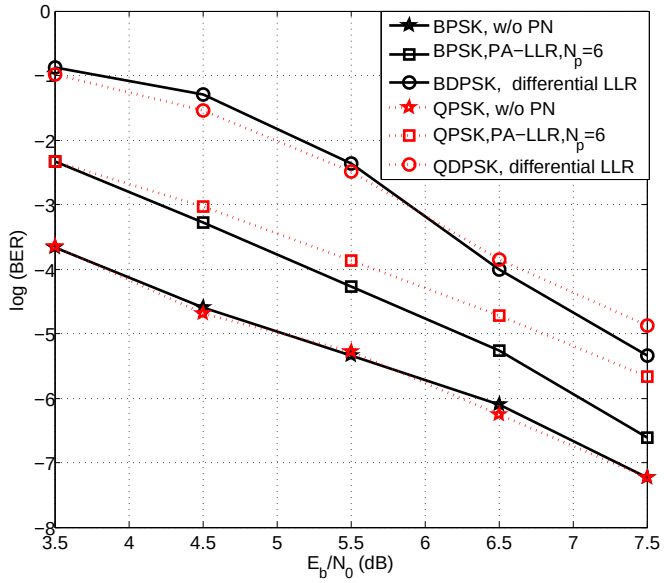

Figure 6.14: BER performance of (204,102) LDPC codes for different LLR metrics: PA-LLR ($N_p = 6$) for BPSK/QPSK and LLR for differential BPSK/QPSK.

± 4 dB would be sufficient. Fig. 6.14 compares the pilot-aided LLR metric (PA-LLR) with the differential metric derived in previous section. Coherent PA-LLR ($N_p = 6$) is performing better than differential LLR metric.

6.3 PA LLR for LDPC Coded M-QAM OFDM

In the presence of linear phase noise, pilot-assisted (PA) phase compensation is usually conducted first, followed by LDPC decoding using the conventional LLR [33–35]. In this section, we propose to incorporate the knowledge of phase noise into the calculation of bit LLR and derive it for M-QAM CO-OFDM system. The derived bit LLR, defined as pilot-aided LLR (PA-LLR), is evaluated from the likelihood function given the received signal that carries that bit and a set of pilot subcarriers as well as unknown linear phase noise.

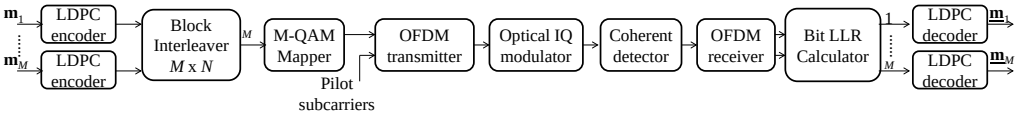

Figure 6.15: LDPC coded PA M-QAM CO-OFDM system model

6.3.1 Derivation of LLR Metric

The system model of LDPC coded PA M-QAM CO-OFDM system is shown in Fig. 6.15. The linear phase noise, which is a Wiener process, will introduce both common phase error (CPE) and inter-carrier interference (ICI). For deriving the PA-LLR, we assume that only CPE is considered and the channel distortion is already removed. The assumptions lead to a simplified model as: $r(k) = s(k)e^{j\phi} + w(k)$, where k is the frequency subscript while the time subscript is omitted. ϕ is the CPE and $w(k)$ is a complex AWGN sequence with $E[|w(k)|^2] = N_0$. Assume the symbols may equally take values from the set of $\{A_l\}_{l=0}^{M-1}$, which constitutes the M-QAM constellation. L equally spaced pilot subcarriers are employed for CPE estimation, with $\{s(gB)\}_{g=0}^{L-1}$ and $\{r(gB)\}_{g=0}^{L-1}$ representing transmitted and received pilot subcarriers, respectively. For simplicity, we set $s(gB) = E_s$ with E_s being the average signal power. The knowlege of CPE ϕ is contained in the received pilot subcarriers. Thus, the LLR metric is calculated from the information contained both in the received signal and the pilot subcarriers:

$$\begin{aligned}\lambda(k) &= \ln \frac{p\Big(c_k = 0 \Big| r(k), \{r(gB)\}_{g=0}^{L-1}\Big)}{p\Big(c_k = 1 \Big| r(k), \{r(gB)\}_{g=0}^{L-1}\Big)} \\ &= \ln \frac{\sum_{l\in\mathbf{P}_+} p\Big(s(k) = A_l \Big| r(k), \{r(gB)\}_{g=0}^{L-1}\Big)}{\sum_{l\in\mathbf{P}_-} p\Big(s(k) = A_l \Big| r(k), \{r(gB)\}_{g=0}^{L-1}\Big)}\end{aligned} \tag{6.33}$$

where $\mathbf{P}_+$ and $\mathbf{P}_-$ is the set of all possible A_l-values corresponding to $c_k = 0$ or 1, respectively. Because the transmitted signal $s(k)$ is independent of the pilots, i.e., $p(s(k)|\{r(gB)\}_{g=0}^{L-1}) = p(s(k))$ and $p(s(k) = A_l) = \frac{1}{M}$, we can rewrite Eq. 6.33 as:

$$\lambda(k) = \ln \frac{\sum_{l\in\mathbf{P}_+} p\Big(r(k)\Big|s(k) = A_l, \{r(gB)\}_{g=0}^{L-1}\Big)}{\sum_{l\in\mathbf{P}_-} p\Big(r(k)\Big|s(k) = A_l, \{r(gB)\}_{g=0}^{L-1}\Big)} \tag{6.34}$$

Each probability density function is evaluated by integrating over all possible values of phase noise ϕ:

$$\begin{aligned} & p\Big(r(k)\Big|s_k = A_l, \{r(gB)\}_{g=0}^{L-1}\Big) \\ = & \int_{-\pi}^{\pi} p\Big(r(k)\Big|s(k) = A_l, \phi, \{r(gB)\}_{g=0}^{L-1}\Big) \\ & \cdot p\Big(\phi\Big|s(k) = A_l, \{r(gB)\}_{g=0}^{L-1}\Big) d\phi \end{aligned} \tag{6.35}$$

Conditioned on $s(k) = A_l$ and ϕ, the only randomness in $r(k)$ is due to $w(k)$, which is a Gaussian random variable. Hence, we have:

$$\begin{aligned} & p\Big(r(k)\Big|s(k) = A_l, \phi, \{r(gB)\}_{g=0}^{L-1}\Big) \\ = & p\Big(r(k)\Big|s(k) = A_l, \phi\Big) \\ = & \frac{1}{\pi N_0} \exp\Big[-\frac{1}{N_0}|r(k) - A_l e^{j\phi}|^2\Big] \\ = & C_l \exp\Big[\frac{1}{N_0}(r^*(k)A_l e^{j\phi} + r(k)A_l^* e^{-j\phi})\Big] \end{aligned} \tag{6.36}$$

where

$$C_l = \frac{1}{\pi N_0} \exp\Big[-\frac{1}{N_0}(|r(k)|^2 + |A_l|^2)\Big] \tag{6.37}$$

The second probability term under the integration is calculated as follows:

$$\begin{aligned} & p\Big(\phi\Big|s(k)=A_l,\{r(gB)\}_{g=0}^{L-1}\Big) \\ = \; & p\Big(\phi\Big|\{r(gB)\}_{g=0}^{L-1}\Big) \\ = \; & \frac{p\Big(\{r(gB)\}_{g=0}^{L-1}\Big|\phi\Big)p(\phi)}{\int_{-\pi}^{\pi}p\Big(\{r(gB)\}_{g=0}^{L-1}\Big|\phi\Big)p(\phi)d\phi} \end{aligned} \tag{6.38}$$

where

$$\begin{aligned} & p\Big(\{r(gB)\}_{g=0}^{L-1}\Big|\phi\Big) \\ = \; & C_l'\exp\Big[\frac{1}{N_0}(\sum_{g=0}^{L-1}r^*(gB)s(gB)e^{j\phi}+r(gB)s^*(gB)e^{-j\phi})\Big] \end{aligned} \tag{6.39}$$

Incorporating Eq. 6.39 into Eq. 6.38, we obtain:

$$\begin{aligned} & p\Big(\phi\Big|\{r(gB)\}_{g=0}^{L-1}\Big) \\ = \; & \frac{\exp\Big[\frac{2}{N_0}|v|\cos(\phi-\angle v)\Big]}{2\pi I_0\Big[\frac{2}{N_0}|v|\Big]} \end{aligned} \tag{6.40}$$

where $I_0[|x|] = \frac{1}{2\pi}\int_{-\pi}^{\pi}\exp[|x|\cos\phi]d\phi$ is the zeroth-order modified Bessel function and $v = \sum_{g=0}^{L-1}r(gB)s^*(gB)$, which is the reference phasor based on the received pilot subcarriers. Now substituting Eq. 6.36 and Eq. 6.40 into

Eq. 6.35, we have

$$\begin{aligned} & p\Big(r(k)\Big|s_k = A_l, \{r(gB)\}_{g=0}^{L-1}\Big) \\ = & \frac{C_l I_0\Big[\frac{2}{N_0}|v + r(k)A_l^*|\Big]}{I_0\Big[\frac{2}{N_0}|v|\Big]} \end{aligned} \tag{6.41}$$

Finally, we obtain the PA-LLR for M-QAM system:

$$\begin{aligned} \lambda(k) &= \ln \frac{\sum_{l\in\mathbf{P}_+} C_l I_0\Big[\frac{2}{N_0}|v + r(k)A_l^*|\Big]}{\sum_{l\in\mathbf{P}_-} C_l I_0\Big[\frac{2}{N_0}|v + r(k)A_l^*|\Big]} \\ &= \ln \frac{\sum_{l\in\mathbf{P}_+} \exp(-\frac{1}{N_0}|A_l|^2) I_0\Big[\frac{2}{N_0}|v + r(k)A_l^*|\Big]}{\sum_{l\in\mathbf{P}_-} \exp(-\frac{1}{N_0}|A_l|^2) I_0\Big[\frac{2}{N_0}|v + r(k)A_l^*|\Big]} \end{aligned} \tag{6.42}$$

For high SNR such that $E_s/N_0 >> 1$, $I_0(x)$ may be approximated as $e^x/\sqrt{2\pi x}$. After the approximation and removal of the $\ln(*)$ term, the metric becomes simplified-approximate LLR (PA-SA-LLR):

$$\lambda(k) \approx \frac{1}{N_0}\Big[\max_{l\in\mathbf{P}_+}(2|v+r(k)A_l^*| - |A_l|^2) - \max_{l\in\mathbf{P}_-}(2|v+r(k)A_l^*| - |A_l|^2)\Big] \tag{6.43}$$

The calculation of PA-SA-LLR is much computationally simpler than the calculation of PA-LLR, with the modified Bessel function, which requires integration, and the ln() operation being removed. In the literature [33–35], pilot-assisted (PA) CPE compensation is usually employed first ($r'(k) = r(k)\exp(-j\hat{\phi})$, $\hat{\phi} = \angle\sum_{g=0}^{L-1} r(gB)s^*(gB)$), followed by LDPC decoding. The conventional LLR (C-LLR) metric without the consideration of phase noise is usually em-

ployed for LDPC decoder:

$$\lambda(k) = \ln \frac{\sum_{l \in \mathbf{P}_+} \exp\left[-\frac{1}{N_0} |r'(k) - A_l|^2 \right]}{\sum_{l \in \mathbf{P}_-} \exp\left[-\frac{1}{N_0} |r'(k) - A_l|^2 \right]} \tag{6.44}$$

Similarly, we could derive a simplified-approximate version of C-LLR (C-SA-LLR):

$$\lambda(k) \approx \frac{1}{N_0} \Big[\max_{l \in \mathbf{P}_+} (-|r'(k) - A_l|^2) - \max_{l \in \mathbf{P}_-} (-|r'(k) - A_l|^2) \Big] \tag{6.45}$$

Thus, the calculation of the new PA-SA-LLR (Eq. 6.43) has no higher computational complexity than compensation of phase noise followed by calculation of C-LLR (Eq. 6.45).

6.3.2 Simulation Study

In the simulation, a half-rated, regular (204,102) binary LDPC code [95] is used with IDFT/DFT size of 256 and data subcarriers of 204, resulting in an oversampling ratio of about 1.25. Different M-QAM modulation formats (M=4,16,64) with Gray coding are employed. The noise variance is assumed to be known at the receiver.

In the first case, only CPE is considered, i.e., the phase noise ϕ is assumed constant over different subcarriers, modeled as a random variable with uniform distribution in the interval $[-\pi, \pi)$. In Fig. 6.16, we plot the BER curves for PA-LLR and PA-SA-LLR with 4 or 6 pilot subcarriers. The coherent case without phase noise is shown as a reference. Additionally, we plot the baseline BER curve with PA CPE compensation followed by LDPC decoding using conven-

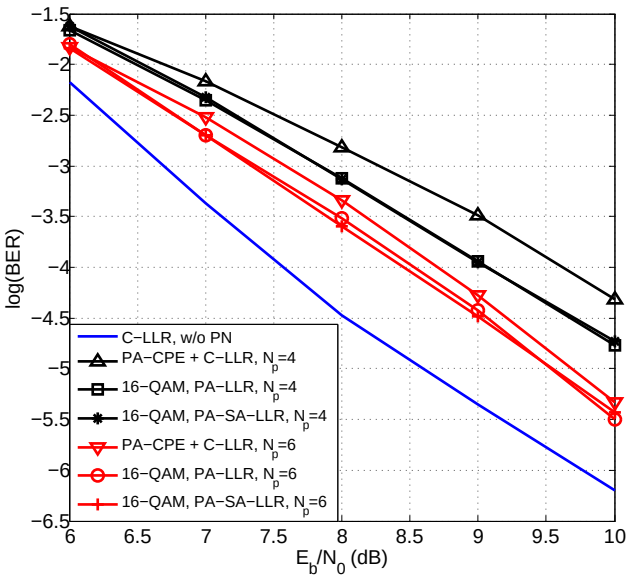

Figure 6.16: BER performance of (204,102) LDPC codes with phase noise (N_p=4 or 6, PA-LLR or PA-SA-LLR or C-LLR) and without phase noise for 16QAM.

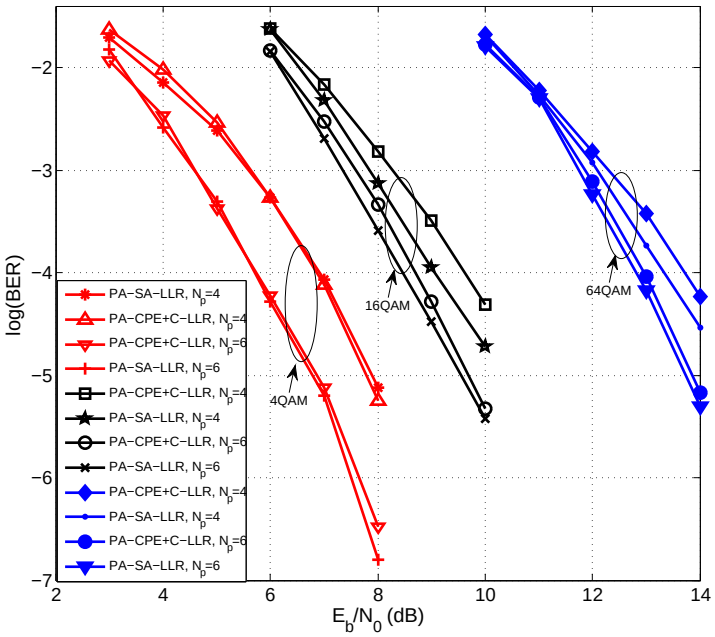

Figure 6.17: BER performance of (204,102) LDPC codes for different modulation formats: 4QAM, 16QAM and 64QAM.

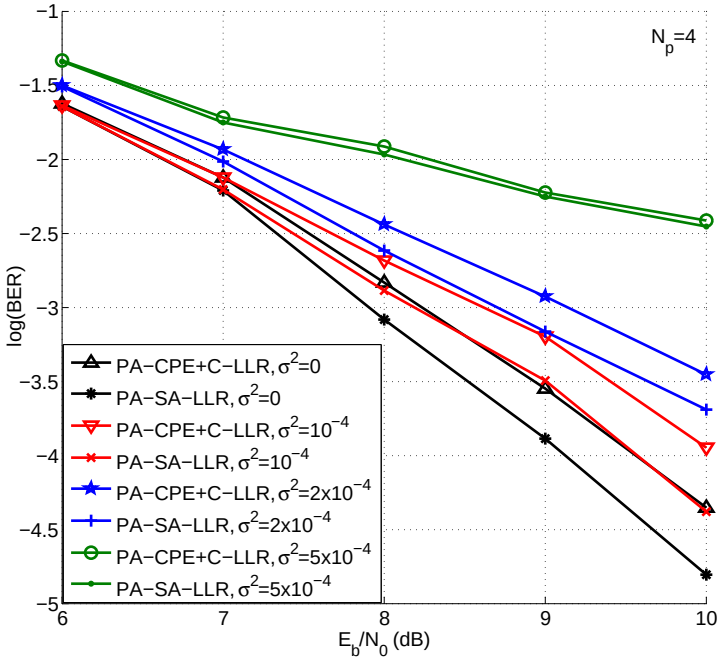

Figure 6.18: BER performance of (204,102) LDPC codes for different distribution of phase noise ($N_p = 4$, PA-LLR, PA-SA-LLR) for 16QAM

tional LLR metric. Our one-step LDPC decoding using PA-LLR (or PA-SA-LLR) is superior to the baseline method, especially for fewer pilot subcarriers. With more pilot subcarriers, the performance in the presence linear phase noise is closer to the coherent case. This is because more accurate knowledge of CPE is acquired given more pilot subcarriers. It is observed from the figure that PA-LLR and PA-SA-LLR achieve almost identical performance. In terms of computational complexity, PA-LLR involves an extra integration and $\ln(*)$ term compared to PA-SA-LLR. Thus the approximated version (PA-SA-LLR) would be a better alternative of PA-LLR. In the following simulation, the curve with PA-LLR is omitted for clarity. However, we have verified that PA-LLR and PA-SA-LLR perform almost the same in all the investigated cases. Fig. 6.17 compares LDPC coded CO-OFDM system with different M-QAM modulation

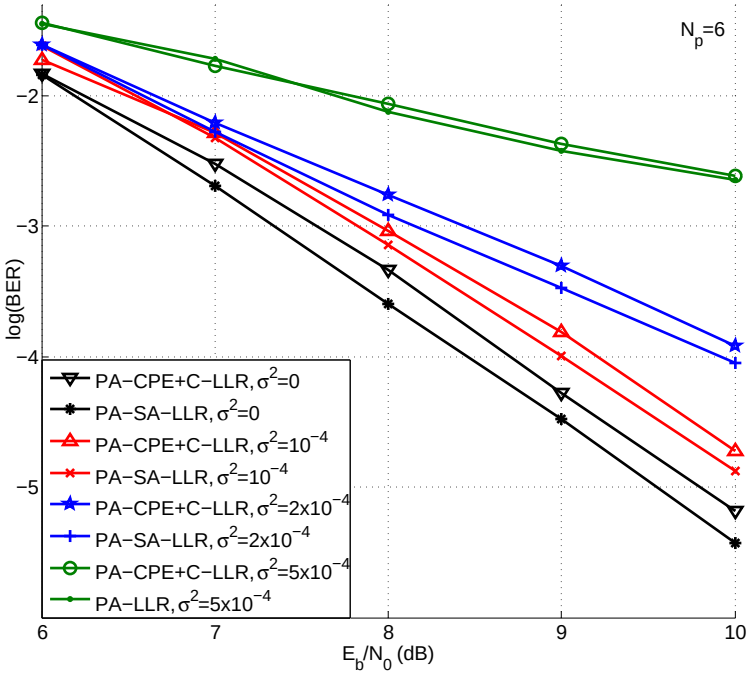

Figure 6.19: BER performance of (204,102) LDPC codes for different distribution of phase noise ($N_p = 6$, PA-LLR, PA-SA-LLR) for 16QAM

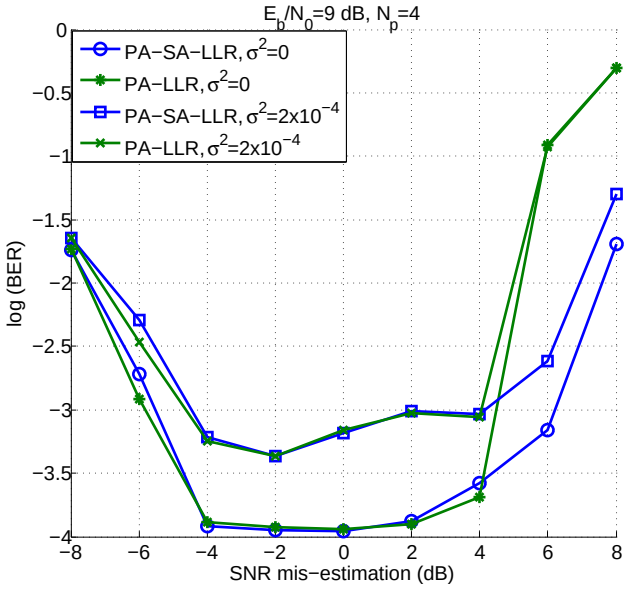

Figure 6.20: BER performance of (204,102) LDPC codes at $E_b/N_0 = 9$ dB, $\sigma^2 = 0$ or $2 \cdot 10^{-4}$, $N_p = 4$, subjected to SNR estimation error, for 16QAM.

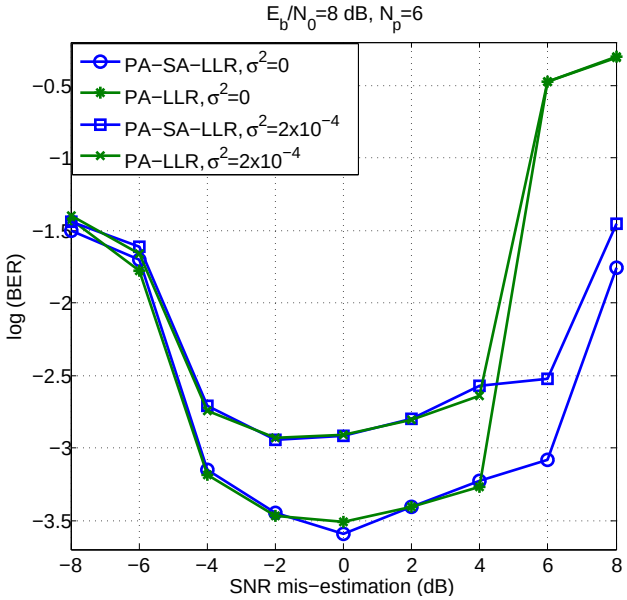

Figure 6.21: BER performance of (204,102) LDPC codes at $E_b/N_0 = 8$ dB, $\sigma^2 = 0$ or $2 \cdot 10^{-4}$, $N_p = 6$, subjected to SNR estimation error, for 16QAM.

formats (M=4,16,64). There is noticeable improvement of our LLR over the C-LLR for 16QAM and 64QAM format with the $N_p = 4$ case.

In the second case, we model the linear phase noise as a Wiener process, i.e., the difference between two phase noise time samples $\{\Delta\phi_n | \Delta\phi_n = \phi_{n+1} - \phi_n\}$ is a set of independent and identically distributed, zero-mean Gaussian random variables, each with variance of $\sigma^2 = 2\pi v \Delta t$. v is the combined laser linewidth and Δt is the time difference between two samples. In Fig. 6.18 and Fig. 6.19, we plot the BER curves with 4 or 6 pilot subcarriers and different σ^2 values (0, 10^{-4}, $2 \cdot 10^{-4}$ and $5 \cdot 10^{-4}$). When the variance is small enough, e.g., $\sigma^2 < 10^{-4}$, which corresponds to 160 kHz for a 10-Gsample/s system, the ICI part is negligible and the BER performance only suffers small degradation from the first case. The performance improvement of our LLR metric over the C-LLR vanishes for large variance ($5 \cdot 10^{-4}$).

Fig. 6.20 and Fig. 6.21 show the effect of SNR estimation error on the system performance with σ^2 equal to 0 or $2 \cdot 10^{-4}$, at 9-dB E_b/N_0 with 4 or 6 pilot subcarriers for 16QAM. Both metrics are quite tolerant to SNR mis-estimation with up to 4-dB underestimation or overestimation. The calculation of LLR metric requires the knowledge of SNR. As shown in [97], with CO-OFDM, OSNR (SNR) can be estimated through receiver signal processing before decoding using the derived LLR metrics. Moreover, any estimation method with accuracy within ± 4 dB would be sufficient.

In conclusion, we derive the PA-LLR metric with the consideration of linear phase noise for LDPC coded M-QAM CO-OFDM. The phase noise term is included into the decoding metric and thus the need for prior phase compensation is eliminated. Moreover, our PA-LLR performs better than the conventional LLR in 16QAM and 64QAM simulation. PA-SA-LLR is proposed as a simplification of PA-LLR, which achieves similar performance with much lower complexity.

6.4 Conclusion

In this chapter, we have derived the theoretical LLRs and their approximate versions with consideration of linear phase noise for LDPC coded OFDM systems for the first time. In section 6.1, we proposed an LLR metric based on two-symbol-interval observations with consideration of linear phase noise for LDPC coded BDPSK-OFDM. The LLR metric outperforms the GM metric, with larger tolerance to SNR under-estimation error. Yet, the new metric (A-LLR) has the same order of complexity as GM. The work is then extended to cover other

differential formats, the differential M-ary PSK formats such as DQPSK. In section 6.2 and section 6.3, we derived a PA-LLR metric and its approximation (PA-SA-LLR) based on the received signal as well as the pilot subcarriers with consideration of linear phase noise for LDPC coded M-ary PSK and M-QAM OFDM systems, respectively. The PA-SA-LLR achieves the same performance as PA-LLR with much lower complexity. With the help of the PA-LLR (or PA-SA-LLR), the phase noise term is included into the decoding metric and thus the need for prior phase compensation is eliminated. Notably, our proposed one-step decoding using PA-SA-LLR has no higher computational complexity than the two-step phase estimation plus LDPC decoding using C-LLR. Moreover, our PA-LLR (or PA-SA-LLR) performs better than the conventional LLR in 16QAM and 64QAM simulation.

LOG-LIKELIHOOD RATIO FOR LDPC CODED OFDM SYSTEM WITH LINEAR PHASE NOISE

Chapter 7

Conclusion and Future Work

This chapter concludes the thesis and suggests several directions for future work. Section 7.1 summarizes the technical contributions achieved in this thesis. Section 7.2 suggests some directions for future research.

7.1 Conclusion

7.1.1 Carrier Frequency Offset Compensation

The key challenge in FOC for CO-OFDM system is to estimate the CFO both accurately and efficiently with a full acquisition range. In Chapter 3, a novel frequency offset compensation method is introduced for CO-OFDM system. The method is composed of a correlation-based method for the fraction part estimation and a pilot-tone-assisted method for the integer part estimation. Our algorithm can achieve the widest estimation range which is determined by the signal spectrum allocation and receiver bandwidth, by inserting only one pilot tone at the center of the spectrum. The fraction part of the CFO is calculated

simultaneously with time synchronization, whereas the integer part of the CFO is estimated by counting the shifted positions of the pilot tone in the received spectrum. Only one training symbol is needed for CFO acquisition, without the need of exhaustive search or tuning of any parameters. The performance of our FOC method is experimentally demonstrated in a 22.24-Gb/s CO-OFDM system.

Furthermore, a comprehensive analysis is carried out to examine the performance of our FOC method in the presence of chromatic dispersion and linear phase noise. We have analytically derived the fraction part estimation accuracy in the presence of linear phase noise for various correlation-based methods, Schmidl, Moose and CP, among which CP estimator is the most robust to linear phase noise. Schmidl and Moose estimators are shown to be robust to CD while CP estimator is quite sensitive to CD. The estimation accuracy of our pilot-tone-assisted integer part estimation method is proved to be independent of carrier spacing, carrier frequency offset value and dispersion, dependent of DFT size, pilot to average signal power ratio, SNR and linear phase noise.

7.1.2 Linear Phase Noise Compensation

Uncompensated linear phase noise will cause common phase error (CPE) and intercarrier interference (ICI). In Chapter 4, a novel decision-aided algorithm is introduced to compensate for the common phase error caused by linear phase noise, and we further propose to combine decision-aided algorithm with pilot-aided as well as decision-feedback methods. DA estimates the phase noise of the current symbol based on the decisions from the previous symbol. DA+PA

is able to reduce the overhead of PA and it improves the phase noise tolerance of DA. DA+DF is demonstrated to be performing the best among all the phase estimation schemes with zero overhead in a simulated 40-Gb/s CO-OFDM system. We also analytically evaluate the BER performance when only CPE is compensated for. BER expression is derived under Gaussian approximation of ICI, which is quite close to the simulation result, especially for smaller laser linewidth.

A time-domain blind ICI mitigation algorithm was first proposed for constant amplitude modulation formats in wireless networks. Here, we propose new power estimation methods for this algorithm to adapt to non-constant amplitude modulation format in CO-OFDM system. The modified algorithm is demonstrated to be effective in mitigating ICI for a simulated 56-Gb/s CO-OFDM system over various non-constant amplitude modulation formats: 8-QAM, 16-QAM, 32-QAM and 64-QAM. Furthermore, it shows superior performance with the same complexity compared to the decision-aided ICI compensation algorithm at larger laser linewidths, especially for higher-order modulation format.

7.1.3 IQ mismatch Compensation

In Chapter 5, we investigate the system model with carrier frequency offset, linear phase noise, Tx and Rx IQ mismatch and channel distortion. Based on the model, the correct order of compensation should be: (1) Rx IQ mismatch compensation (GSOP), (2) frequency offset compensation, (3) Tx IQ mismatch and channel distortion compensation.

A decision-aided joint compensation method for Tx IQ mismatch and chan-

nel distortion is successfully introduced. Our method is superior to the previous methods in several aspects. Firstly, DAJC makes use of standard pilot symbols, which simplifies the design compared to the special pilot structure proposed in [36]. Secondly, the adaptive characteristic of DAJC makes it more robust to time-variant channel and imbalance parameters, and also reduces the requirement on overhead. Last but not least, DAJC performs better than both GSOP and PA, with tolerable and adjustable increase in complexity.

In addition to DAJC, we propose to employ a second stage to compensate the linear phase noise. Simulation results show that our proposed algorithm can effectively mitigate Tx IQ mismatch, channel distortion and linear phase noise at the same time.

Lastly, we propose to use pre-distortion scheme for compensating IQ mismatch and compare it with the post-equalization scheme through simulation. PE is performing better than PD for smaller phase or amplitude mismatch values while PD has larger tolerance towards the mismatch.

7.1.4 Log-likelihood Ratio for LDPC Coded OFDM System with Linear Phase Noise

The performance of decoding algorithms depends on the calculation of the decoding metric, i.e., the log-likelihood ratio. In Chapter 6, a new log-likelihood ratio with the linear phase noise term is analytically derived for CO-OFDM system with different modulation formats: differential MPSK, pilot-aided MPSK and pilot-aided M-QAM. As far as we know, this is the first work which gives analytical LLR expressions for LDPC coded CO-OFDM system with the con-

sideration of linear phase noise.

We first proposed a new LLR metric and its simplied version (A-LLR) based on two-symbol-interval observations with consideration of linear phase noise for LDPC coded BDPSK-OFDM. Our LLR metric is performing slightly better compared to GM metric, with larger tolerance to SNR under-estimation error. A-LLR metric has almost identical performance compared to the LLR metric but with much lower computational complexity. The work is then extended to cover other differential formats, the differential M-ary PSK formats such as DQPSK.

Furthermore, we derived a PA-LLR metric based on the received signal as well as the pilot subcarriers with consideration of linear phase noise for LDPC coded M-ary PSK and M-QAM OFDM systems. With the help of the PA-LLR, the phase noise term is included into the decoding metric and thus the need for prior phase compensation is eliminated. Moreover, our PA-LLR performs better than the conventional LLR in 16QAM and 64QAM simulation. The PA-SA-LLR is proposed as a simplification of PA-LLR, which achieves similar performance with much lower complexity.

7.1.5 Discussion

Fig. 7.1 shows the complete diagram of all the proposed DSP algorithms for combatting front-end non-idealities in CO-OFDM system. At the receiver side, window synchronization and carrier frequency offset compensation (no.1) is done first, followed by an optional time domain ICI mitigation (no.2.2), then channel equalization is performed, including channel distortion (CD/PMD) and

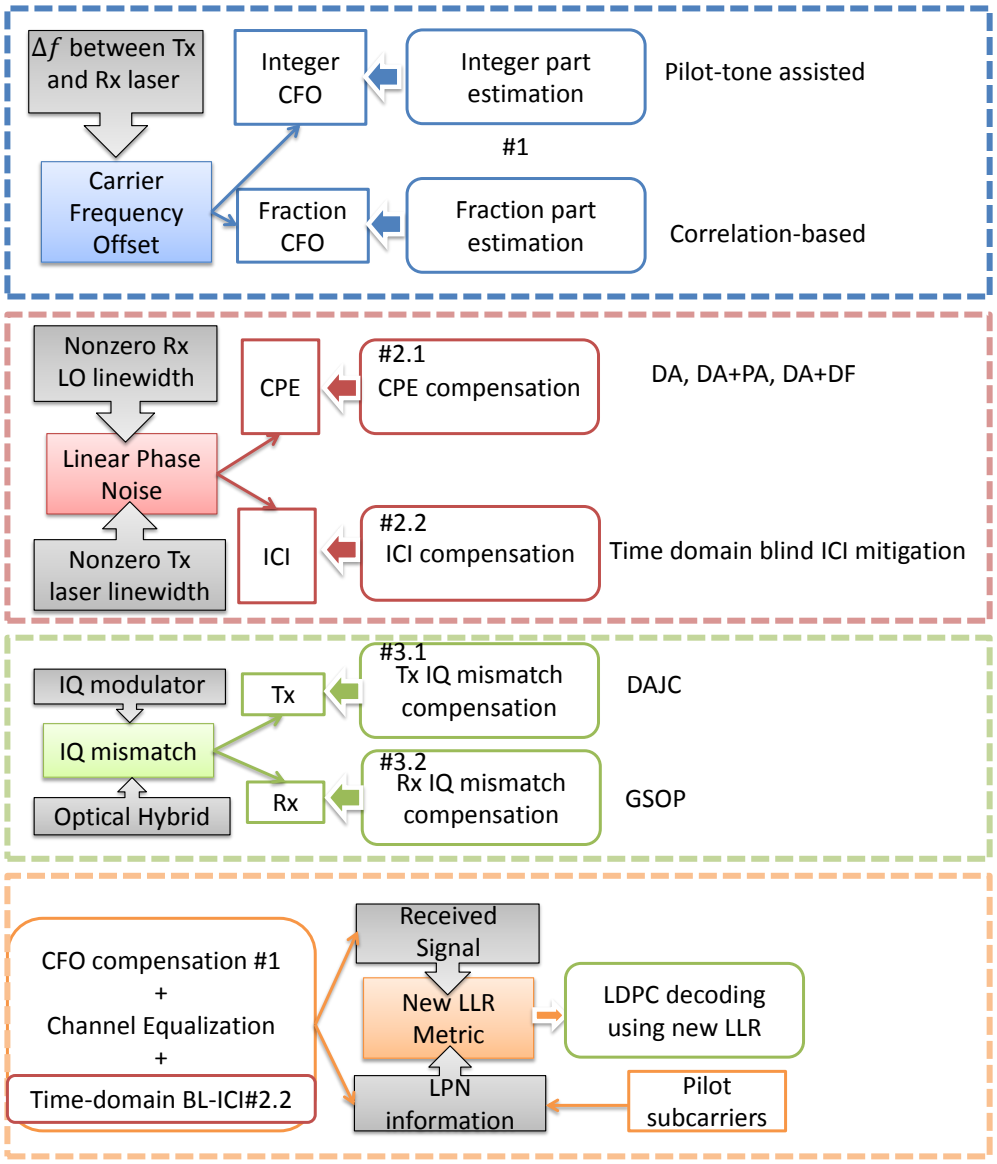

Figure 7.1: Diagram of all the proposed DSP for combatting front-end non-idealities

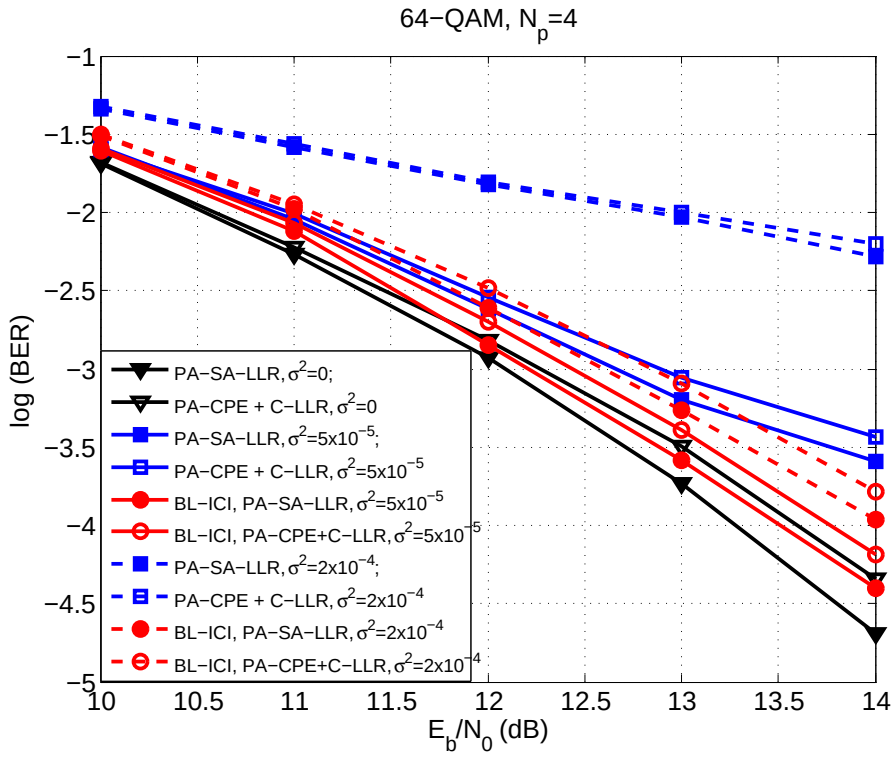

Figure 7.2: BER of LDPC coded 64QAM-CO-OFDM with different phase noise variance and 4 pilot subcarriers, with or without time-domain ICI mitigation

Tx IQ mismatch compensation (no.3.2), and finally CPE compensation (no.2.1) is carried out. For an LDPC coded OFDM system, we need to perform LDPC decoding as our last step. When we employ our newly derived LLR for LDPC decoders, the final stage of CPE compensation is eliminated. The CPE compensation stage is combined into the calculation of the new LLR metric. We derived our new LLR metric based on the assumption of no ICI. Thus, its performance will be degraded if ICI is too large, usually in the case of large laser linewidth, long OFDM symbol duration and high-order modulation formats. To solve this problem, we can employ our time-domain ICI mitigation method prior to LDPC decoding. Fig. 7.2 shows one of the examples of combining the time-doamin ICI mitigation method and LDPC decoding using PA-SA-LLR metric. We can observe large performance gain when the two methods are combined as compared to LDPC decoding only.

7.2 Future Work

7.2.1 Nonlinear Phase Noise

Besides linear phase noise, nonlinear phase noise is another key performance-limiting factor in CO-OFDM system. The large peak-to-average power ratio of OFDM signals leads to large system nonlinearity. Nonlinear phase noise is caused by the interaction of amplified spontaneous emission (ASE) noise with fiber nonlinearity such as self-phase modulation, cross-phase modulation and four-wave mixing. We have conducted some preliminary research on nonlinear phase noise compensation in our paper [98]. In this work, we show that

the one-step nonlinearity compensation method, i.e., nonlinear phase rotation, is affected by the amount of pre-compensated dispersion for CO-OFDM system with a dispersion unmanaged link. It is observed that NPR plus optimal percentage, around 50%, of dispersion pre-compensation is performing better than 1-step digital back-propagation (BP), with the same computational complexity. The optimized scheme results in a 2-dB improvement in optimal launch power as well as 1.75-dB improvement in optimal signal quality compared to 1-step BP after 800-km transmission at the bit rate of 20 Gb/s. However, the performance gain becomes more limited as the data rate increases to 40 Gb/s. In our work, we only consider chromatic dispersion and assumes no polarization mode dispersion. In the future, we would like to do more research on nonlinear phase noise compensation in CO-OFDM system.

7.2.2 LDPC Coded OFDM

In our thesis, the bit LLR for MPSK and M-QAM format is calculated directly and passed to the LDPC decoder. However, in the literature [99], iterative demapping and decoding is conducted. The symbol LLRs are calculated in the a posteriori probability (APP) demapper. Then the bit LLRs are determined from the symbol LLRs and passed to the LDPC decoder. The iteration between the APP demapper and the LDPC decoder is performed until the maximum number of iterations is reached or the valid code words are obtained. We would like to apply our LLR metric with linear phase noise term to this iterative demapping and decoding scheme. Moreover, we would like to investigate on non-binary LDPC codes for CO-OFDM system.

References

[1] X. Yi, W. Shieh, and Y. Tang, "Phase Estimation for cohrent optical OFDM," *Photon. Technol. Lett.*, vol. 19, no. 12, pp. 919–921, 2007.

[2] I. Fatadin, S. J. Savory, and D. Ives, "Compensation of quadrature imbalance in an optical QPSK coherent receiver," *IEEE Photon. Technol. Lett.*, vol. 20, no. 20, pp. 1733–1735, 2008.

[3] S. C. H. Chung and K. Kim, "Effect of IQ mismatch compensation in an optical coherent OFDM receiver," *Photon. Technol. Lett.*, vol. 22, no. 5, pp. 308–310, 2010.

[4] Z. Wang and G. Giannakis, "Wireless multicarrier communications," *IEEE Signal Processing Mag.*, vol. 17, pp. 29–48, 2000.

[5] J. A. C. Bingham, *ADSL, VDSL, and multicarrier modulation*. New York: John Wiley and Sons, 2000.

[6] W. Shieh and C. Athaudage, "Coherent optical orthogonal frequency division multiplexing," *Electron Lett*, vol. 42, pp. 587–589, 2006.

[7] W. Shieh, H. Bao, and Y. Tang, "Coherent optical OFDM: theory and design," *Opt Express*, vol. 16, pp. 841–859, 2008.

[8] A. Lowery, L. Du, and J. Armstrong, "Orthogonal frequency division multiplexing for adaptive dispersion compensation in long haul WDM systems," in *Proc. Opt. Fiber Commun. Conf.*, 2006.

[9] I. Djordjevic and B. Vasic, "Orthogonal frequency division multiplexing for high-speed optical transmission," *Opt Express*, vol. 14, pp. 3767–3775, 2006.

[10] B. Schmidt, A. Lowery, and J. Armstrong, "Experimental demonstrations of electronic dispersion compensation for long-haul transmission using direct-detection optical OFDM," *J. Lightw. Technol.*, vol. 26, pp. 196–203, 2008.

[11] S. Jansen, B. Spinnler, I. Morita, S. Randel, and H. Tanaka, "100GbE: QPSK versus OFDM," *Optical Fiber Technol.*, vol. 15, pp. 407–413, 2009.

[12] G. Raybon and P. Winzer, "100 Gb/s challenges and solutions," in *Proc. Opt. Fiber Commun. Conf.*, 2008.

[13] M. Duelk, "Next generation 100 G Ethernet," in *in 34th European Conference on Optical Communication*, 2005.

[14] W. Shieh, Q. Yang, and Y. Ma, "107 Gb/s coherent optical OFDM transmission over 1000-km SSMF fiber using orthogonal band multiplexing," *Opt Express*, vol. 16, pp. 6378–6386, 2008.

[15] T. Hobayash, A. Sano, and E. Yamada, "Electro-optically subcarrier multiplexed 110 Gb/s OFDM signal transmission over 80 km SMF without dispersion compensation," *Electron Lett*, vol. 44, pp. 225–226, 2008.

[16] S. Jansen, I. Morita, and H. Tanaka, "10 x 121.9-Gb/s PDM-OFDM transmission with 2-b/s/Hz spectral efficiency over 1000 km of SSMF," in *Proc. Opt. Fiber Commun. Conf.*, 2008.

[17] X. Yi and et al., "Tb/s coherent optical OFDM systems enabled by optical frequency combs," *J. Lightw. Technol.*, vol. 28, no. 14, pp. 2054–2061, 2010.

[18] D. Hillerkuss and et al., "Single source optical OFDM transmitter and optical FFT receiver demonstrated at line rates of 5.4 and 10.8 Tbit/s," in *Proc. Opt. Fiber Commun. Conf.*, 2010.

[19] Y. Ma and et al., "1-Tb/s single-channel coherent optical OFDM transmission with orthogonal-band multiplexing and subwavelength bandwidth access," *J. Lightw. Technol.*, vol. 28, no. 4, pp. 308–315, 2010.

[20] D. Hillerkuss and et al., "Generation, transmission and coherent detection of 11.2 Tb/s (112x100Gb/s) single source optical OFDM superchannel," in *Proc. Opt. Fiber Commun. Conf.*, 2011.

[21] W. Shieh and I. Djordjevic, *OFDM for optical communications*, 1st ed. Academic Press, 2009.

[22] S. Han and J. Lee, "An overview of peak-to-average power ratio reduction techniques for multicarrier transmission," *IEEE Wireless Commun.*, vol. 12, pp. 56–65, 2005.

[23] X. Liu, F. Buchali, R. Tkach, and S. Chandrasekhar, "Mitigation of fiber nonlinear impairments in polarization division multiplexed OFDM transmission," *Bell Labs Tech. J.*, vol. 14, pp. 47–59, 2010.

[24] A. Barbieri and et al, "OFDM vs. single-carrier transmission for 100 Gbps optical communication," *J. Lightw. Technol.*, vol. 28, no. 17, pp. 2537–2551, 2010.

[25] G. Colavolpe, T. Foggi, E. Forestieri, and G. Prati, "Robust multilevel coherent optical systems with linear processing at the receiver," *J. Lightw. Technol.*, vol. 27, pp. 2357–2369, 2009.

[26] *ETSI Standard TR 102 376 V1.1.1: Digital Video Broadcasting (DVB) User Guidelines for the Second Generation System for Broadcasting, Interactive Services, News Gathering and Other Broadband Satellite Applications (DVB-S2)*. ETSI Std. TR 102 376, 2005.

[27] A. Morello and V. Mignone, "DVB-S2: The second generation standard for satellite broadband services," *Proc. IEEE*, vol. 94, pp. 210–227, 2006.

[28] *IEEE Standard for Information Technology-Telecommunications and Information Exchange Between Systems-Local and Metropolitan Area Networks-Specific Requirements Part 3: Carrier Sense Multiple Access With Collision Detection (CSMA/CD) Access Method and Physical Layer Specifications*. IEEE Std. 802.3an, 2006.

[29] *IEEE Standard for Local and Metropolitan Area Networks Part 16: Air Interface for Fixed and Mobile Broadband Wireless Access Systems Amendment 2: Physical and Medium Access Control Layers for Combined Fixed*

and Mobile Operation in Licensed Bands and Corrigendum 1. IEEE Std. 802.16e, 2006.

[30] *IEEE Draft Standard for Information Technology-Telecommunications and information Exchange Between Systems-Local and Metropolitan Area Networks-Specific Requirements-Part 11: Wireless LAN Medium Access Control (MAC) and Physical Layer (PHY) Specifications: Amendment : Enhancements for Higher Throughput*. IEEE Std. 802.11n/D2.00, 2007.

[31] K. S. Andrews, D. Divsalar, S. Dolinar, J. Hamkins, C. R. Jones, and F. Pollara, "The development of turbo and LDPC codes for deep-space applications," *Proc. IEEE*, vol. 95, pp. 2142–2156, 2007.

[32] A. Kavcic and A. Patapoutian, "The read channel," *Proc. IEEE*, vol. 96, pp. 1761–1774, 2008.

[33] I. B. Djordjevic and B. Vasic, "LDPC-coded OFDM in fiber-optics communication systems," *J. Opt. Netw.*, vol. 7, no. 3, pp. 217–226, 2008.

[34] Q. Yang, Z. He, W. Liu, Z. Yang, S. Yu, W. Shieh, and I. Djordjevic, "1-Tb/s large girth LDPC-coded coherent optical OFDM transmission over 1040-km standard single-mode fiber," in *Proc. OFC*, 2011.

[35] S. Zhang and et al, "40*117.6 Gb/s PDM-16QAM OFDM transmission over 10,181 km with soft-decision LDPC coding and nonlinearity compensation," in *Proc. OFC*, 2012.

[36] W. Chung, "Transmitter IQ mismatch compensation in coherent optical OFDM systems using pilot signals," *Photon. Technol. Lett.*, vol. 1, no. 20, pp. 21 308–21 314, 2010.

[37] M. Kuschnerov, F. Hauske, K. Piyawanno, B. Spinnler, M. Alfiad, A. Napoli, and B. Lankl, "DSP for coherent single-carrier receivers," *Journal of lightwave technology*, vol. 27, no. 16, pp. 3614–3622, 2009.

[38] S. L. Jansen, I. Morita, and H. Tanaka, "Narrowband filtering tolerance and spectral efficiency of 100GbE PDM-OFDM," in *IEEE/LEOS Summer Topical Meetings*, 2008, pp. 247–248.

[39] S. Weinsten and P. Ebert, "Data transmission by frequency-division multiplexing using the discrete Fourier transform," *IEEE Trans. Commun.*, vol. 19, no. 5, pp. 628–634, 1971.

[40] W. Shieh, X. Yi, and Q. Yang, "Coherent optical OFDM: has its time come?" *J. Opt. Networking*, vol. 7, no. 3, pp. 234–255, 2008.

[41] S. Jansen, I. Morita, T. Schenk, N. Takeda, and H. Tanaka, "Long-haul transmission of 16x52.5-Gb/s polarization division multiplexed OFDM enabled by MIMO processing," *OSA Journal of Optical Networking*, vol. 7, pp. 173–182, 2008.

[42] S. Hara and R. Prasad, *Multicarrier Techniques for 4G Mobile Communications*. Boston: Artech House, 2003.

[43] L. Hanzo, M. Munster, B. Choi, and T. Keller, *OFDM and MC-CDMA for Broadband Multi-user Communications, WLANs and Broadcasting*. New York: Wiley, 2003.

[44] P. H. Moose, "A technique for orthogonal frequency division multiplexing frequency offset correction," *IEEE Trans. Commun.*, vol. 42, no. 10, pp. 2908 – 2914, 1994.

[45] S. Chang, H. Chung, and K. Kim, "Impact of Quadrature Imbalance in Optical Coherent QPSK Receiver," *IEEE Photon. Technol. Lett.*, vol. 21, no. 11, pp. 709–711.

[46] T. Mizuochi and et al, "Forward error correction based on block turbo code with 3-bit soft decision for 10Gb/s optical communication systems," *IEEE J. Selected Topics Quantum Electronics*, vol. 10, no. 2, pp. 376–386, 2004.

[47] R. Pyndiah, "Near optimum decoding of product codes," *IEEE Trans. Commun.*, vol. 46, no. 8, pp. 1003–1010, 1998.

[48] O. Sab and V. Lemarie, "Block turbo code performances for long-haul DWDM optical transmission systems," in *Proc. Opt. Fiber Commun. Conf.*, vol. 3, 2001, pp. 280–282.

[49] S. Chung, J. G. Forney, T. Richardson, and R. Urbanke, "On the design of low-density parity-check codes within 0.0045 dB of the Shannon limit," *IEEE Comm. Lett.*, vol. 5, no. 2, pp. 58–60, 2001.

[50] I. B. Djordjevic, O. Milenkovic, and B. Vasic, "Generalized low-density parity-check codes for optical communication systems," *J. Lightwave Technol.*, vol. 23, no. 5, pp. 1939–1946, 2005.

[51] B. Vasic, I. B. Djordjevic, and R. Kostuk, "Low-density parity check codes and iterative decoding for long haul optical communication systems," *J. Lightwave Technol.*, vol. 21, no. 2, pp. 438–446, 2003.

[52] R. Gallager, *Low-density Parity-check Codes*. Cambridge MA: MIT Press, 1963.

[53] R. M. Neal. Sparse Matrix Methods and Probabilistic Inference Algorithm. [Online]. Available: http://www.cs.utoronto.ca/~radford/

[54] R. G. Gallager, "Low-density parity-check code," *IRE Trans. Inform. Theory*, vol. 8, no. 1, pp. 21–28, 1962.

[55] D. MacKay, "Good error-correcting codes based on very sparse matrices," *IEEE Trans. Inform. Theory*, vol. 45, no. 2, pp. 399–431, 1999.

[56] L. Ping and W. Leung, "Decoding low density parity check codes with finite quantization bits," *IEEE Commun. Lett.*, vol. 4, no. 2, pp. 62–64, 2000.

[57] T. Moon, *Error Correction Coding: Mathematical Methods and Algorithms*. New York: John Wiley and Sons, 2005.

[58] M. Fossorier, M. Mihaljevic, and H. Imai, "Reduced complexity iterative decoding of low density parity check codes based on belief propagation," *IEEE Trans. Commun.*, vol. 47, no. 5, pp. 673–680, 1999.

[59] E. Eleftheriou, T. Mittelholzer, and A. Dholakia, "Reduced-complexity decoding algorithm for low-density parity-check codes," *IEEE Electronics Lett.*, vol. 37, no. 2, pp. 102–104, 2001.

[60] X. Hu, E. Eleftheriou, D. Arnold, and A. Dholakia, "Efficient implementations of the sum-product algorithm for decoding of LDPC codes," in *Proc. IEEE Globecom*, vol. 2, 2001, pp. 1036–1036E.

[61] X. Liu and F. Buchali, "Intra-symbol frequency-domain averaging based channel estimation for coherent optical OFDM," *Optics Express*, vol. 16, no. 26, pp. 21 944–21 957.

[62] S. Fan, J. Yu, D. Qian, and G. Chang, "A fast and efficient frequency offset correction technique for coherent optical orthogonal frequency division multiplexing," *J. Lightw. Technol.*, vol. 29, no. 13, pp. 1997–2004, 2011.

[63] T. Pollet, M. V. Bladel, and M. Moeneclaey, "BER sensitivity of ofdm systems to carrier frequency and Wiener phase noise," *IEEE Trans. on Comm.*, vol. 43, no. 234, pp. 191–193, 1995.

[64] M. Moreli and U. Mengali, "An improved frequency offset estimator for OFDM applications," *IEEE Commun. Lett.*, vol. 3, no. 3, pp. 75–77, 1999.

[65] Z. Zhang, W. Jiang, H. Zhou, Y. Liu, and J. Gao, "High accuracy frequency offset correction with adjustable acquisition range in OFDM systems," *IEEE Trans. Wireless Commun.*, vol. 4, no. 1, pp. 228–237, 2005.

[66] F. Buchali, R. Dischler, M. Mayrock, X. Xiao, and Y. Tang, "Improved frequency offset correction in coherent optical OFDM systems," in *in 34th European Conference on Optical Communication*, 2008.

[67] T. M. Schmidl and D. C. Cox, "Robust frequency and timing synchronization for OFDM," *IEEE Trans. Commun.*, vol. 45, no. 12, pp. 1613 – 1621, 1997.

[68] Z. Zhang, M. Zhao, H. Zhou, Y. Liu, and J. Gao, "Frequency offset estimation with fast acquisition in OFDM systems," *IEEE Commun. Lett.*, vol. 8, no. 3, pp. 171–173, 2004.

[69] G. Ren, Y. Chang, H. Zhang, and H. Zhang, "An efficient frequency offset estimation method with a large range for wireless OFDM systems," *IEEE Trans. Vehic. Technol.*, vol. 56, no. 4, pp. 1892–1895, 2007.

[70] S. Jansen, I. Morita, T. Schenk, N. Takeda, and H. Tanaka, "Coherent Optical 25.8-Gb/s OFDM Transmission over 4,160-km SSMF," *J. Lightw. Technol.*, vol. 26, no. 1, pp. 6–15, 2008.

[71] R. No'e, "PLL-free synchronous QPSK polarization multiplex/diversity receiver concept with digital I & Q baseband processing," *IEEE Photon. Technol. Lett.*, vol. 17, no. 4, pp. 887–889, 2005.

[72] T. Pfau, S. Hoffmann, and et al., "First real-time data recovery for synchronous QPSK transmission with standard DFB lasers," *IEEE Photon. Technol. Lett.*, vol. 18, no. 9, pp. 1907–1909, 2006.

[73] W. Shieh, "Maximum-likelihood phase estimation and channel estimation for coherent optical OFDM," *IEEE Photon. Technol. Lett.*, vol. 20, no. 8, pp. 605–607, 2008.

[74] S. Jansen, I. Morita, N. Takeda, and H. Tanaka, "20-Gb/s OFDM transmission over 4160-km SSMF enabled by RF-pilot tone phase noise compensation," in *Proc. OFC*, 2007.

[75] S. Randel, S. Adhikari, and S. Jansen, "Analysis of RF-pilot-based phase noise compensation for coherent optical OFDM systems," *IEEE Photon. Technol. Lett.*, vol. 22, no. 17, pp. 1288–1290, 2010.

[76] M. E. Mousa-Pasandi and D. V. Plant, "Data-aided adaptive weighted channel equalizer for coherent optical OFDM," *Opt. Express*, vol. 18, no. 4, pp. 3919–3927, 2010.

[77] M. E. Mousa-Pasadi and D. V. Plant, "Zero-overhead phase noise compensation via decision-directed phase equalizer for coherent optical OFDM," *Opt. Express*, vol. 18, no. 20, pp. 20 651–20 660, 2010.

[78] S. Zhang, P. Kam, J. Chen, and C. Yu, "Decision-aided maximum likelihood detection in coherent optical phase-shift-keying system," *Opt. Express*, vol. 17, no. 2, pp. 703–715, 2009.

[79] S. Zhang, P. Kam, C. Yu, and J. Chen, "Decision-aided carrier phase estimation for coherent optical communications," *J. Lightw. Technol.*, vol. 28, no. 11, pp. 1597–1607, 2010.

[80] M. Lee, S. Lim, and K. Yang, "Blind compensation for phase noise in OFDM systems over constant modulus modulation," *IEEE Trans. on Comm.*, vol. 60, no. 3, pp. 620–625, 2012.

[81] D. Petrovic, W. Rave, and G. Fettweis, "Phase noise suppression in OFDM including intercarrier interference," in *Proc. Intl. OFDM Workshop (InOWo)*, 2003.

[82] D.Petrovic, W.Rave and G.Fettweis, "Intercarrier interference due to phase noise in OFDM - estimation and suppression," in *Proc. VTC*, 2004.

[83] C. Yang, F. Yang, and Z. Wang, "Orthogonal basis expansion-based phase noise estimation and suppression for CO-OFDM systems," *IEEE Photon. Technol. Lett.*, vol. 22, no. 1, pp. 51–53, 2010.

[84] C. Zhao and et al., "A CO-OFDM system with almost blind phase noise suppression," *IEEE Photon. Technol. Lett.*, vol. 25, no. 17, pp. 1723–1726, 2013.

[85] C. Lin, C. Wei, and M. Chao, "Phase noise suppression of optical OFDM signals in 60-GHz RoF transmission system," *Opt. Express*, vol. 29, no. 11, pp. 10 423–10 428, 2011.

[86] W. Chung, "A matched filtering approach for phase noise suppression in CO-OFDM systems," *IEEE Photon. Technol. Lett.*, vol. 22, no. 24, pp. 1802–1804, 2010.

[87] I. Djordjevic, L. Xu, and T. Wang, "Beyond 100 Gb/s optical transmission based on polarization multiplexed coded-OFDM with coherent detection," *J. Opt. Commun. Netw.*, vol. 1, no. 1, pp. 50–56, 2009.

[88] O. I. Forum, "Integrable tunable transmitter assembly multi source agreement," *OIF-ITTA-MSA-01.0*, 2008.

[89] S. Zhang, L. Xu, J. Yu, M.-F. Huang, P. Kam, C. Yu, and T. Wang, "Dual-stage cascaded frequency offset estimation for digital coherent receivers," *Photon. Technol. Lett.*, vol. 22, no. 6, pp. 401–403, 2010.

[90] J.-J. van de Beek, M. Sandell, and P. Borjesson, "ML estimation of time and frequency offset in OFDM systems," *IEEE Trans. Signal Process.*, vol. 45, no. 7, pp. 1800–1805, 1997.

[91] T. Schenk, *RF Imperfections in High-rate Wireless Systems*. New York: Springer, 2008.

[92] X. Liu and F. Buchali, "Improved nonlinear tolerance of 112-Gb/s PDM-OFDM in dispersion-uncompensated transmission with efficient channel estimation," in *Proc. ECOC*, 2008, pp. 47–48.

[93] E. Mo and P. Kam, "Log-likelihood metrics based on two-symbol-interval observations for LDPC codes with BDPSK transmission," in *Proc. Of Vehicular Tech. Conf.*, 2008.

[94] H. Tatsunami, K. Ishibashi, and H. Ochiai, "On the performance of LDPC codes with differential detection over Rayleigh fading channels," in *Proc. Of Vehicular Tech. Conf.*, 2006.

[95] D. J. MacKay. Encyclopedia of Sparse Graph Codes. [Online]. Available: http://www.inference.phy.cam.ac.uk/mackay/codes/data.html

[96] E. Mo and P. Y. Kam, "Log-likelihood ratios for LDPC codes with pilot-symbol-assisted BPSK transmission over the noncoherent channel," in *Proc. WCNC*, 2009.

[97] W. Shieh and et al, "Optical performance monitoring in coherent optical OFDM systems," *Opt. Express*, vol. 15, no. 2, pp. 350–356, 2007.

[98] S. Cao, C. Yu, and P. Y. Kam, "Mitigation of nonlinearity based on optimized percentage of dispersion pre-compensation in coherent optical PDM-OFDM systems," in *Proc. Photonics Global Conference*, 20012.

[99] I. Djordjevic, M. Cvijetic, L. Xu, and T. Wang, "Using LDPC-coded modulation and coherent detection for ultra highspeed optical transmission," *J. Lightw. Technol.*, vol. 25, no. 11, pp. 3619–3625, 2007.

Publication List

Journal Papers

1. Shengjiao Cao, Changyuan Yu and Pooi-Yuen Kam, Time-domain blind ICI mitigation for non-constant modulus format in CO-OFDM, *IEEE Photon. Technol. Lett.*, vol. 24, no. 25, pp. 2490-2493, 2013.

2. Shengjiao Cao, Changyuan Yu and Pooi-Yuen Kam, A performance investigation of correlation-based and pilot-tone-assisted frequency offset compensation method for CO-OFDM, *Opt. Express*, vol. 21, no. 19, pp. 22847-22853, 2013.

3. Shengjiao Cao, Pooi-Yuen Kam and Changyuan Yu, Pilot-aided log-likelihood ratio for LDPC coded MPSK-OFDM transmissions, *IEEE Photon. Technol. Lett.*, vol. 25, no. 6, pp. 594-597, 2013.

4. Shengjiao Cao, Pooi-Yuen Kam and Changyuan Yu, Decision-aided, pilot-aided, decision-feedback phase estimation for coherent optical OFDM systems, *IEEE Photon. Technol. Lett.*, vol. 24, no. 22, pp. 2067-2069, 2012.

5. Shengjiao Cao, Changyuan Yu and Pooi-Yuen Kam Decision-aided joint compensation of transmitter IQ mismatch and phase noise for coherent op-

tical OFDM, *IEEE Photon. Technol. Lett.*, vol. 24, no. 12, pp. 1066-1068, 2012.

Conference Papers

1. Shengjiao Cao, Pooi-Yuen Kam and Changyuan Yu, Pilot-aided Log-likelihood Ratio for LDPC coded M-QAM CO-OFDM System, accepted by *Optical Fiber Communication conference (OFC)*, 2014.

2. Shengjiao Cao, Shaoliang Zhang, Changyuan Yu and Pooi-Yuen Kam, Full-range pilot-assisted frequency offset estimation for OFDM systems, in *Proc. Optical Fiber Communication conference (OFC)*, 2013.

3. Shengjiao Cao, Changyuan Yu and Pooi-Yuen Kam, Mitigation of nonlinearity based on optimized percentage of dispersion pre-compensation in coherent optical PDM-OFDM systems, in *Proc. Photonics Global Conference (PGC)*, 2012.

4. Shengjiao Cao, Chuangyuan Yu and Pooi-Yuen Kam, Log-likelihood metric for LDPC coded BDPSK-OFDM transmission, in *Proc. OECC*, 2012.

5. Shengjiao Cao, Pooi-Yuen Kam, and Changyuan Yu, Pre-distortion versus post-equalization for IQ mismatch compensation in CO-OFDM, in *Proc. OECC*, 2012.

6. Shengjiao Cao, Changyuan Yu and Pooi-Yuen Kam, Decision-Aided Joint Compensation of Channel Distortion and Transmitter IQ Imbalance for Coherent Optical OFDM, in *Proc. MWP*, 2011.

7. Shengjiao Cao, Changyuan Yu and Pooi-Yuen Kam, Decision-aided carrier phase estimation for coherent optical OFDM, in *Proc. OECC*, 2011.